Respiration and Heart Rate Monitoring of Neonates using Thermal Imaging

R.B.Addaguduri Aditya

4769457

MSc. Embedded Systems,

TU Delft, 2021

Respiration and Heart Rate Monitoring of Neonates using Thermal Imaging

by

R.B.Addaguduri Aditya

to obtain the degree of Master of Science

at the Delft University of Technology,

to be defended publicly on 31 May 2021 at 13:00

Student number:	4769457	
Project duration:	December 9th, 2019 – May 31st 2021	
Thesis Supervisors:	Prof. dr. P. J. French,	TU Delft
	ir. K. Rassels ,	TU Delft
Thesis Committee:	Prof. dr. P. J. French,	TU Delft, supervisor
	Prof. dr. K. G. Langendoen ,	TU Delft
	dr. ir. C. Strydis,	TU Delft,

This thesis is confidential

Abstract

Non-contact monitoring of vitals is a growing field with numerous applications in monitoring neonates and adults alike. Previous research have already tried to monitor the vitals of the subject ranging from heart rate, breath rate, blood pressure etc using both RGB and Thermal imaging. As neonates have sensitive skin, some of the bulky apparatus used for monitoring their vitals have a lot of wires and have to be attached to the neonates using adhesive electrodes that can cause harm and inconvenience them. This project aims to explore the possibility of monitoring the vitals of the neonate remotely and without placing any sensors or electrodes on the subjects body. Due to the COVID-19 pandemic, the research had to be tested on adults instead of neonates due to health concerns. For analyzing the breath rate remotely in thermal imaging, almost all research have looked at either monitoring the thermal activity of the nose or the movement of the chest during the breathing cycles. For heart rate monitoring, remote photoplethysmography (rPPG) is a commonly used method to monitor the subject's heart rate remotely; using both RGB and thermal imaging. In this research, thermal imaging will be used to further explore the possibilities of monitoring heart and breath rates of the subject by looking further into understanding the behaviours of different regions of interest(ROI) in the frequency domain. Exploring different spectral analysis methods that are used to monitor the signal's frequency components have also been explored. Part of the research involving temperature noise compensation and the ROI tracking algorithm were done in cooperation with Erik Wirianto of TU Delft with his project "Predicting Infections in Preterm Infants with Thermal Imaging Technology".

Acknowledgement

Acknowledgement...

I also want to give my thanks to Paddy French and Kianoush Rassels, as my supervisors and mentors, for giving me support, guidance, and advice that greatly help me finish this thesis.

I want to thank my parents and my brother who always supported me and believed in me no matter what. I cannot express my gratitude enough for them.

I express my thanks to Erik Wirianto and all members and staffs of the Bio-Electronics, the Remote Sensing group and EWI department of TU Delft, and anyone who contributed to this thesis work.

I hope this thesis could contribute to any future research in relating topic.

Delft, May 2021

Contents

1 Introduction

1.1. Research Goal

The goal of this project is to implement contactless monitoring of respiration and heart rate using thermal imaging. This project aims at removing many sensors placed on the patients/neonates which could make them uncomfortable and cause skin damage in some situations.

Implementation involves getting accurate readings from the Infrared(IR) camera; FLIR SC305 was used for this project.The acquired data is filtered and processing to get the respective vitals; heart rate and respiration rate. Other associated programs like noise compensation and object detection with motion tracking will also be implemented for this project.

The research questions for this project are;

- How to continuously monitor the heart rate and the respiration rate of a neonate inside an incubator using non-contact thermal imaging ?
- If it is possible to monitor vitals of the neonate inside the incubator irrespective of the position he/she is in or the ROI that is being monitored ?
- Is it possible to acquire both heart and respiration rate simultaneously using the same method or algorithm?

1.2. Preterm Neonatal Care

The gestational age; which is the duration of a pregnancy, lasts about 37 to 42 weeks before delivering the child. However not all cases of deliveries happen in that specified duration. Children born before 37 weeks are called **premature neonates**[1]. It's because the child did not have time to fully develop within the mothers womb and was delivered earlier because of certain complications. Because of these unfortunate circumstances, a premature neonate is generally much smaller and lighter than a full term neonate. Their body is around 25-40 cm in length and 500-3000 g in weight, unlike the full-term neonates who are 50 cm in length and 3000+ g in weigh. On top of that, premature infants are also at greater risk for developing cerebral palsy, hearing problems etc. The earlier a baby is born, the greater these risks will be. Fortunately, at least 75% of preterm infants would survive with appropriate treatment. This makes providing the best care to neonates a top priority as this could provide the child hope to leading a long and healthy life.

Unfortunately, the current monitoring methods for neonates are not entirely safe for its well being and comfort. The sticky electrodes, shown in Figure 1.1, are used to measure the vitals of the baby but they can also cause skin irritations and skin lesions when being pulled off. Even if the electrodes are minimally adhesive, the electrodes can fall off and/or raise many false alarms. On top of that, this will also make the child feel very uncomfortable, who without the ability to express its pain goes though the anguish silently.

Figure 1.1: Premature Baby in an Incubator with sticky electrodes [1]

There could be improvements made to the incubator to have non-contact monitoring of vitals to reduce the discomfort of having the stick-on sensors while still effectively getting the readings for vitals. One method would be to use **Thermal Imaging** using Infra-Red(IR) cameras to monitor the Heart and Breathing of the child. This project focuses on researching and implementing the non-contact way to implementing the Respiration and Pulse Monitoring system using IR cameras.

1.2.1. Respiration and Pulse Monitoring

There are several techniques to monitor the vitals but the most common method and the gold standard for monitoring respiration is Transthoracic Impedance Plethysmography (TTI)[1]. An alternating current is passed between two electrodes that are placed on the chest. The changes in the chest volume and its composition caused by respiration changes the pattern of the current, from which respiration rate can be derived. The common method to get the pulse rate is Electrocardiography which also involves placing electrodes on the chest. As mentioned earlier, it is not convenient for the baby to put electrodes on it, because of the sensitive skin and not enough chest area for strong readings.

From [1], the average respiration frequency for a neonate baby is estimated at 40-60 times a minute. The neonatal heart rate is approximately 120-180 beats per minute. Occasionally, monitoring the respiration rate in neonates is challenging because of their irregular nature. It is because of their irregular nature. Apart from irregular breathing, neonates sometimes experience breathing pauses. When these pauses last longer than 10-15s, they are called apnea periods and require intervention.

Heart rate is also the most important indicator to evaluate the clinical status of a newborn[10]. Newborns may also require resuscitation at birth. Inaccurate pulse rate during resuscitation may lead to early neonatal mortality and also cause moderate to severe brain injury in those who survive it. Therefore, it is imperative to perform fast and accurate heart rate measurement for neonatal resuscitation.

As the long-term health and development of the premature baby depends on the care provided in the incubator, it is imperative to provide it with the necessary support. For that, a viable and non-contact monitoring system would be a good start to realizing that.

2

Technical Background and Research

2.1. Thermal Imaging

Thermal imaging is an imaging technique detecting infrared radiation, usually in the long-infrared range (9-14 μm), and producing image of the radiation. Human body emits significant radiations of wavelength in range 4 to 30 μm, with peak at 9 μm [22], which is suitable for the thermal imaging. Thermal imaging has been used in the medical scene more than 50 years, first used to find breast cancer in women. Compared to X-ray, computed tomography (CT), and mammography, thermal imaging is not harmful as it does not emit any radiation. It is a real time non-contact measurement method, like a normal camera. From the image of the radiation, we can see the difference of temperature between one object and the other, and also determine the temperature of the object, even though the accuracy of the measurement depends on a lot of variable. In case of thermal imaging on preterm infants, incubator environment is also affecting the measurement [14]. The hood of the incubator is generally made out of polymethyl methacrylate (PMMA) (also known as acrylic or plexiglass) or polycarbonate. Unfortunately, these materials are very poor for infrared wave transmission, so thermal imaging cannot look through these materials [23].

2.1.1. Thermal Radiation

Infra-red cameras usually detect these radiations in the long-infrared range of the EM spectrum, which is roughly 9–14 μm. The images produced by reading these IR radiations are called thermograms; which show how the heat from a body is being emitted. With increase in temperature, the amount of thermal energy emitted also increases; making it easier to detect temperature variations.The total thermal energy emitted by a surface of a black body for a given area is given as[2]:

$$P = \sigma A T^4 \tag{2.1}$$

where $\sigma = 5.670373x10^{-8}[Wm^{-2}K^{-4}]$ also called Stefan-Boltzmann constant, **A** is area of the radiating surface and **T** is the temperature of the object in Kelvin(^0K)[2]. However, each non-black body has a factor known as Emissivity(ϵ) which denote the spectral absorption component of a body. Emissivity is the ratio of the thermal radiation from a surface to the radiation from an ideal black surface at the same temperature as given by the equation 2.1. This shows the effectiveness of a body to emit as thermal radiation. For an ideal black body, $\epsilon = 1$ but for the rest of the objects, it falls in the range $0 < \epsilon < 1$. This transform equation 2.1 to :

$$P = \sigma \epsilon A T^4 \tag{2.2}$$

As mentioned in [4], the emissivity of human skin is around $0.97 < \epsilon < 0.98$ for range of 2-14 μm , there will be a very small amount of thermal reflection from the surrounding. This understanding will provide us a more accurate way of measuring the baby's temperature using IR cameras. Apart from emissivity, there are many other factors that effect the accuracy of the temperature reading from IR camera.

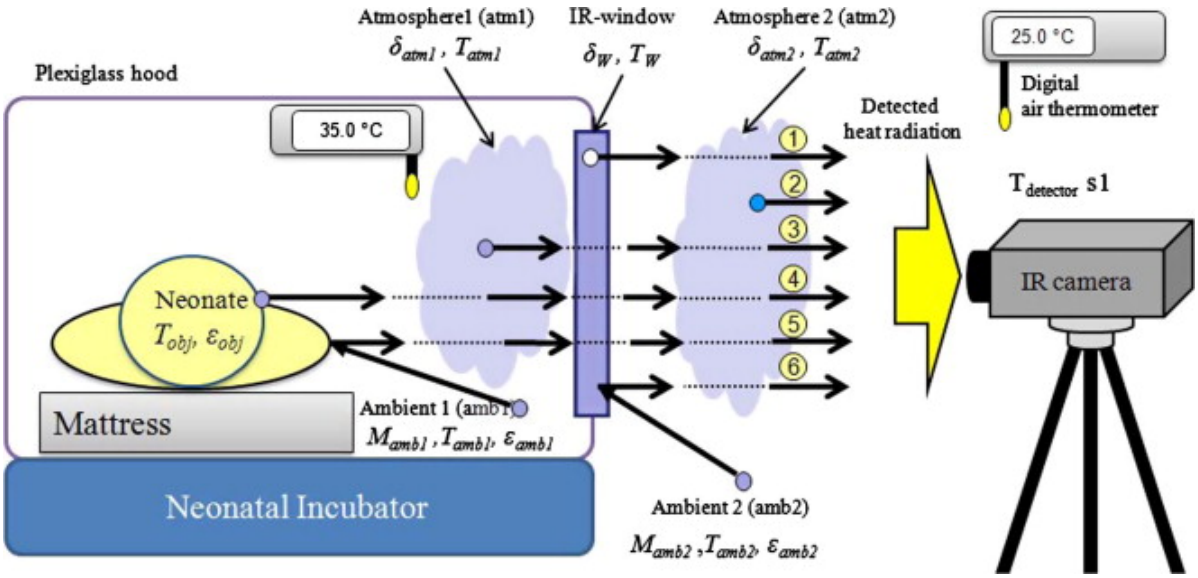

Figure 2.1: Thermal measurement of neonate inside incubator with infrared camera. Adapted from 'Neonatal infrared thermography imaging: Analysis of heat flux during different clinical scenarios,' by Abbas, A. K. et al, 2012, Infrared Physics & Technology, 55(6), 538–548.

2.1.2. Thermal Measurement Model

A generalized model of thermal measurement of neonate inside an incubator is shown in the figure 2.1. There are 6 sources of radiation detected by the camera, (1) infrared window, (2) atmosphere outside the incubator, (3) atmosphere inside the incubator, (4) the actual neonate that is being measured, (5) reflection of ambient object inside incubator, and (6) reflection of ambient object outside incubator. The infrared window can be an infrared transparent foil. If the measurement setup does not use window (open hole), sources number 1 and 6 can be disregarded.

An equation can be derived from the model as:

$$T_{detector} = \frac{T_{obj}}{\epsilon_{obj}\cdot\delta_{atm1}\cdot\delta_w\cdot\delta_{atm2}} + \frac{(1-\epsilon_{obj})\cdot T_{amb1}}{\epsilon_{obj}} + \frac{(1-\delta_{atm1})\cdot T_{atm1}}{\epsilon_{obj}\cdot\delta_{atm1}} + \frac{\epsilon_w\cdot T_w}{\epsilon_{obj}\cdot\delta_{atm1}\cdot\delta_w} + \frac{R_W\cdot T_{amb2}}{\epsilon_{obj}\cdot\delta_{atm2}\cdot\delta_w} + \frac{(1-\delta_{atm1})\cdot T_{atm2}}{\epsilon_{obj}\cdot\delta_{atm1}\cdot\delta_w\cdot\delta_{atm2}} \tag{2.3}$$

where variable T, ϵ, δ, and R are temperature, emissivity, transmittance, and reflectance respectively, with description $detector$ means the infrared camera, obj means object measured, $amb1$ and $amb2$ mean ambient object inside and outside the incubator, $atm1$ and $atm2$ mean atmosphere inside and outside incubator, and w means infrared window.

If there is no infrared window, we can segment the total radiation received by the camera as radiation from actual object measured, reflective radiation from other objects around the object measured, and radiation of the atmosphere between object and infrared camera. The equation then, can be modified to:

$$T_{detector} = \frac{T_{obj}}{\epsilon_{obj}\cdot\delta_{atm1}\cdot\delta_w\cdot\delta_{atm2}} + \frac{(1-\epsilon_{obj})\cdot T_{amb1}}{\epsilon_{obj}} + \frac{(1-\delta_{atm1})\cdot T_{atm1}}{\epsilon_{obj}\cdot\delta_{atm1}} + \frac{(1-\delta_{atm1})\cdot T_{atm2}}{\epsilon_{obj}\cdot\delta_{atm1}\cdot\delta_{atm2}} \tag{2.4}$$

Object Measured Radiation

The radiation coming from the object measured is the specific radiation we want to measure to determine the temperature of the object, in this case the neonate. However, the radiation will go through the atmosphere and infrared window (if there is any), which will attenuate the radiation. if not compensated, the infrared camera will underestimate the temperature of the object. The compensation is shown in the formula as

dividing the object temperature with transmittance of atmosphere and infrared window. Lower transmittance can be caused by the window or particles in the atmosphere.

Reflective Radiation

In the infrared wavelength, neonate is not a black body, which means the neonate is reflecting some radiation from objects around it. This reflectivity depends on the emissivity of the object, in this case emissivity of neonate is 0.97-0.98 [25, 26]. High emissivity means that almost all radiation is coming from the actual object, hence more accurate approximation of the temperature. Even so, 2-3% of the radiation is still coming from the temperature of objects around the neonate. This yields small measurement error and needs to be compensated. The compensation in the formula is in the T_{amb1} part of the equation.

Atmospheric Radiation

Particles in the atmosphere can attenuate infrared radiation as we know in air transmittance, however, these particles also radiate heat because of their temperature, causing additional incoming radiation to the camera. Hence, in the equation, we see the atmospheric temperature contribution to the total radiation.

2.1.3. Total Measurement Error

Temperature measurement of infrared camera would have error measurement which can be caused by error of method, calibration error, and electronic path error. In real condition, error of method is coming from incorrect evaluation of object emissivity, ambient temperature, atmospheric temperature, relative atmospheric humidity, distance from camera to object, and atmospheric transmission and radiance [29]. There is also contribution of detector noise in the camera.

Based on the general model from figure 2.1, error simulation from *Infrared Thermography : Errors and Uncertainties* (Minkina & Dudzik, 2009), and experiment, the total measurement error budget for a thermal imaging measurement on neonate inside an incubator can be summarized in equation:

$$\begin{aligned} T_{error} = & \frac{\Delta\epsilon}{0.245} \times 0.01 T_{obj} + \frac{\Delta T_{ambient}}{8.8K} \times 2.2 \times 10^{-3} T_{obj} + \frac{\Delta T_{atmosphere}}{8.8K} \times 5 \times 10^{-4} T_{obj} + \\ & \frac{\Delta d}{30m} \times 3 \times 10^{-4} T_{obj} + \frac{\Delta\omega}{15\%} \times 3 \times 10^{-4} T_{obj} + \text{camera thermal noise} + \\ & \text{thermal lens error} + \text{calibration and electronic path error} \end{aligned} \tag{2.5}$$

where T_{error} is the total temperature error of the measurement, T_{obj} is the actual temperature of the object, ϵ is emissivity of the object, $T_{ambient}$ is the temperature of objects around the measured object, $T_{atmosphere}$ is the atmospheric temperature, d is distance of object from camera, and ω is relative humidity of the environment.

2.2. Optical Flow

Optical flow is the method of movement estimation of objects or other feature points like edges,surfaces etc in a video source caused by relative motion between the observer and the observed region[41, 42]. This means that optical flow is the apparent motion of individual pixels on the image frame. Methods that compute optical flow assume that the color intensity of a pixel is invariant under the displacement from one video frame to the next[41, 42]. This means that optical flow can be expressed as[41, 42] 2.6

$$I(x,\ y,\ t) = I(x+dx,\ y+dy,\ t+dt) \tag{2.6}$$

where *I(x,y,t)* is the pixel intensity of a point(x,y) on a frame at a given time(t). Assuming that the movement of the pixels is small between frames, equation 2.6 can be approximated using Taylor series as

$$I(x+dx, y+dy, t+dt) = I(x,y,t) + \frac{\partial I}{\partial x}\partial x + \frac{\partial I}{\partial y}\partial y + \frac{\partial I}{\partial t}\partial t + ... \tag{2.7}$$

$$=> \frac{\partial I}{\partial x}\partial x + \frac{\partial I}{\partial y}\partial y + \frac{\partial I}{\partial t}\partial t = 0 \tag{2.8}$$

Dividing equation 2.8 w.r.t. ∂t can be approximated to

$$=> \frac{\partial I}{\partial x}u + \frac{\partial I}{\partial y}v + \frac{\partial I}{\partial t} = 0 \tag{2.9}$$

where $u = \frac{\partial x}{\partial t}$ and $v = \frac{\partial y}{\partial t}$, giving us the relative speed of the pixel intensity along each axis. $\frac{\partial I}{\partial x}$, $\frac{\partial I}{\partial y}$ and $\frac{\partial I}{\partial t}$ are the frame's gradients along their respective axes. This gives a good approximation of movement and/or direction of an object from an observer's point of view without using object detection. However, u and v are unknown variables and as they are part of only one equation, they cannot be solved. This is called as *aperture problem*[41, 42] for optical flow algorithms and there are motion estimation or flow approximation algorithms used along with optical flow to solve this problem.
There are two different types of optical flow algorithms; *sparse* and *dense* optical flow. Sparse optical flow calculates the flow vectors of special features like edges or user selected feature points on a frame. It will be tracking the pixel intensity of the selected points on the frame. It is not always accurate but fast and easy to compute. For e.g. Lucas–Kanade method, the Horn–Schunck method, the Buxton–Buxton method etc. Dense optical flow gives the flow vectors of the entire frame i.e. all pixels are given a flow vector. Despite of having higher accuracy, it is slow and computationally expensive. One example of dense optical flow is the Gunnar Farneback algorithm.

2.2.1. Gunnar Farneback Optical Flow Algorithm

Gunnar Farneback Algorithm[40] is a dense optical flow algorithm that uses polynomial expansion to approximate the neighborhood of each pixel. It estimates the motion, or displacement, field from only two frames and tries to compensate for the background motion. A local signal model can be expressed in a local coordinate system as[40],

$$f_1(x) = x^T A_1 x + b_1^T x + c_1 \tag{2.10}$$

where A_1 is a symmetric matrix, b_1 a vector and c_1 a scalar.They are the global approximation coefficients of an image. Lets construct a new signal f_2 by a global displacement by d

$$f_2(x) = f_1(x \quad d) = (x \quad d)^T A_1 (x \quad d) + b_1^T (x \quad d) + c_1 \tag{2.11}$$

$$= x^T A_1 x + (b_1 \quad 2A_1 d)^T x + (d^T A_1 d \quad b_1^T d) + c_1 \tag{2.12}$$

$$= x^T A_2 x + b_2^T x + c_2 \tag{2.13}$$

$$=> A_2 = A_1 \qquad b_2 = (b_1 \quad 2A_1 d) \qquad c_2 = (d^T A_1 d \quad b_1^T d) + c_1) \tag{2.14}$$

Looking at equation 2.14, it is possible to solve for d; given A_1 is non-singular

$$2A_1 d = (b_2 \quad b_1) \qquad => \qquad d = \frac{1}{2} A_1^{-1} (b_2 \quad b_1) \tag{2.15}$$

Ideally from equation 2.14 $A_1 = A_2$ but in real applications, the average of the two is used for a good approximation. Instead of taking the global coefficients, $A_1(x)$, $b_1(x)$ & $c_1(x)$ would be the local approximation coefficients. This gives the following equations,

$$A(x) = \frac{A_1(x) + A_2(x)}{2} \tag{2.16}$$

$$\Delta b(x) = (b_2(x) \quad b_1(x)) \tag{2.17}$$

This can be expressed as,

$$A(x)d(x) = \Delta b(x) \tag{2.18}$$

where d(x) indicates the local displacement field of each coordinate, giving a spatially varying displacement field. This is done assuming that the local polynomials at the same coordinates in the two frames are identical except for a certain displacement. Since the local models of these polynomial expansions will vary spatially, it introduces errors in the constraints in equation [40]2.18. However, for small displacements this is not too serious, but with larger displacements the problem increases. This can be solved if we have a priori knowledge about the displacement field i.e. we can compare the polynomial at x in the first signal to the polynomial at $x+\widehat{d}(x)$in the second signal, where $\widehat{d}(x)$ is the a priori displacement field rounded to integer values. Then the relative displacement can be estimated between the real value and the rounded a priori estimate, giving the following equations,

$$\widehat{x} = x + \widehat{d}(x) \tag{2.19}$$

$$A(x) = \frac{A_1(x) + A_2(\widehat{x})}{2} \tag{2.20}$$

$$\Delta b(x) = (b_2(\widehat{x}) \quad b_1(x)) + A(x)\widehat{d}(x) \tag{2.21}$$

2.2.2. Image Pyramid

In order to filter out the small amplitude noise, optical flow also performs scaling down the image or frame in lower resolutions to only respond to the major changes, as shown in fig.2.2. The process of scaling an image to lower resolutions while parallelly considering the original resolution is called pyramid scaling. A scaling factor(<=1) decides the fraction by which the image resolution is reduced i.e. for 0.5 scaling factor, resolution of the image halves at every level or layer. The number of layers decide on the level to which the scaling will be performed.

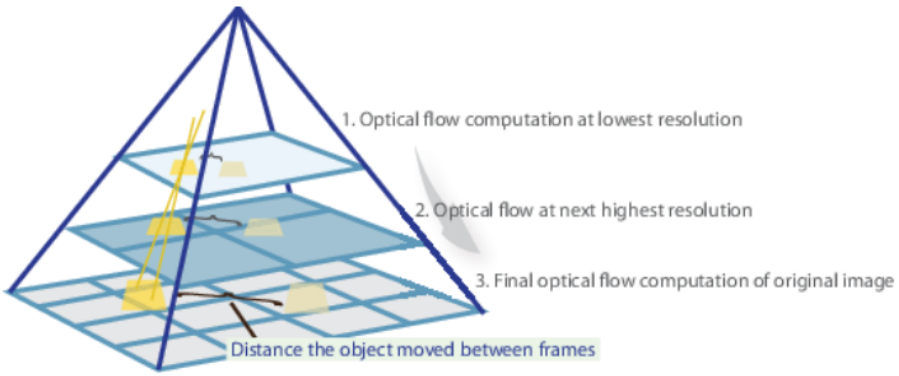

Figure 2.2: Pyramid Scaling for Optical Flow

2.3. Feature Point Detection and Matching

2.3.1. Image Feature Detectors and Descriptors

In order to compare similarities or correspondences between multiple images, it is required to isolate a set of distinct features between these images in order to be able to classify and compare them. Feature point detection is a low-level image processing operation which means that it is usually the first operation on an image that examines every pixel to see if there is a features present; like edges and corners or smooth regions with similar features called blobs and ridges.There are two types of image features can be extracted form an image, as mentioned in [35];

- **Global Features:** These try to describe an image as a whole and can classify the property of all the pixels in the image; like colour histogram, texture etc into one multi-dimensional feature vector. This can be used to find images of similar nature. However, these cannot distinguish between background and foreground.
- **Local Features :** The image is represented based on its local structures or interest regions and some of its salient features. This includes a set of local feature descriptors/vectors that are affine and scale invariant. They are better suited for finding other occurrences of the similar objects or region of pixels in the images.

These relevant features points or keypoints are then converted into an affine, orientation and scale invariant feature vector representation for the image data around the detected features; providing **feature descriptors**. These descriptors are later used to match the similarities between different images. The purpose of local invariant features is to provide a representation that can efficiently match then with another image despite there being shifting, scale or orientation changes. In order to detect feature points invariant of scale, affine or orientation changes for the interest regions between images, there are methods that use a continuous filter kernel to check for distribution or gradient or looking for a maximally stable region around the detected feature points; as mentioned in [36]. Area around each keypoint that is considered for the descriptor is usually taken in a circular or elliptical pattern.

In order to make sure that the feature point detectors and descriptors work efficiently, the following properties, mentioned in [35] need to be satisfied;

- **Robustness:** to be able to detect the same feature points irrespective of shifting, rotation or noises.
- **Repeatability:** to be able to detect the same features of the same interest region repeatedly under different viewing conditions.
- **Accuracy:** to accurately localize the same image features in different images; especially for image matching tasks.
- **Generality:** to be able to detect features that can be used in different applications.
- **Efficiency:** to be able to detect features in images fast enough to support real-time applications.
- **Quantity:** to be able to detect all or most of the features in the image.

Some of the examples of commonly used image feature descriptor algorithms are;

1. *Scale Invariant Feature Transform (SIFT):* This algorithm consists of four steps, as mentioned in [37];
   (a) Estimate a scale space extrema using the Difference of Gaussian (DoG).
   (b) Keypoints are localized and refined by removing the low contrast points.
   (c) Orientation is estimated based on local image gradient.
   (d) Generate descriptors for each feature point of image based on image gradient and the estimated orientation.

   It is useful for cases like image rotation, affine transformations, intensity or perspective change.
2. *Gradient Location-Orientation Histogram (GLOH):* It is very similar to the SIFT descriptor, but uses log-polar coordinates for keypoints instead and then tries to reduce the size of the descriptor;as mentioned in [36].
3. *Speeded-Up Robust Features Descriptor (SURF):* According to [37], it is as an alternative to SIFT; but much faster and more robust. The steps for this algorithm are;
   (a) Instead of DOG averaging, squares are used for localizing keypoints since it is less complex and much faster.
   (b) Uses a scale invariant blob detector around the detect a stable neighbourhood of pixels around the keypoints.

(c) Wavelet response for each of the keypoints' regions is taken in both horizontal and vertical directions and their responses are used for the feature point descriptors.

This also allows the detector to be parallelly run on different image scales, making it capable of much faster performance.

4. *Binary Robust Independent Elementary Features (BRIEF):* This algorithm performs simple binary comparison test and uses hamming distance for comparison tests; as mentioned in [35]. This means that the algorithm compares the pixel intensity around the detected feature points which gives sufficient information and provides with binary feature descriptors, which is faster and more efficient. The descriptors are then matched based on the hamming distance between them. This algorithm relies on a relatively small number of tests to represent an interest region as a binary string and also tends to yield higher recognition rates, provided there are no large in-plane rotations.

5. *Features from Accelerated Segment Test (FAST):* It uses corner detection method to extract the feature points and is very suitable for real-time applications because of its higher speed; as mentioned in [35]. The steps for this algorithm are;

   (a) Select interest points across the image and take 16 pixels surrounding each of these points under consideration; pixels that would lie on the path of a circle with radius of 3 pixels drawn from each feature point.

   (b) In the 16-point set for each interest point, check if there are a set of continuous pixels that are either brighter or darker that the pixel intensity of the feature points by a set threshold value.

   (c) Only if the condition is satisfied, the interest point is taken as a corner. This process is iterated over all interest points or for all pixels in the image.

   (d) The performance of this algorithm depends on the threshold value and the limit for minimum number of continuous pixels that need to be considered for the corner test; usually around 12.

   This process however has some disadvantages;

   - The algorithm does not work if the limit for minimum continuous pixels is less than 12.
   - The order of testing the 16 neighbouring pixels also determines the speed of the algorithm.
   - It does not have any orientation component or detects scaling.

6. *Oriented FAST and Rotated BRIEF (ORB):* It is a fusion of the FAST key point detector and BRIEF descriptor; both these algorithms contribute to ORB's computational speed and efficiency; as mentioned in [34]. The steps for this algorithm are;

   (a) Initially to determine the key points, it uses the FAST algorithm. Since FAST does not have any orientation or scaling features, ORB creates a scaled image pyramid; similar to the one in fig.2.2, where it contains the down sampled versions of the same image and the FAST algorithm is run on every level. This makes the detected key points scale invariant.

   (b) Orientation is assigned based on the levels of pixel intensity change around the key points.In ORB it is done by using intensity centroid where it is assumed that a corner's intensity is offset from its center, and the vector between the two points may be used to impute an orientation. For this, the moments of a patch is calculated; which is defined as,

$$m_{pq} = \sum_{x,y} x^p y^q I(x,y) \tag{2.22}$$

   where (p+q) is the order of the moment of the patch or a defined neighbourhood of pixels around the key point; pixel coordinates (x,y) and I(x,y) being the respective pixel intensity. With these moments, we can find the intensity centroid is calculated as;

$$C = (\frac{m_{10}}{m_{00}}, \frac{m_{01}}{m_{00}}) \tag{2.23}$$

This can be used to construct the vector from the centre of the keypoint to the intensity centroid; giving the orientation of the patch as,

$$\theta = atan2(m_{01}, m_{10}) \tag{2.24}$$

This can be used to rotate the patch and compute the descriptor with rotation invariance.

(c) BRIEF takes all keypoints found in the previous step and converts it into a binary feature vector of around 128–512 bits string so that together they can represent an object. Then, the image is smoothed by using a Gaussian filter to remove any high frequency noises. After the image is smoothed, a patch **p** is taken and a binary test τ is performed; which is defined as,

$$\tau(p; x, y) = \begin{cases} 1 & : p(x) < p(y) \\ 0 & : p(x) \geq p(y) \end{cases} \tag{2.25}$$

where p(x) is the intensity of **point x** in the patch **p**; both x and y are points inside the same patch. The feature point is defined as a vector of **n** binary tests:

$$f_n(p) = \sum_{1 \leq i \leq n} 2^{(i-1)} \tau(p; x, y) \tag{2.26}$$

As the performance of BRIEF falls off sharply for in-plane rotation of more than a few degrees, ORB uses another method to steer BRIEF according to the orientation of the keypoints. For a feature point with **n** tests and key point coordinate (x_i, y_i), a *2 x n* matrix is defined as;

$$S = \left\{ x_1, x_2, ...x_n y_1, y_2, ...y_n \right. \tag{2.27}$$

With the patch orientation θ and its corresponding rotation matrix R_θ, the steered version of the **S** matrix; namely S_θ is defined as;

$$S_\theta = R_\theta S \tag{2.28}$$

Now the steered BRIEF operator can be written as;

$$g_n(p, \theta) = f_n(p) \,|\, (x_i, y_i) \in S_\theta \tag{2.29}$$

Using equation 2.29, a lookup table of pre-computed BRIEF patterns is generated with an angle increment of $2\pi/30(12°)$. As long as the keypoint orientation angle θ is consistent, the respective $S\theta$ can be used to compute its descriptor.
ORB algorithm specifies the rotated BRIEF algorithm with the following steps:

i. Run the test equation2.26 against all available patches.

ii. Order the results of the tests by their hamming distance from a mean value of 0.5,resulting in the vector T.

iii. A greedy search is performed on all the values in vector T:

   A. Remove the first test from T into the result vector R.

   B. Remove the next test from T and compare it against all tests in R. The test is discarded if its absolute correlation is greater than a previously set threshold value. If not, then the test add to R.

   C. Repeat the process until there are 256 tests in R. If there are no more tests in T and there are fewer than 256 tests in R, raise the threshold value and repeat the process.

2.3.2. Feature Matching

Once the features and their descriptors have been created from multiple images, they need to be matched in order to look for similarities between the images. In order to achieve that, a **matcher** is used in combination with the feature point detector to use the information provided by the descriptors and match the interest regions from the query image to the others.

The feature matchers commonly used along with the feature descriptors are;

1. **Brute-Force (BF):** This algorithm compares each feature point from the first image to every other feature point on the other image by calculating distance between the feature points; as mentioned in [35]. As the feature points are multi-dimensional vectors describing the aspects of their respective images, the Euclidean distance calculated between them is calculated. However if the descriptors are binary in nature like BRIEF, then the Hamming between them is calculated. After that, the points are sorted in ascending order based on distance. A match between two feature points is viable only when both points are the best matches for each other. This means that for any feature point p in the first image and feature point q in the second, p and q are a valid match with each other when q has the shortest distance with p of all points in the first image and p has the shortest distance with q of all points in the second image.
2. **Fast Library for Approximate Nearest Neighbors (FLANN):** This algorithm is optimized to be much faster that Brute-Force matcher; as mentioned in [38]. Instead of looking for the best match like the BF matcher, FLANN only finds a nearest neighbor. It builds a **k-d tree** of the feature points that will be used to search for an approximate neighbour. A **k-d tree** is a binary search tree, where each node of the tree is a k_{th} dimensional vector. This means that the matches provided by FLANN are fast but less accurate as compared to BF matcher.

BF matcher will provide accurate results but it will perform an exhaustive search comparing every feature point between the images, making is slow for large number of feature points. FLANN is much faster than BF but with a trade-off in accuracy. For data sets much larger than 1000 feature points, it would be more efficient to use FLANN as a matcher. Otherwise. BF matcher is a better approach.

2.4. TCP/IP Communication

Transmission Control Protocol/Internet Protocol(TCP/IP) is a reliable, heavy-weight and ordered communication protocol used to connect devices over an IP network, as mentioned in [39]; it consists of a large overhead/header of around 20-80 bytes; but most implementations have 40 bytes header. It is a connection-oriented protocol, which means that a connection needs to be established between the communicating devices i.e. the client and the server before transmitting data and should close after transmitting. In order to establish a connection, TCP/IP performs a three-way handshake[39]. The server is passive open; looking for connection requests from clients if not already established. When a connection is formed between a client to a server;

1. The client first sends a synchronize (SYN) bit set to the server requesting to start communication and what sequence number the client will use for its segments.
2. The server then responds to the client's request with SYN and the acknowledge (ACK) signal set, acknowledging the message from the client and informing it's own sequence number it will be using to the client.
3. The client finally sends another ACK bit set to acknowledge the server's segment and then the data transfer process begins.

The TCP/IP model consists of four layers[39];

- **Application Layer :** It's responsible for implementing the communication part of the program. It includes node-to-node communication, synchronizing, user-interface specifications etc. Some of the protocols present in this layer are: Hypertext Transfer Protocol(HTTP), File Transfer Protocol(FTP), Secure Shell(SSH) etc.
- **Transport Layer :** It is responsible for the reliability of the link over the network and maintaining it through methods like flow control,correction of data, multiplexing etc.
- **Internet Layer :** It is responsible for dealing with the packets and providing a functional method for transferring packets by connecting to independent networks for data transfer.
- **Network Access Layer :** It is responsible for determining how the data should be sent physically between devices over the same network. It is the lowest layer in the model.

The structure in fig.2.3 shows the format used for a TCP/IP message segment. It consists of around five or

six *32 bits / 4 bytes* long words of header, but the *Options and Padding* in the header can go upto 40 bytes depending on the connection parameters. As mentioned earlier, the commonly used size of the header is around 40 bytes; with *Options and Padding* around 20 bytes. The checksum in each header segment is used by the server to verify that the data is undamaged. If the data received is undamaged, the server sends a positive acknowledgment back to the client confirming a successful transfer. If the data is damaged, the server discards it and after a timeout period, the client will transmits the same data again until it receives the positive acknowledgment.

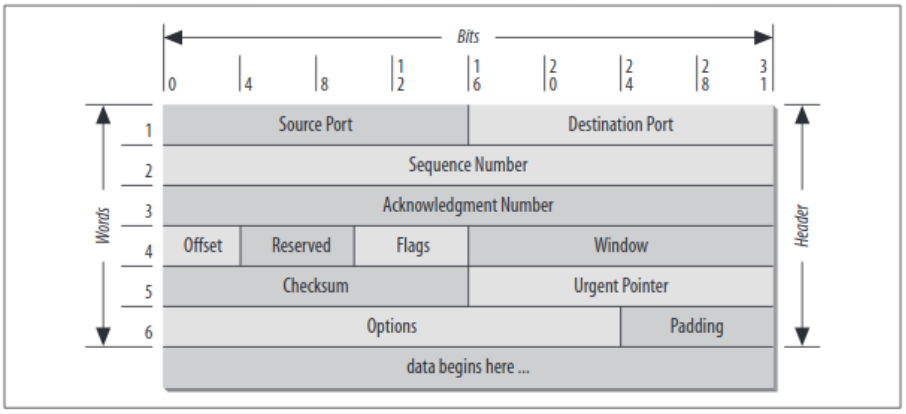

Figure 2.3: TCP/IP Segment Format[39]

With 40 bytes header, it is important to reduce *overhead*; it is the ratio between the header size to the message size. The maximum segment size (MSS) for a TCP/IP is the largest amount of data that the protocol can transport over the network; it is usually around 1460 bytes. Payload size larger than that is either discarded or segmented into multiple TCP segments. If the data payload is fragmented into multiple segments, then each segment gets its own header which adds extra 40 bytes for each segment.

$$Overhead(\%) = 100 * INT[(Payload\,Size\,/\,MSS) + 1] * (Header\,Size)\,/\,Payload\,Size \tag{2.30}$$

The overhead that constitutes the message packets after segmentation is mentioned in equation 2.30; which is only valid if the payload is not an integral multiple of the MSS. If the payload size is an integral multiple of the MSS, then it achieves the lowest possible overhead depending on the header size and the MSS.

$$Lowest\,Overhead\,Possible(\%) = 100 * Header\,Size\,/\,MSS \tag{2.31}$$

For a header size of 40 bytes and MSS of 1460 bytes, the lowest overhead that can be achieved is **2.7397%**. As seen in fig.2.4; for the formerly mentioned parameters, the overhead forms a saw-tooth shaped function where it dips to **2.7397%** when the package size is an integral multiple of MSS(1460 bytes). This is why it is preferable to have a payload size

2.5. Monitoring Breathing Activity

There have been many methods of monitoring respiration rate in both humans and animals. However, there are many contact-based respiration monitoring methods; classified based on the input they depend on are[50],

- **Respiratory Airflow :** Sensors are used for measuring the volume and/or the velocity of the inhaled and exhaled air during breathing. They are generally placed near the nostrils[50]. The sensors used are;
  1. *Differential Flowmeters*
  2. *Turbine Flowmeters*
  3. *Hot Wire Anemometers*

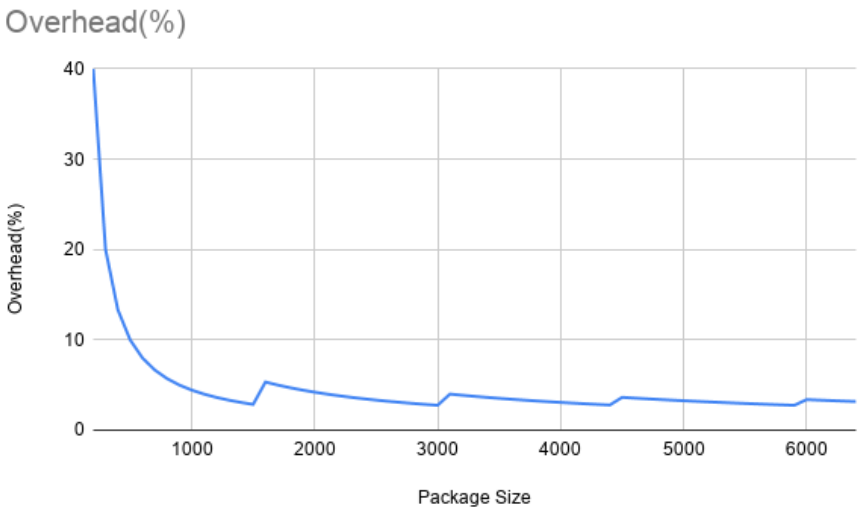

Figure 2.4: Overhead(%) for different message size

4. *Fiber-Optic Based Flowmeters*

- **Respiratory Sounds :** During breathing, sound is generated by the air flowing through the patient's throat and airways. It is collected to investigate the inspiration and expiration phases of breathing. So, a microphone is placed near the throat region or the nostrils to record sound changes during respiration[50].
- **Air Temperature :** During breathing, the exhaled air is warmer than the inhaled air with difference between them reaching approximately $15°C$. Therefore, different temperature sensors allow estimating respiration rate, depending on the temperature difference between exhaled and inhaled air. They are also placed near the nostrils[50].
    1. *Thermistors*: The resistive thermometer or thermistor is a type of resistor whose resistance is dependent on temperature.
    2. *Thermocouples*: The sensor exploits the Seeback effect to measures the heat difference due to exhalation around the nostrils.
    3. *Pyroelectric Sensors*:This sensor generates a current which is proportional to the rate of temperature change.
    4. *Fiber-Optic Sensors*: The sensor measures wavelength shift that has a linear response with temperature changes.
- **Air Humidity :** The inhaled and exhaled air have different water vapor content. Therefore, these sensors are placed near the nostrils to estimate the respiratory signal from the difference of water vapor contents between inhaled and exhaled air[50].
    1. *Capacitive Sensors*: These sensors depend on the change in capacitance between the electrodes which happens because of the change in the dielectric medium between them.
    2. *Resistive Sensors*: These sensors provide RH estimation based on the electrical impedance change with humidity.
    3. *Nanocrystals and Nanoparticles Sensors*: Humidity monitoring with fabricated nanocrystals, nanoparticles and graphene-based nanocomposites is efficient because of the high ratio between exchange surface and volume.
    4. *Fiber-Optic Sensors*: The coatings of the optic sensors are made of hygroscopic materials that absorb or exude environmental water vapor depending on humdity changes.

- **Air Components:** During breathing, the oxygen and carbon dioxide levels differs between the inhaled and exhaled air with a difference of around 6% increase in CO_2 during exhalation. Sensors near the nose region measure this increase in CO_2 to monitor the breathing cycles. These kind of sensors use masks or ventilators to direct the exhaled gas to the sensor implanted on the mask[50].

  1. *Infrared Sensors*
  2. *Fiber-Optic Sensors*

- **Chest Wall Movement Analysis:** Breathing is made possible by the work of the respiratory muscles, with the diaphragm playing a major role during inspiration. The diaphragm's expansion and contraction produces pressure difference causing air to enter and leave the lungs. This causes movement in the chest because of the expansion and contraction of the chest cavity during respiration. Therefore, sensors are used to either measure the change in strain around the chest or the movement of the chest during respiration[50].

  Strain Sensors: These sensors use the deformations of the chest wall for an indirect measurement of respiratory activity. Sensors are placed around the chest to measure the chest movement[50].

  1. *Resistive Sensors*: The sensors change their shape in strain which in turn causes them to change their resistance.
  2. *Capacitive Sensors*: The change in capacitance between electrodes placed in the front and back of the chest is monitored to observe the respiration cycles.
  3. *Inductive Sensors*: Breathing in/out produces variations in the self-inductance of the coil around the chest, causing a change in the oscillator's frequency.
  4. *Fiber-Optic Sensors*: The change in chest cavity during respiration will cause strain, leading to change in wavelength it will reflect, providing details of the chest position during respiration.

  Transthoracic Impedance Sensors: The relationship between the change in the impedance of the chest during respiration and the respiratory volume is approximately linear. There is an increment of the electrical impedance during inspiration because of the increase in chest size and decrease in conductivity because of the air in the chest. This allows the monitoring of the respiratory activities, including the volume of inhaled and exhaled air. This method also happens to be the gold standard for measuring respiratory rate[50]. **Movement Sensors**: Movement sensors are placed on the chest wall of the subject so that they can follow the chest movement during respiration. This includes placing accelerometers, gyroscopes and magnetometers around the chest region[50].

  1. *Accelerations Sensors (Accelerometers)*: An accelerometer converts mechanical motion into an electrical signal.
  2. *Angular Velocities Sensors (Gyroscopes)*: A gyroscope provides the angular velocity of the frame it's placed on.
  3. *Magnetic Field Sensors (Magnetometers)*: The magnetic vector of the sensor rotates due to the chest movement during the breathing activity changing magnetic vector components.

- **Modulation of Cardiac Activity:** Respiration has a low frequency effect on cardiac activity. With appropriate filters, it is possible to filter out respiratory rate from the same signal used to monitor the heart. It means that respiratory activity can be monitored indirectly by monitoring the cardiac activity. The commonly used methods capable of this are Electrocardiography(ECG) and Photoplethysmography(PPG)[50]. **Photoplethysmography (PPG):** It is a non-invasive method of detecting the changes in blood volume of the micro-vessels under the skin. During respiration and cardiac activity, there will be changes in the light absorption between the blood vessels and tissues. By monitoring the change in absorption and using appropriate filters, it is possible to extract both respiration and heart rate simultaneously. Optical sensors are placed on the skin with higher vascular density to detect the difference in light absorption more easily[8, 50].

However, there have been many contactless methods of monitoring respiration either by monitoring skin colour, chest movement or temperature around the nostrils remotely.

- **Thermal Imaging:** The Infrared(IR) camera is generally aimed at the nasal cavity region. This method can be used to measure both breathing rate and exhaled air temperature to monitor the vitals[2, 3].
- **Depth Imaging:** A depth map will contain the information about the distance between the object and the sensor. This works on using ultrasound to map the object space and measure its distance and possibly movement. The camera's sensor is aimed at the chest region to monitor movement during respiration, along with giving a measurement for the respiration phase. However, this process is much slower compared to the other methods[51].
- **Doppler Radar:** It is a Electromagnetic(EM) wave based method which analyze the micro-doppler effect, i.e. change in relative frequency between the source and receiver because of movement between them. So, microwave signals such as pulse signals in Ultra-wideband (UWB) radar or continuous signal in Continuous wave (CW) radar are sent to the target which is the chest region or the thorax of the patient. The targets reflects these signals back and the movement of the target region during respiration causes micro-doppler harmonics which are later analyzed for acquiring respiration rate. This method is also used to acquire the heart rate by using different filters on the same acquired signal. The disadvantage of this method is that the movement of the subject significantly affects the readings[12].
- **Optoelectronic and Structured Light Plethysmography:** Optoelectronic Plethysmography uses a camera and a few markers placed around the chest region. As the camera is tracking these markers, it is not completely a contactless method. However, Structured Light Plethysmography uses this principle with a different application. Light sources project a pattern onto the target. The camera tries to reconstruct the depth map by observing the distortions caused by movement, allowing it to analyze the direction and amount of motion. This is used to monitor the chest activity during respiration remotely. However, this methods assumes that there is no other movement around the chest apart from the breathing activity. This makes it difficult in case of patients who are not still[12].
- **Video Based:** Respiration causes movement on chest or abdomen region, which can be seen in any video source. This makes it possible to extract respiration rate from image/video processing methods like optical flow. Optical flow is a method of tracking the movement of pixels or object in a video frame based on their pixel intensity. This allows the camera to track the pixels of the chest region or the chest ROI during the breathing cycle. This makes it possible to track the chest movement during respiration from a video source even from a great distance(>2m). This method also provides the option to track other body movements too[52].

2.6. Monitoring Cardiac Activity

The Cardiac system consists of the heart and the circulatory system. They are responsible for circulating blood throughout the body; carrying oxygenated blood from the lungs to other organs and de-oxygenated blood back to the lungs. As the health of neonates is very fragile, monitoring vitals like heart/respiration rate etc play a crucial role in their long term health and development. Inaccurate measurements may lead to permanent damage of the body including the brain or even death in some cases, which is why methods for monitoring vitals need to be fast and reliable. There have been many methods to acquire heart rate; either from the blood vessels or from monitoring the heart directly through non-invasive means. The contact based methods of monitoring heart rate are;

- **Electrocardiography (ECG):** Also the gold standard for measuring heart rate, this method measures the electric impulses generated by the heart muscles during each rhythmic contraction and relaxation. There are electrodes on specific points on the body, mainly the chest; and the electric signals read from each sensor is amplified and observed. This method not provides heart rate but also gives the state of the heart from the output waveform[53].
- **Photoplethysmography (PPG):** PPG provides information about both respiration and heart rate by analyzing light absorption of blood vessel regions under the skin. An IR sensor will be placed on the fingertips or the toes and the fluctuations in the skin absorption provides us with the signal for both heart and breath rates[7, 8, 32].
- **Pressure Sensing :** Peizo-electric sensors can detect mechanical strain and convert that into electrical signals. These sensors are placed on the skin where the major blood vessel complex are under the skin,

like the wrist. This is used to detect the changes in blood pressure during the cardiac compression and relaxation cycle, providing the heart rate[54].

- **Phonocardiography :** The heart valves produce sound during contraction and relaxation in every cycle. These sounds can be heard through a stethoscope and microphones that are placed on the chest region closest to the heart. With appropriate filters, this not only provides the heart rate but also any physiological abnormalities can be identified, like murmurs etc[53].

The non-contact based methods of monitoring heart rate are;

- **Doppler Radar :** This method analyzes the reflected EM waves from the body or target region. A filter section is needed to filter the heartbeat and the respiration from the acquired EM wave signal with the micro-doppler harmonics and to deal with the many unwanted reflected signals[55].
- **Laser Doppler Vibrometry :** It is possible to detect skin deflections due to the pressure variations caused by cardiac activity. The signal is extracted by pointing a laser at the region with blood vessel complex under the skin. This signal is examined and the heart rate is derived from the micro-movements of the skin[56].
- **Magnetic Induction:** As the chest region is continuously moving, the impedance of the chest keeps changing. With the poor-conducting air in the lungs and the well-conducting blood in the heart and the blood vessels, the vitals are measured by inducing eddy currents and measuring the re-induced magnetic fields from the chest externally. The same method can be extended to also measuring the capacitance of the body by using electrodes attached to the clothing or the mattress the patient is on; not directly attaching on the patient, and performing similar analysis[57].
- **Ultrasound :** An ultrasonic transmitter and an ultrasonic receiver are installed on both sides of the patient; not directly attaching on the patient, and the signals from the transmitter are modulated by the respiratory and cardiac activities. The receiver picks up on these signal changes and filters out both respiratory and heart rates simultaneously. This methods is slower and requires a lot of filtering and is not reliable in case of any movement from the subject[58].
- **Remote Photoplethysmography (rPPG):** It is possible to acquire the heart rate remotely where a camera will be placed at a distance and the subject will be illuminated with a light source. The camera is able to analyze the entire ROI of the subject and detect those micro-changes from the light reflected by the subject. The diffuse part of the reflected light contains the information about the cardiac activity. The performance of this method depends on the intensity of the incident light source[9, 59].
- **Thermal Image Analysis :** The pulse generated from the heart travels throughout the body through the blood vessels, enabling blood circulation. The blood flow affects the tissue temperature because of the heat exchange between the blood vessels and the surrounding tissue. This effect is more observable around the major superficial blood vessels. Analyzing the temperature change around these blood vessel regions provides the heart rate[15, 21].

2.7. Non-Contact Monitoring of Vitals using Thermal Imaging

Skin is a complex organ that comprises many different cells and cell types. It is a critical physical barrier that protects the body and is responsible for fluid homeostasis, temperature regulation, and sensation. As the skin of the neonates is very fragile, having adhesive sensors with connection wires; as shown in fig.1.1, may cause them more harm than good. The adhesive on these contact sensors will damage the sensitive neonate skin and may also cause sepsis related problems. The same problem will happen for people with damaged skin as this may even hurt them more. In order to avoid these problems, a lot of effort has been put in devising contactless methods for monitoring vitals. Infrared thermography has been a very efficient and preferred method for its non-invasive yet detailed applications.For contactless monitoring in biomedical applications; including thermal imaging, the following methods have been suggested in [11];

- **Near Infrared (NIR) Imaging:** It is of wavelength range between 0.75 μm–1.4 μm. Used for applications like measuring blood perfusion or blood vessel condition, monitoring brain injury etc[60].
- **Short Wave Infrared Imaging (SWIR):** It is of wavelength range between 1.4 μm–3.0 μm. Applications include blood vessels imaging etc[61].

- **Middle and Long Wave Infrared Imaging (MWIR, LWIR):** MWIR is of wavelength range between 3.0 μm–8.0 μm and LWIR is from 8.0 μm-15.0 μm. Theses ranges can be extended to applications like Heart/Breath Rate(HR/BR), stress imaging or emotional classification of a subject etc[3].
- **Photoplethysmography Imaging (PPG):** This method uses sensors to monitor skin perfusion by measuring their difference in spectrum absorption. This is because of the pressure difference in blood vessels caused by cardio/respiratory activities. It can be used for applications like measuring HR/BR to hemodynamic monitoring, oxygen consumption etc[60].
- **Neonatal Imaging with Visible Light:** Monitoring of physiological signal such as heart rate, peripheral blood pressure and blood perfusion[63].
- **Embedding Contactless Imaging inside Incubator:** It involves embedding several physiological monitoring and imaging sensors inside the neonatal incubator. Applications include IR imaging, Magnetic impedance tomography (MIT) etc[1, 62].

2.8. Signal Analysis Methods

2.8.1. Power Spectral Density using Periodogram

A **Periodogram** is a method used to calculate the power spectral density (PSD) of a signal using Discrete Fourier Transform(DFT) to perform spectral analysis on the signal. The spectral analysis is done using combination of different methods like *windowing methods* and *zero-padding* before computing the DFT.

Windowing is a method for tapering the signal at the ends in order to reduce *spectral leakage* caused during frequency analysis. As seen in fig.2.5, there is a sine wave of 4Hz sampled for 1 sec duration. The sampling frequency o the signal is 100Hz. The fourier transform of the signal can be seen in fig.2.6 where it is clearly visible that the frequency component in the signal is 4Hz.

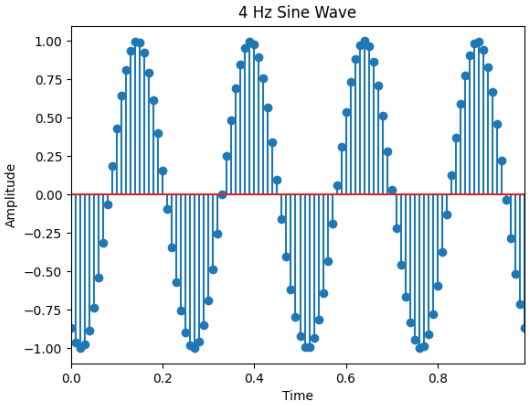

Figure 2.5: 4Hz Sine Wave

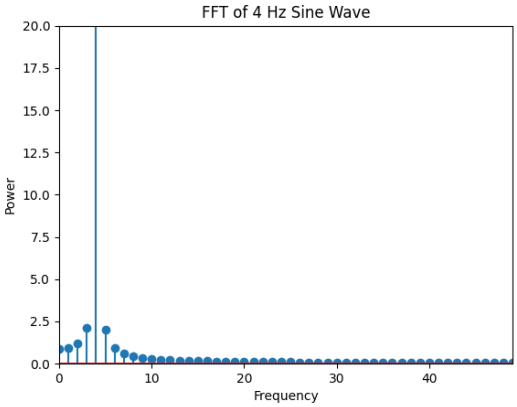

Figure 2.6: DFT of 4Hz Sine Wave

However instead of 1 sec if the signal is sampled for 0.9 sec; as shown in fig.2.7, then the fourier transform of this case is not as clear as the case when it was sampled for 1 sec as seen in fig.2.8. There are other frequency components that are visible despite there being only one frequency component. Although the 4Hz component has the highest amplitude in fig.2.8, the other components have amplitude comparable to the true value which is undesirable.

If there are multiple frequency components present in the signal then these undesirable components affect the observed results from the true value and that can affect the performance of the application. This is called as spectral leakage, where there are undesirable frequency components in the fourier transform that should not exist because the sampling duration and the time-period of the frequency components are not integer factors of each other.

In practical situations; as the frequency components present in the signal are not known beforehand, knowing the ideal sampling duration would be difficult. Another alternative would be to have the sampling dura-

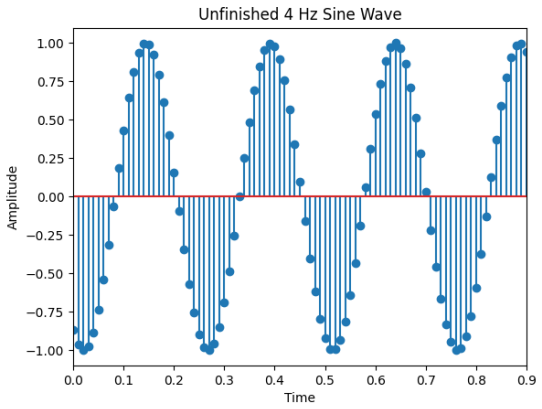

Figure 2.7: Unfinished 4Hz Sine Wave

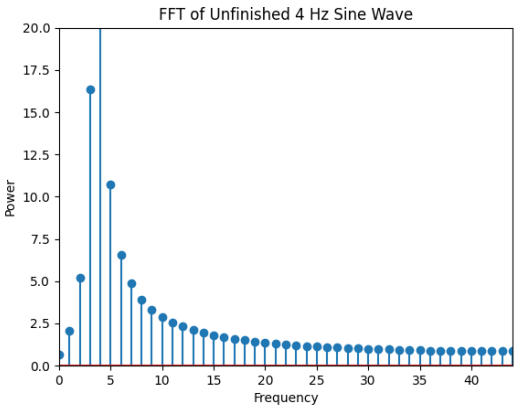

Figure 2.8: DFT of Unfinished 4Hz Sine Wave

tion as large as possible to prevent spectral leakage but that will not be applicable for real-time situation and for non-stationary signals where the frequency components tend to change. So in order to reduce the spectral leakage, a windowing function is applied to the signal in order to taper the ends which would contribute to the spectral leakage.

As seen in fig.2.9, the incomplete sine wave sampled for 0.9 sec is multiplied with a Hamming window as shown in fig.2.15. The fourier analysis of the signal after windowing the signal; as shown in fig.2.10, shows a reduction in the undesirable frequency components as compared to not applying any windowing function.

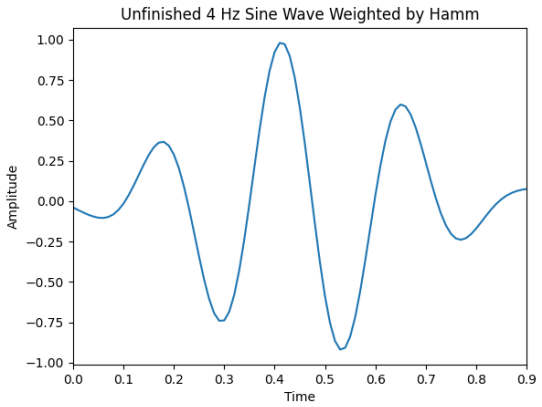

Figure 2.9: Unfinished 4Hz Sine Wave after Hamming Window

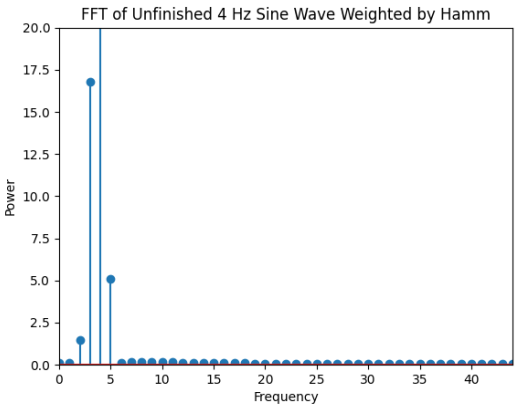

Figure 2.10: DFT of Hamming Window Unfinished 4Hz Sine Wave

There are many different windowing functions but the ones that will be used for this project are as follows;

- **Boxcar :** This window is equivalent to not applying any tapering or window to the signal. The window function *w[n]* can be defined as;

$$w[n] = 1\,, \quad where \quad 0 \leq n < N \tag{2.32}$$

  where N is the length of the window.

  The plot of the window w[n] can be seen in fig.2.11 with its respective frequency response in fig.2.12.

- **Triangular :** This window is a triangle, symmetrical at the centre of the signal. The window function *w[n]* can be defined as;

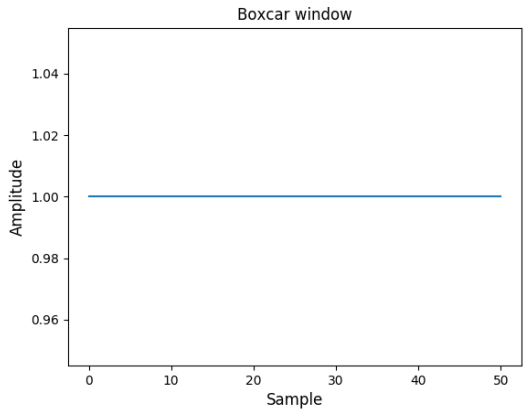

Figure 2.11: Boxcar Window Signal

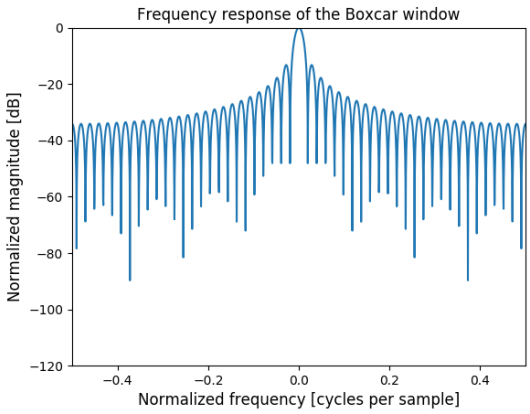

Figure 2.12: Boxcar Window Frequency Response

$$w[n] = 1 - \left| \frac{n - \frac{N}{2}}{\frac{N}{2}} \right|, \quad where \quad 0 \leq n < N \tag{2.33}$$

where N is the length of the window.

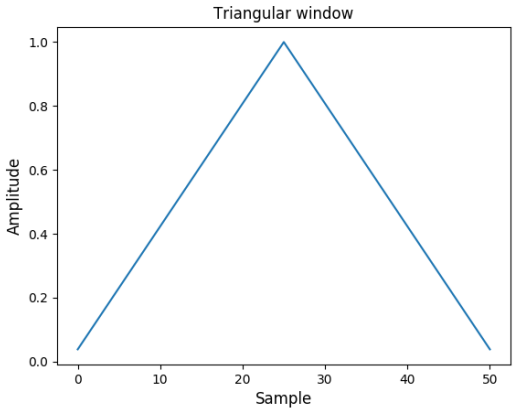

Figure 2.13: Triangular Window Signal

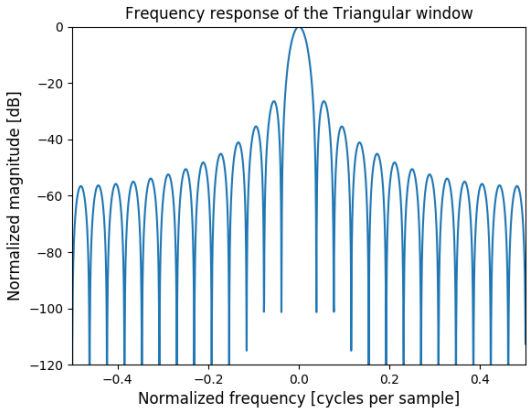

Figure 2.14: Triangular Window Frequency Response

The plot of the window w[n] can be seen in fig.2.13 with its respective frequency response in fig.2.14.

- **Hamming :** This is one of the most commonly used windowing functions. The window function *w[n]* can be defined as;

$$w[n] = 0.54 - 0.46\, cos\left(\frac{2\pi n}{N-1}\right), \quad where \quad : 0 \leq n < N \tag{2.34}$$

where N is the length of the window.

The plot of the window w[n] can be seen in fig.2.15 with its respective frequency response in fig.2.16.

- **Hann :** This windowing functions is commonly abbreviated as *Hanning* window. The window function *w[n]* can be defined as;

$$w[n] = 0.5 - 0.5\, cos\left(\frac{2\pi n}{N-1}\right), \quad where \quad 0 \leq n < N \tag{2.35}$$

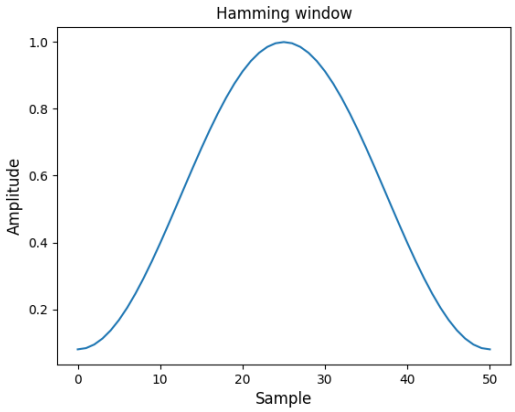

Figure 2.15: Hamming Window Signal

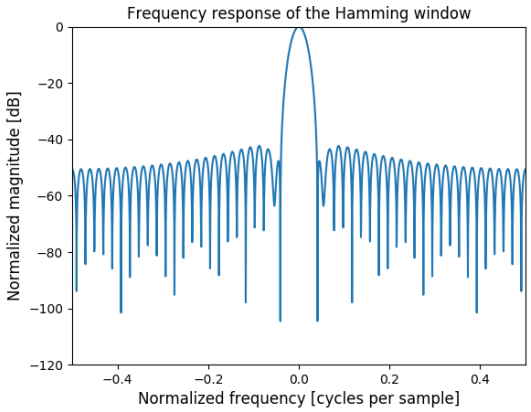

Figure 2.16: Hamming Window Frequency Response

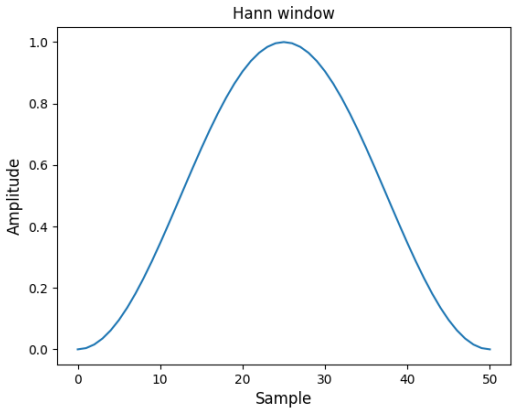

Figure 2.17: Hann Window Signal

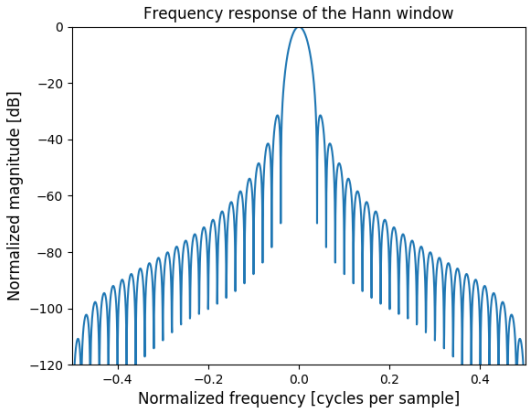

Figure 2.18: Hann Window Frequency Response

where N is the length of the window.

The plot of the window w[n] can be seen in fig.2.17 with its respective frequency response in fig.2.18.

- **Blackman-Harris :** The window function *w[n]* can be defined as;

$$w[n] = 0.35875 - 0.48829\,cos\left(\frac{2\pi n}{N-1}\right) + 0.14128\,cos\left(\frac{4\pi n}{N-1}\right) - 0.01168\,cos\left(\frac{6\pi n}{N-1}\right), \quad where \quad 0 \le n < N \tag{2.36}$$

where N is the length of the window.

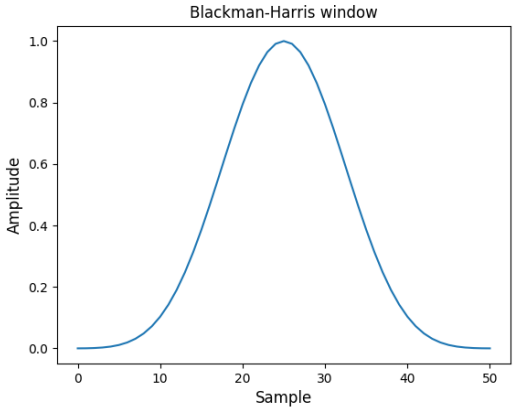

Figure 2.19: Blackman-Harris Window Signal

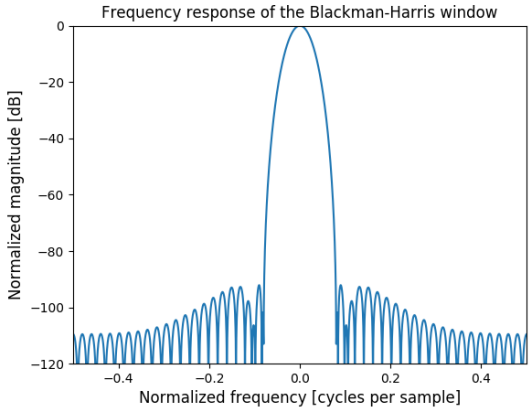

Figure 2.20: Blackman-Harris Window Frequency Response

The plot of the window w[n] can be seen in fig.2.19 with its respective frequency response in fig.2.20.

- **Bohman :** The window function *w[n]* can be defined as;

$$w[n] = \left(1 - \left|\frac{n-\frac{N}{2}}{\frac{N}{2}}\right|\right)cos\left(\pi\left|\frac{n-\frac{N}{2}}{\frac{N}{2}}\right|\right) + \frac{1}{\pi}sin\left(\pi\left|\frac{n-\frac{N}{2}}{\frac{N}{2}}\right|\right), \quad where \quad 0 \le n < N \tag{2.37}$$

where N is the length of the window.

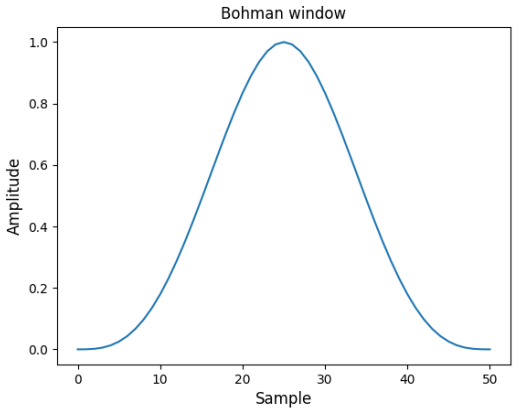

Figure 2.21: Bohman Window Signal

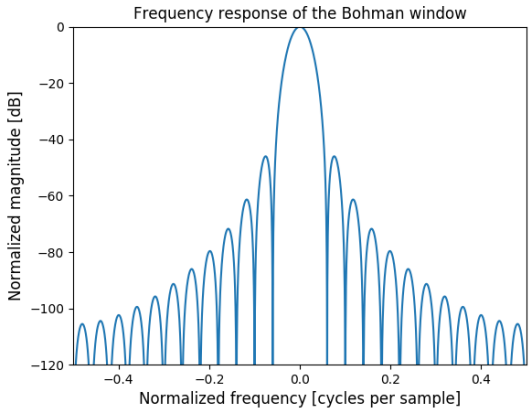

Figure 2.22: Bohman Window Frequency Response

The plot of the window w[n] can be seen in fig.2.21 with its respective frequency response in fig.2.22.

- **Flattop :** The window function *w[n]* can be defined as;

$$w[n] = 0.21557895 - 0.41663158\,cos\left(\frac{2\pi n}{N-1}\right) + 0.277263158\,cos\left(\frac{4\pi n}{N-1}\right) - 0.083578947\,cos\left(\frac{6\pi n}{N-1}\right) + 0.0066947368\,cos\left(\frac{8\pi n}{N-1}\right), \quad where \quad 0 \le n < N \tag{2.38}$$

where N is the length of the window.

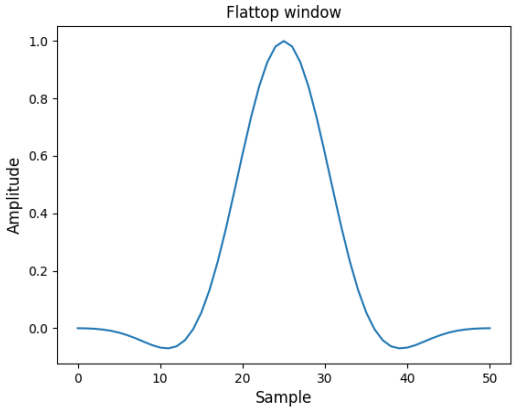

Figure 2.23: Flattop Window Signal

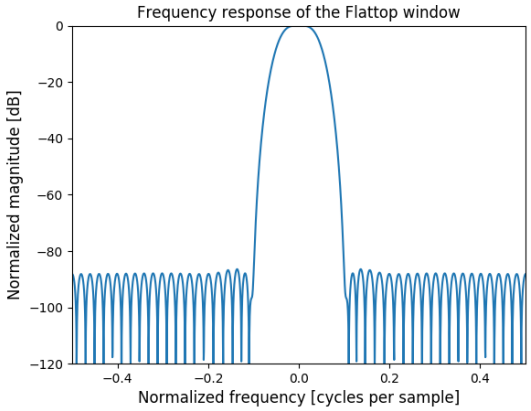

Figure 2.24: Flattop Window Frequency Response

The plot of the window w[n] can be seen in fig.2.23 with its respective frequency response in fig.2.24.

- **Parzen :** The window function *w[n]* can be defined as;

$$w[n] = \begin{cases} 1 - 6\left(\frac{|2n|}{N}\right)^2 + 6\left(\frac{|2n|}{N}\right)^3 & : 0 \le |n| \le \frac{N-1}{4} \\ 2\left(1 - \frac{|2n|}{N}\right)^3 & : \frac{N-1}{4} < |n| \le \frac{N-1}{2} \\ \\ where \quad -\frac{N-1}{2} \le n \le \frac{N-1}{2} \end{cases} \tag{2.39}$$

where N is the length of the window.

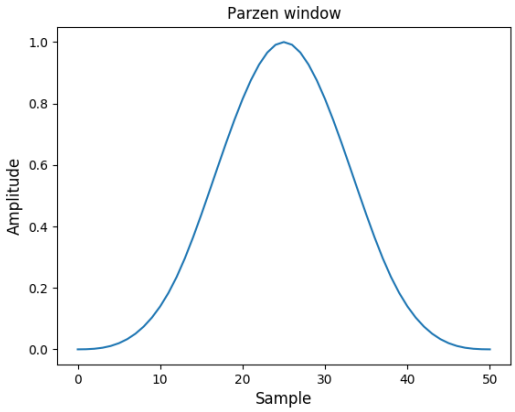

Figure 2.25: Parzen Window Signal

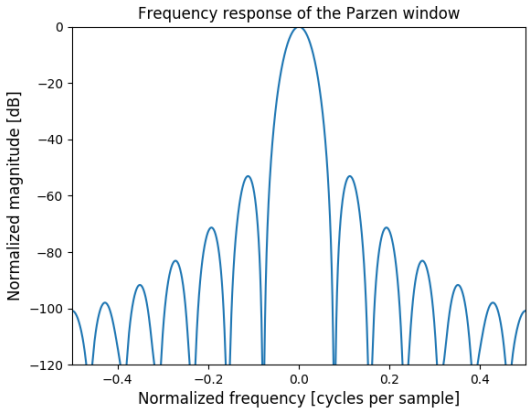

Figure 2.26: Parzen Window Frequency Response

The plot of the window w[n] can be seen in fig.2.25 with its respective frequency response in fig.2.26.

- **Nuttall :** The window function *w[n]* can be defined as;

$$w[n] = 0.355768 - 0.487396\,cos\left(\frac{2\pi n}{N-1}\right) + 0.144232\,cos\left(\frac{4\pi n}{N-1}\right) - 0.012604\,cos\left(\frac{6\pi n}{N-1}\right), \quad where \quad 0 \le n < N \tag{2.40}$$

where N is the length of the window.

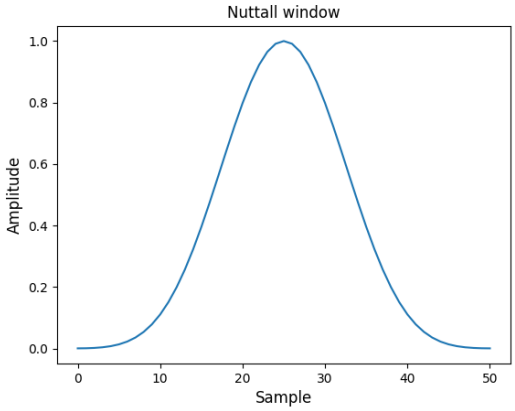

Figure 2.27: Nuttall Window Signal

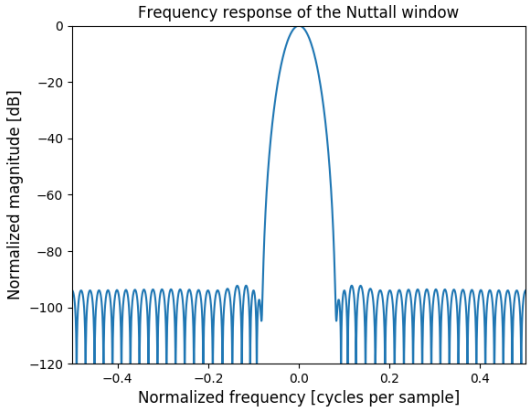

Figure 2.28: Nuttall Window Frequency Response

The plot of the window w[n] can be seen in fig.2.27 with its respective frequency response in fig.2.28.

- **Bartlett-Hann :** This windowing function is a combination of the Bartlett (another type of rectangular window) and the Hann window. The window function *w[n]* can be defined as;

$$w[n] = 0.62 - 0.48\left|\frac{n}{N-1} - \frac{1}{2}\right| - 0.38\,cos\left(\frac{2\pi n}{N-1}\right), \quad where \quad 0 \le n < N \tag{2.41}$$

where N is the length of the window.

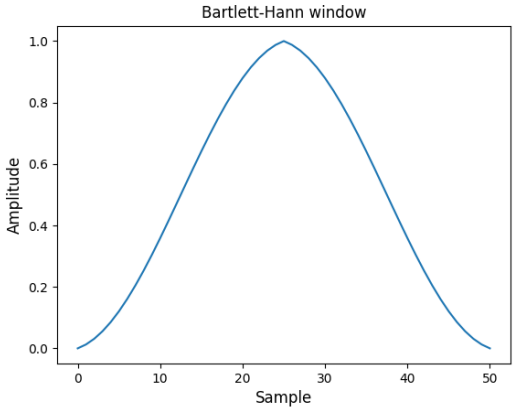

Figure 2.29: Bartlett-Hann Window Signal

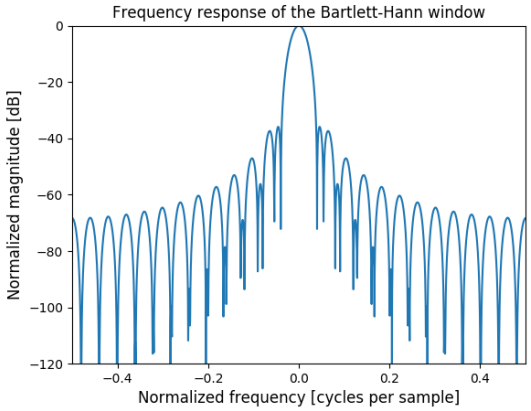

Figure 2.30: Bartlett-Hann Window Frequency Response

The plot of the window w[n] can be seen in fig.2.29 with its respective frequency response in fig.2.30.

- **Kaiser :** The window function *w[n]* can be defined as;

$$w[n] = \frac{I_0\left(\beta\sqrt{1-\frac{4n^2}{(N-1)^2}}\right)}{I_0(\beta)}, \quad where \quad -\frac{N-1}{2} \leq n \leq \frac{N-1}{2} \tag{2.42}$$

where N is the length of the window and $\beta \geq 0$ is the shaping parameter used to determine the trade-off between the main lobe width and the side lobe attenuation and I_0 is a zero-degree Bessel function.

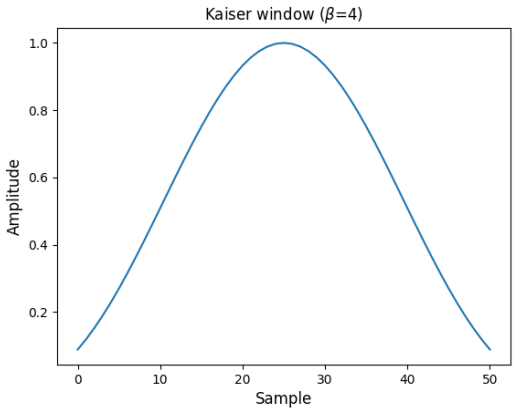

Figure 2.31: Kaiser Window Signal for $\beta = 4$

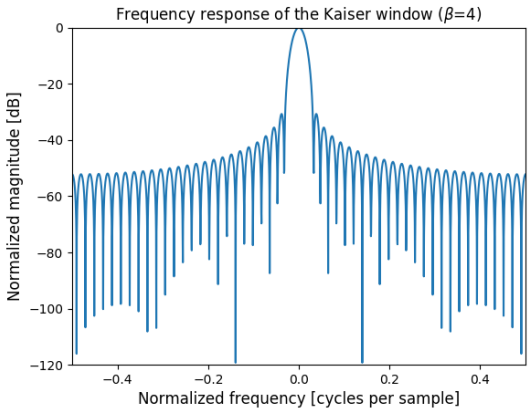

Figure 2.32: Kaiser Window Frequency Response for $\beta = 4$

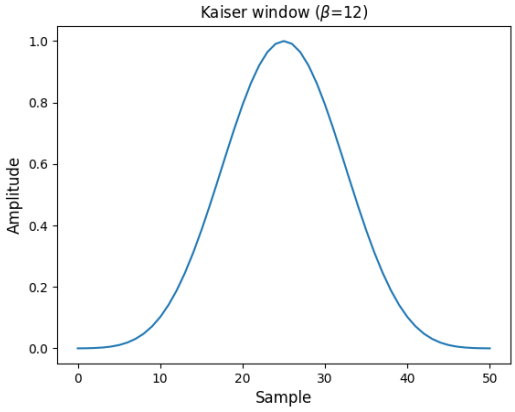

Figure 2.33: Kaiser Window Signal for $\beta = 12$

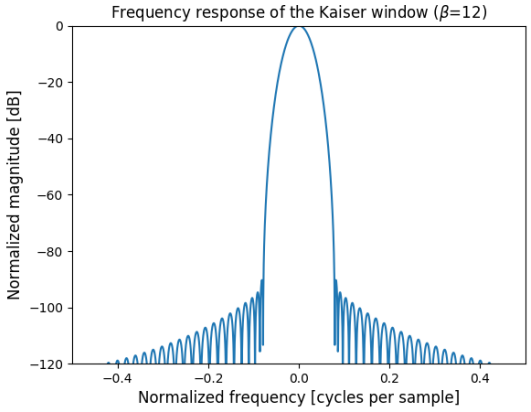

Figure 2.34: Kaiser Window Frequency Response for $\beta = 12$

The plot of the window w[n] for $\beta = 4, 12$ can be seen in fig.2.31,2.33 with its respective frequency response in fig.2.32,2.34.

- **Dolph-Chebyshev :** Unlike the other windows, this window is defined in the frequency domain with a set attenuation factor. The window function *W[k]* is defined as;

$$W[k] = cos\left(M\,cos^{-1}\left(\beta cos(\tfrac{\pi k}{M})\right)\right) \Big/ cosh(M\,cos^{-1}(\beta))$$
$$where \quad \beta = cosh\left(\tfrac{1}{M} cosh^{-1}\left(10^{\frac{A}{20}}\right)\right) \tag{2.43}$$
$$0 \leq k < M$$

where; M is the length of the signal and A is the attenuation factor for the window.

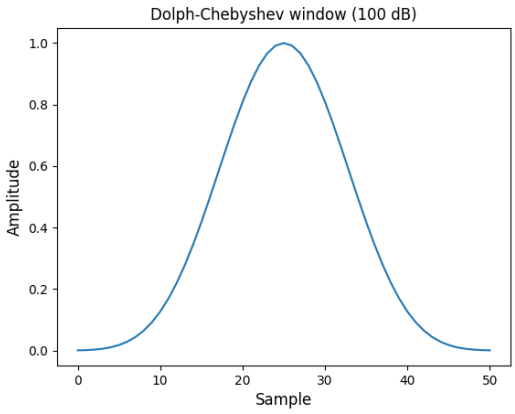

Figure 2.35: Dolph-Chebyshev Window Signal

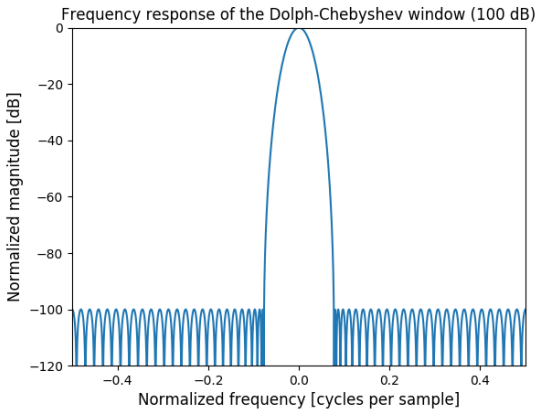

Figure 2.36: Dolph-Chebyshev Window Frequency Response

The plot of the window W[k] for attenuation of 100dB can be seen in fig.2.36 with its respective signal in the time-domain in fig.2.35.

- **Tukey :** The window function *w[n]* can be defined as;

$$w[n] = \begin{cases} \frac{1}{2}\left(1 - cos\left(\frac{2\pi n}{\alpha N}\right)\right) & where \quad 0 \le n < \frac{\alpha N}{2} \\ 1 & where \quad \frac{\alpha N}{2} \le n \le \frac{N}{2} \\ w[N-n] & where \quad \frac{N}{2} < n < N \end{cases} \tag{2.44}$$

where N is the length of the window and $0 \le \alpha \le 1$ is the shape parameter for the window.

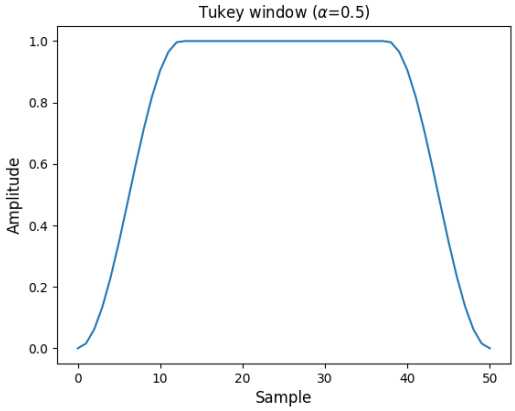

Figure 2.37: Tukey Window Signal for $\alpha = 0.5$

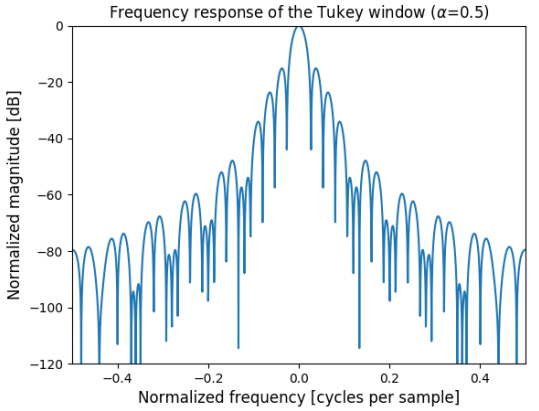

Figure 2.38: Tukey Window Frequency Response for $\alpha = 0.5$

If $\alpha = 0$, then the window is equivalent to a Boxcar window and if $\alpha = 1$, then it is equivalent to a Hann window. The plot of the window w[n] for $\alpha = 0.8, 0.5$ can be seen in fig.2.37,2.39 with its respective frequency response in fig.2.38,2.40.

In case of windowing methods, there is always a trade-off on the frequency resolution determined by the main lobe width and the side lobe attenuation. The other windowing methods try to compensate for the lower side lobe attenuation at the price of the main lobe width. As seen in fig.2.31,2.33, increasing β will improve the side lobe attenuation but also increase the main lobe width.

In table 2.1, the normalized main lobe width and the average side lobe attenuation for each of the windowing methods considered for this project are mentioned. The Boxcar window has the lowest main lobe width compared to the other windows; as shown in table.2.1, giving it better frequency resolution but its side lobe

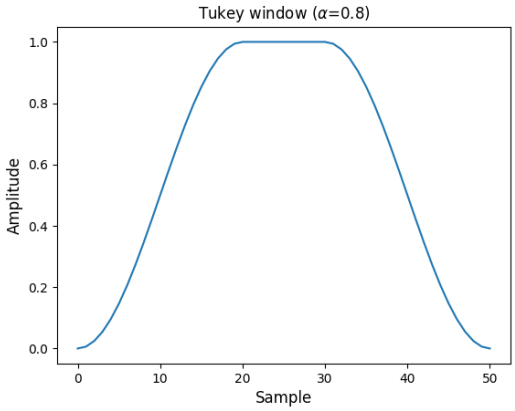

Figure 2.39: Tukey Window Signal for $\alpha = 0.8$

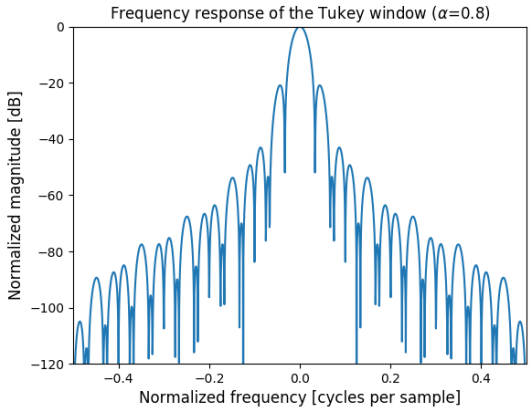

Figure 2.40: Tukey Window Frequency Response for $\alpha = 0.8$

Windowing Method	Normalized Main Lobe Width(Hz)	Avg. Side Lobe Attenuation(dB)
Boxcar	0.01978505	35.23815253
Triangular	0.03883732	60.02994046
Hamming	0.04127992	53.632151
Hann	0.04030288	81.65662472
Blackman-Harris	0.0803615	109.5293241
Bohman	0.06033219	97.81854319
Flattop	0.10332193	94.10716757
Parzen	0.07840743	96.89967634
Nuttall	0.0828041	99.75401848
Bartlett-Hann	0.04030288	70.73104972
Kaiser($\beta = 4$)	0.03297509	53.68559298
Kaiser($\beta = 8$)	0.05495848	87.31320733
Kaiser($\beta = 12$)	0.07938447	117.3135847
Dolph-Chebyshev	0.07791891	106.0603349
Tukey($\alpha = 0.5$)	0.02711285	68.39904645
Tukey($\alpha = 0.8$)	0.03346361	78.77288866

Table 2.1: Comparison of behaviour of different windowing methods in frequency domain

attenuation is poor which contributes to the spectral leakage while the Flattop window has one of the lowest side lobe attenuation but also the largest main lobe width among all the windows; compromising on its frequency resolution. The diversity of the windowing methods helps better explore the nature of the signal and to see which characteristics are better suited for the algorithm's performance.

Zero-padding is the method of appending zeros to the signal after the signal is multiplied by a windowing function and before calculating the DFT of the signal in order to increase the length of the density of the samples in the frequency domain.

In order to show the effects of zero-padding, a sine wave defined as;

$$
\begin{gathered}
y = \sum_{n=1}^{6} A[n] * sin(2\pi * fa[n]\, x) \\
where; \\
A = [0.5, 0.5, 0.5, 0.75, 1, 0.5] \\
fa = [1.1, 1.15, 1.5, 1.55, 2.1, 2.15] \\
x = [0, 1/fs, 2/fs, 3/fs, ..., 15] \\
fs = 9
\end{gathered}
\tag{2.45}
$$

In equation 2.45, *fa* are the frequency components composing the sine wave with A being their respective amplitudes. The signal was generated with a sampling frequency of 9Hz; similar to the camera's frame rate, with a period of 15 sec which is used to generate the time axis x in equation 2.45. This would mean that when the DFT for equation 2.45 is performed, then there should be 6 distinct peaks visible in the transform. However, as we see in fig.2.41, there are only 3 peaks visible. This is because some of the frequencies are only 50mHz apart from each other and because a 15 sec window would give a resolution of only 67mHz, the components too close to each other could not be distinguished and ended up as one frequency. After zero-padding to the same length as the original signal, the DFT is able to distinguish between the frequencies that were too close to each other and otherwise were not detected earlier; as shown in fig.2.42.

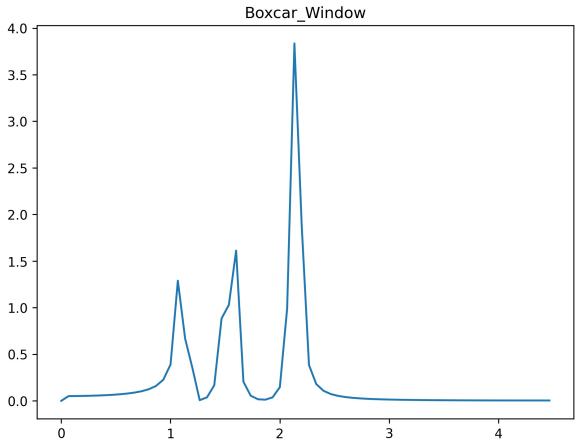

Figure 2.41: DFT of equation 2.45

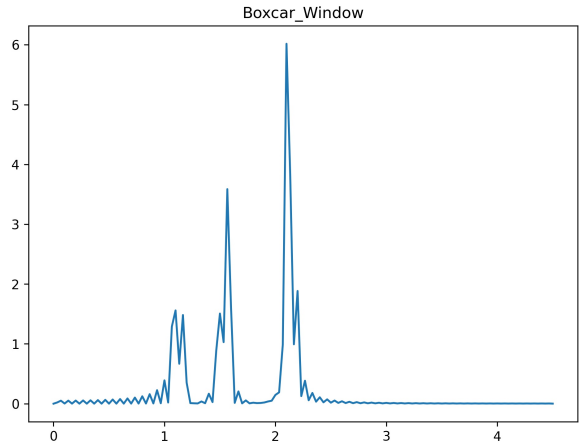

Figure 2.42: DFT of equation 2.45 after Zero-Padding

This demonstrates how zero-padding can improve the frequency resolution of the signal but there is a drawback to this method. In fig.2.42, there are unwanted frequency components that appear near the peaks. These harmonics are the consequence of zero-padding and they can affect the output for a more complex signal from real scenarios. For DFT in fig.2.41 and fig.2.42, the Boxcar window was used. So in order to reduce the harmonics that appear because of zero-padding, using a widow with better side lobe attenuation will reduce them and provide us with better results. After using a Tukey window instead of Boxcar and zero-padding to the length of the original signal; as shown in fig.2.43, there was significant reduction in the harmonics because of higher side lobe attenuation but zero-padding does not appear to be as effective as in case of using Boxcar window in terms of frequency resolution. Increasing the zero-padding to two times the length of the original signal after applying Tukey window did improve the results slightly; as seen in fig.2.44, but it is still not as distinctive as in case of using the Boxcar window. Also, increasing the zero-padding also increases the amount of

computation by the factor of its increment. So, zero-padding must not be done by a really large factor for its effects on the computational load and also in the DFT output. So, for this project zero-padding will be done to only four times the length of the original signal; each paired with 16 different windowing methods.

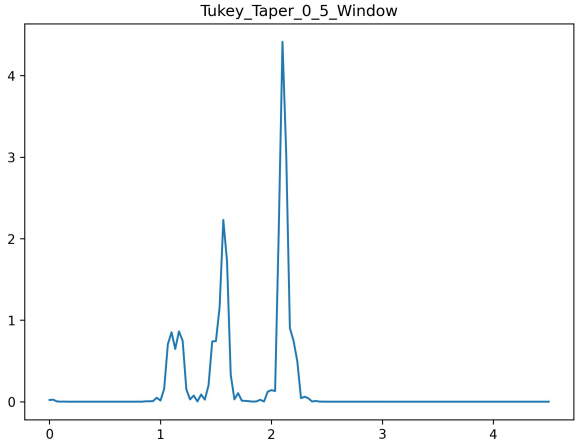

Figure 2.43: DFT of equation 2.45 after using Tukey ($\alpha = 0.5$) window and zero-padding to the length of the original signal

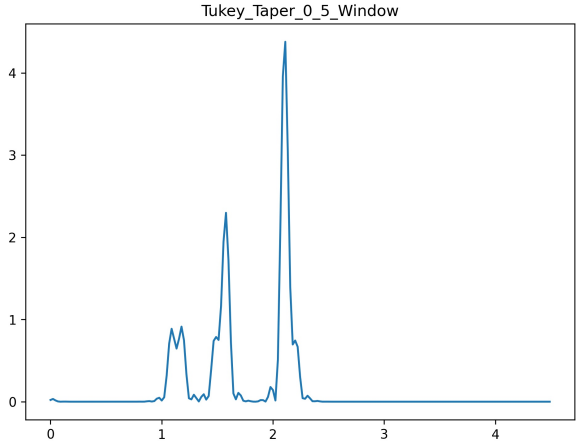

Figure 2.44: DFT of equation 2.45 after using Tukey ($\alpha = 0.5$) window and zero-padding two times the length of the original signal

2.8.2. Welch Periodogram

The *Welch* periodogram; also called as an averaging periodogram, is an improvement on the standard periodogram discussed in the earlier section where the signal whose spectral analysis needs to be performed is divided into equal segments; as shown in fig.2.45, and a standard periodogram is performed on each segment; with windowing and zero-padding, and the results of all segments is merged by averaging; as mentioned in [43]. As the segments are of equal length, the periodogram output of each segment will have the same number of components for the same bandwidth resolution; depending on the sampling rate of the signal. This method is advantageous in order to remove any spectral noise and see which frequency components are recurring among all the segments. As the length of the signal being analyzed by the periodogram is lower that the original length of the signal, the bandwidth resolution of the output will be lower than performing a simple periodogram on the whole signal.

The Welch periodogram depends on the following parameters;

- **Size of each segment**: It has to be lower than or equal to length of the original signal. If the size of the segment is the same as the length of the original signal, then it is equivalent to using a standard periodogram. In fig.2.45, it is potrayed as variable K.
- **Sliding of window between segments**: This determines by how much the segments slides over the whole signal to define another segment.In fig.2.45, it is potrayed as variable Q.
- **Windowing method and zero-padding**: As periodograms are computed for each of the segments, they are also dependent on factors like windowing methods and zero-padding. As shown in fig.2.45, a Hann window is applied to each segment.
- **Mean or median analysis**: The common method is to average the output of all periodograms. However, it is also possible to calculate the median of all periodograms. As all periodograms are of equal length, the mean or median for the values at the same index of the periodograms is computed and merged into one final periodogram which would be the output. For this project, only the averaging of the periodograms will be used.

In fig.2.46, the periodogram of a noisy sine wave of frequency 1500Hz and sampling frequency of 1KHz is shown. The signal was sampled for a 100 sec duration, leading to 100K samples. Even though the relevant frequency component is clearly visible, the noise in the signal is also significant. In order to reduce the contribution of the white noise in the spectral analysis, the Welch periodogram was performed with the following parameters;

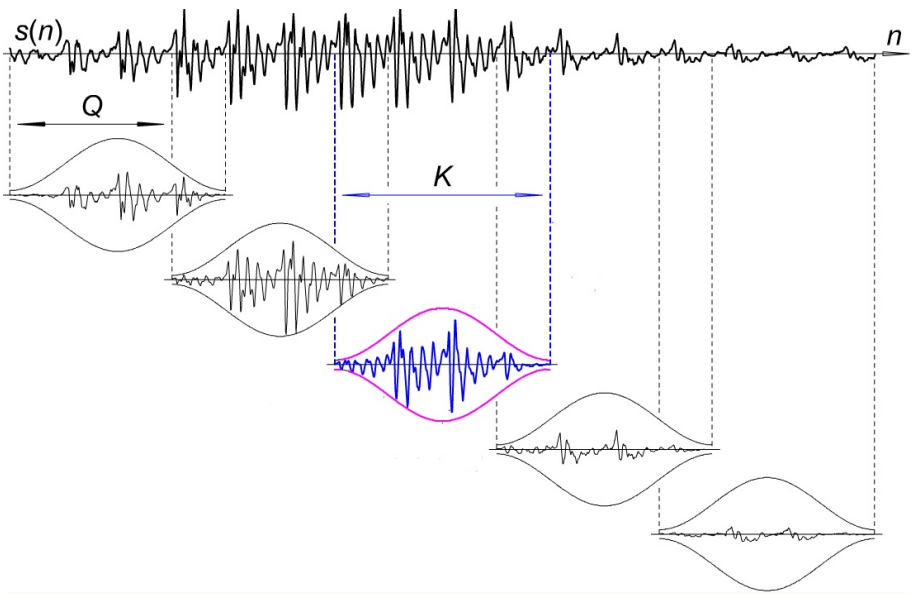

Figure 2.45: Taking segments of signal s(n) for Welch periodogram

- The length of each segment was 1024 samples
- Sliding of window was 512 samples
- Hann window was used with no zero-padding
- Mean analysis was performed on the resulting periodograms of the segments.

The result of the Welch periodogram can be seen in fig.2.47, where the white noise contribution is lower as compared to fig.2.46. Hence, the Welch periodogram can be used to reduce Gaussian noise in the spectral analysis output and could help provide better results.

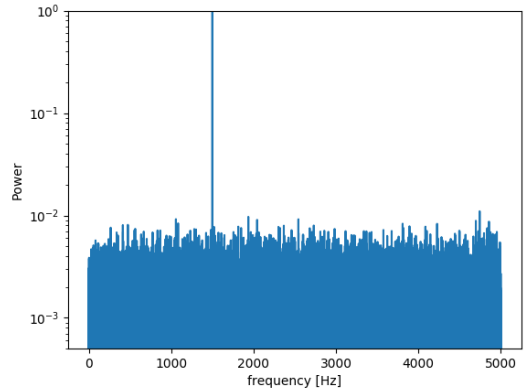

Figure 2.46: Standard Periodogram using Hann Window

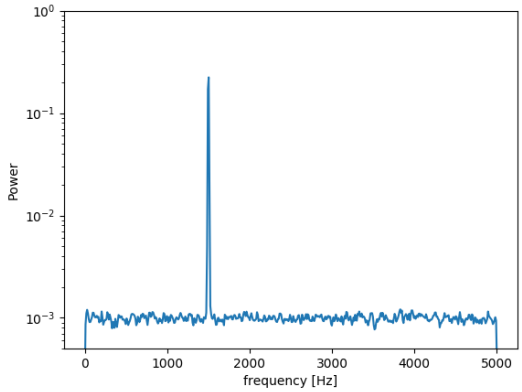

Figure 2.47: Welch Periodogram using Hann Window

2.8.3. Lomb-Scargle Periodogram

The Lomb-Scargle periodogram is a least-squares spectral analysis method where the spectral power of the frequncy components is based on a least squares fit of sinusoidal waves of required frequencies to the sample signal; as mentioned in [44, 45]. Unlike the other periodograms where the frequency vector is dependent on the sampling frequency, the range of frequencies is exclusively specified by the user and the Lomb-Scargle algorithm compares the signal with each of these frequencies and provides an output for the spectral analysis of the signal similar to the other methods. Unlike the other methods, the signal does not need to be sampled at

equal durations for Lomb-Scargle periodogram. So the instances when each sample for the signal was taken also needs to be recorded. This methods also does not use different windowing methods or zero-padding.

Suppose there is a signal X which is sampled at instances t. For a specified frequency ω, first the time delay factor τ for the signal needs to be calculated by using the equation 2.46[45].

$$tan2\omega\tau = \Big[\sum_j sin2\omega t_j\Big] \Big/ \Big[\sum_j cos2\omega t_j\Big] \tag{2.46}$$

Once the time delay factor τ is calculated, then the spectral power $P_n(f)$ of the specified frequency ω is calculated by using the equation 2.47[45].

$$\begin{aligned} P_n(f) = \frac{1}{2}\Bigg\{ &\Big[\sum_j X_j cos\omega(t_j-\tau)\Big]^2 \Big/ \Big[\sum_j X_j cos^2\omega(t_j-\tau)\Big] \\ &+\Big[\sum_j X_j sin\omega(t_j-\tau)\Big]^2 \Big/ \Big[\sum_j X_j sin^2\omega(t_j-\tau)\Big]\Bigg\} \end{aligned} \tag{2.47}$$

In order to calculate the Lomb-Scargle periodogram, a list of ω are specified and using equations 2.46,2.47 the spectral power $P_n(f)$ for each of those frequencies is calculated and this provides us with the spectral analysis output for the signal.

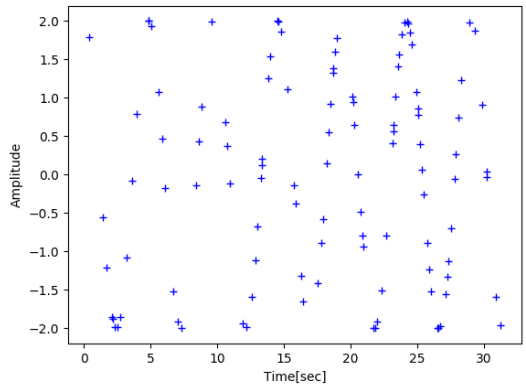

Figure 2.48: Unevenly sampled 1.3Hz sine wave

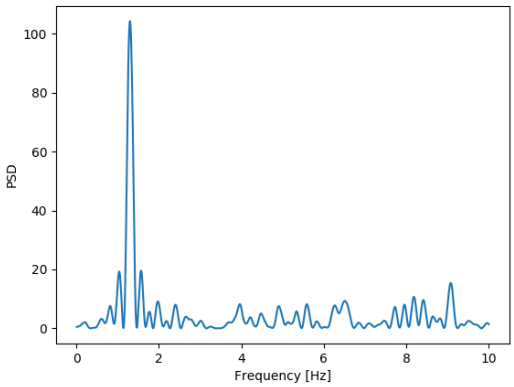

Figure 2.49: PSD output of unevenly sampled 1.3Hz sine wave using Lomb-Scargle method

In fig.2.48, there is an unevenly sampled sine wave of frequency 1.3Hz which appears to be a random set of points. In order to compute the PSD of the signal using Lomb-Scargle's method, a set of 1000 frequencies ranging from 0.01Hz to 10Hz were selected and the spectral analysis was done for the signal. In fig.2.49, there is a distinctive peak at 1.3Hz which is the frequency of the signal.

The Lomb-Scargle's method is clearly useful for practical situations where the sensor data is not sampled at equal intervals. However; given the nature and complexity of this method, a large signal size or a large set of frequencies contribute to greater computational load as compared to Welch or standard periodogram. So, this method must be used cautiously for real-time applications.

2.8.4. Polyphase FFT Filterbank

A Polyphase FFT Filterbank; also known as a *Channelizer*, is an array of filters that divide an input signal into multiple components; one for each filter and then decimate them by the same factor as the number of filters. The filter used for this method will be a polyphase bandpass filters.

Let there be an N_{th} order FIR filter; N being an odd number, whose transfer function can be expressed as;

$$H(z) = h_0 + h_1 z^{-1} + h_2 z^{-2} + h_3 z^{-3} + \ldots\ldots\ldots h_{N-1} z^{-(N-1)}$$

However, the above transfer function can be expressed as a sum of two different transfer functions shown in

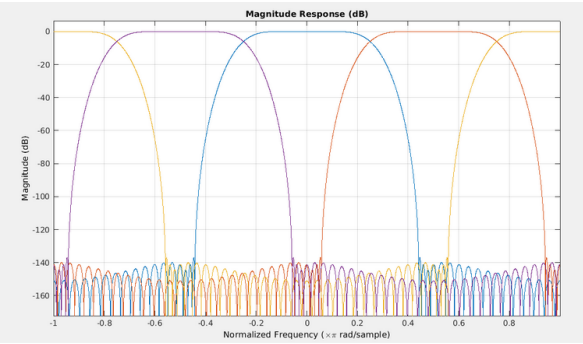

Figure 2.50: Channelizer with 4 bands

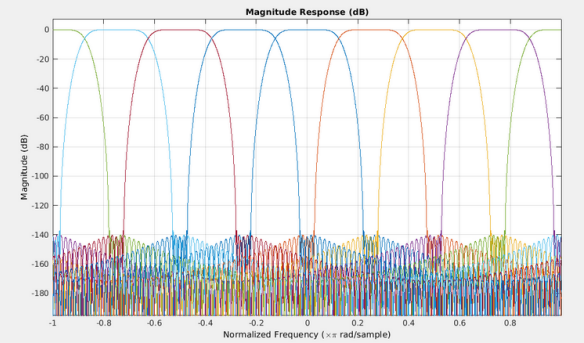

Figure 2.51: Channelizer with 8 bands

[46] as;

$$\begin{aligned} H(z) &= h_0 + h_2 z^{-2} + h_4 z^{-4} + \ldots\ldots\ldots h_{N-3} z^{-(N-3)} + h_{N-1} z^{-(N-1)} \\ &\quad + h_1 z^{-1} + h_3 z^{-3} + \ldots\ldots\ldots h_{N-4} z^{-(N-4)} + h_{N-2} z^{-(N-2)} \\ &= h_0 + h_2 z^{-2} + h_4 z^{-4} + \ldots\ldots\ldots h_{N-3} z^{-(N-3)} + h_{N-1} z^{-(N-1)} \\ &\quad + z^{-1}(h_1 + h_3 z^{-2} + \ldots\ldots\ldots h_{N-4} z^{-(N-5)} + h_{N-2} z^{-(N-3)}) \\ &= E_0(z^2) + z^{-1} E_1(z^2) \end{aligned} \tag{2.48}$$

$$\begin{aligned} &where; \\ E_0(z) &= h_0 + h_2 z^{-1} + h_4 z^{-2} + \ldots\ldots\ldots h_{N-3} z^{-(N-3)/2} + h_{N-1} z^{-(N-1)/2} \\ E_1(z) &= h_1 + h_3 z^{-1} + \ldots\ldots\ldots h_{N-4} z^{-(N-5)/2} + h_{N-2} z^{-(N-3)/2} \end{aligned}$$

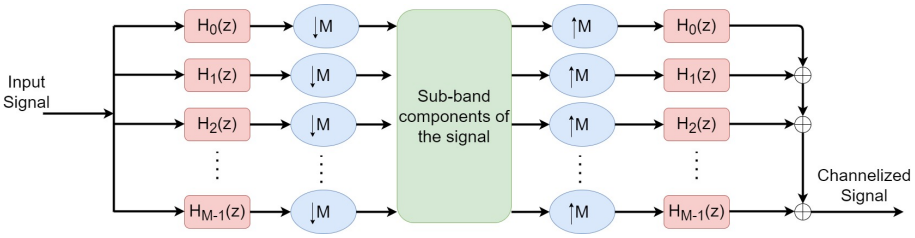

Figure 2.52: Working of a channelizer and signal reconstruction after channelizing the input signal

As shown earlier, the FIR filter *H(z)* is split into two polyphase filters $E_0(z)$ and $E_1(z)$. This can also be extended to more than two polyphase filters i.e. $E_0(z)$, $E_1(z)$ .... $E_{M-1}(z)$ [46];

$$\begin{aligned} H(z) &= \sum_{k=0}^{M-1} z^{-k} E_k(z^M) \\ &where; \\ E_k(z) &= \sum_{0=0}^{[N/M]} h_{Mn+k} z^{-n};\ \ 0 \le k \le M-1 \end{aligned} \tag{2.49}$$

where; **N** is the number of filter coefficients and **M** is the number of polyphase filters to be created.

In a channelizer, there will be a series of equally spaced polyphase bandpass filters; depending on the number of bands the signal needs to divided into (usually an exponent of 2), as shown in fig.2.50, 2.51.

The input signal is simultaneously passed through each of those polyphase filters simultaneously; as shown in fig.2.52, and then the signal is downsampled by the same factor s the number of filters. This gives a row of signals, each containing the output from it's sub-band processing. The channelized signal is constructed by upsampling the sub-band signal components by the same factor they were downsampled with and passing them to the same set of polyphase filters respectively and then adding the outputs. In order to implement a

series of bandpass filters, a set of low-pass filter coefficients are specified to control the nature of all polyphase filters being used.

Unlike the windowing methods which have a trade-off on the main-lobe width and the side-lobe attenuation, the channelizer is used to provide both frequency resolution and side-lobe attenuation. Although, depending on the number of bands, it could be too computationally intensive to do it in real-time.

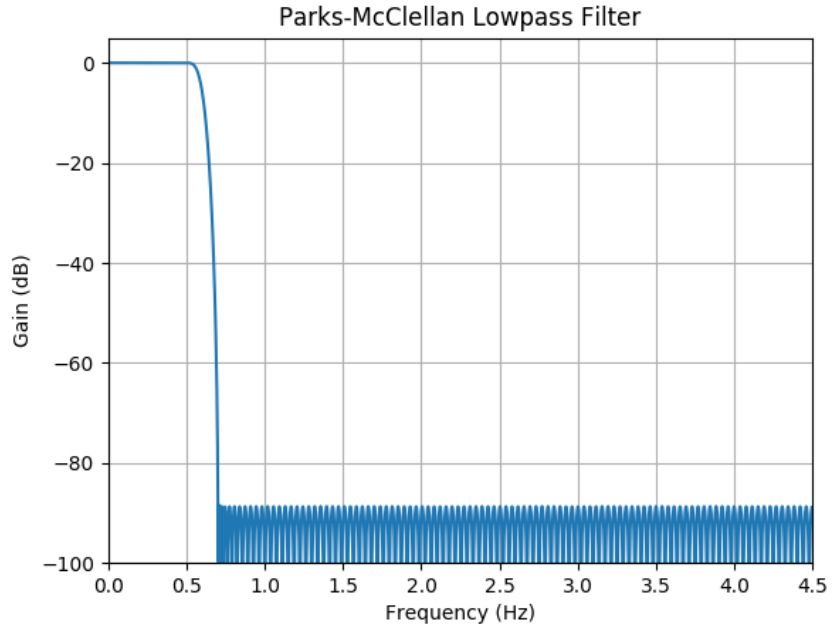

Figure 2.53: Parks-McClellan Lowpass Filter of order 235, cutoff frequency 0.5Hz, transition width of 0.2Hz and sampling frequency of 9Hz

As shown in section 3.4, FLIR SC305 has a maximum frame rate of 9Hz. In order to design the series of polyphase bandpass filters, a Parks-McClellan low pass filter was used. For the filter design, the following parameters were used;

- Order of the filter was *235*. This was done to achieve low passband ripple and side lobe attenuation better than most of the windowing methods (atleast 80dB attenuation).
- Cutoff frequency = *(Sampling Frequency)/ (4.5 * No. of Bands)*
- Transition width of frequency response from passband to stopband

2.8.5. Cubic Spline Interpolation

Interpolation is an analysis method of fitting a curve that can satisfy the conditions for a set of known points and using that curve in constructing new data points between the range of the known data points. The curve can range from being a linear equation between two points or a more complex polynomial like a cubic equation[48, 49]. In fig.2.54, there are a random set of data points defined and the output of each of the interpolation methods is also displayed along with the points showing what the constructed set of data points are depending on the type of interpolation being used.

Let's define a set of data points in the form $(x_0, y_0), (x_1, y_1), (x_2, y_2), (x_3, y_3), ...(x_n, y_n)$,; where x_i is the x-coordinate and y_i is the y-coordinate for $0 \leq i \leq n$, satisfying the conditions that all points are ordered in ascending order of x_i and no two points have the same x_i i.e. $x_0 < x_1 < x_2 < ..... < x_n$. For the $n+1$ points provided, there will be n curves $C_i(x)$ that can be expressed as;

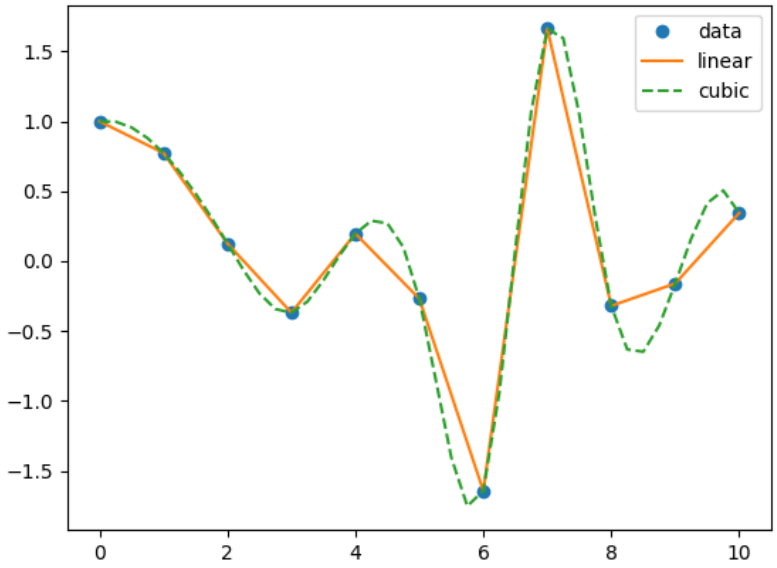

Figure 2.54: Linear and Cubic Interpolation over a set of random set of points

$$S(x) = \begin{cases} C_1(x),\ where & x_0 \le x < x_1 \\ C_2(x),\ where & x_1 \le x < x_2 \\ ..... & \\ C_i(x),\ where & x_{i-1} \le x < x_i \\ ..... & \\ ..... & \\ C_n(x),\ where & x_{n-1} \le x < x_n \end{cases} \tag{2.50}$$

where *S(x)* is the set of curves $C_i(x)$ used after interpolation to show the nature of the constructed data points and to create new ones. For a random coordinate x_j which satisfies the condition $x_0 < x_{i-1} < x_j < x_i < x_n$, then $y_j = C_i(x_j)$ and (x_j, y_j) becomes the new data point.

In case of linear interpolation, $C_i(x)$ will be a linear equation of the form $y = ax + b$; a being the slope of the line and b being the offset, that satisfies the condition for its respective points (x_{i-1}, y_{i-1}) and (x_i, y_i). As seen in fig.2.54, the linear interpolation is not smooth and can be very abrupt. However, using a cubic spline instead of a linear equation will provide a smoother and continuous curve with no abrupt changes at the data points.

For cubic spline interpolation, the curves between the data points are of the form $C_i(x) = a_i x^3 + b_i x^2 + c_i x + d_i$; where $a_i \neq 0$. In order to determine the set of cubic splines S(x) that is valid for the provided set of points and also provides a smooth and continuous curve, the following conditions need to be satisfied[48, 49];

- $C_i(x_{i-1}) = y_{i-1}$ and $C_i(x_i) = y_i$ for $1 \le i \le n$
- $C_i^{'}(x_i) = C_{i+1}^{'}(x_i)$ for $1 \le i \le n$
- $C_i^{''}(x_i) = C_{i+1}^{''}(x_i)$ for $1 \le i \le n$

As $C_i(x)$ is a cubic equation, its double derivative $C_i^{''}(x)$ will be a linear equation expressed as $C_i^{''}(x) = 6a_i x + 2b_i$. This linear equation can be fitted between the points $M_{i-1} = C_i^{''}(x_{i-1})$ and $M_i = C_i^{''}(x_i)$ and can be

expressed as;

$$\begin{aligned} C_i''(x) &= M_{i-1}\frac{x_i - x}{h_i} + M_i\frac{x - x_{i-1}}{h_i}; \\ &where;\, x\epsilon[x_{i-1}, x_i]\, and\, h_i = x_i - x_{i-1} \end{aligned} \tag{2.51}$$

After integrating the equation twice to get $C_i(x)$, the equation results in;

$$\begin{aligned} C_i(x) &= \int\left(\int C_i''(x)dx\right)dx \\ &= M_{i-1}\frac{(x_i - x)^3}{6h_i} + M_i\frac{(x - x_{i-1})^3}{6h_i} \\ &+ \left(y_{i-1} - \frac{M_{i-1}h_i^2}{6}\right)\frac{x_i - x}{6h_i} + \left(y_i - \frac{M_i h_i^2}{6}\right)\frac{x - x_{i-1}}{6h_i} \\ &where;\, x\epsilon[x_{i-1}, x_i] \end{aligned} \tag{2.52}$$

As the condition $C_i'(x_i) = C_{i+1}'(x_i)$ is still valid and using the equation 2.52,

$$C_{i+1}'(x) = -M_i\frac{(x_{i+1} - x)^2}{2h_{i+1}} + M_{i+1}\frac{(x - x_i)^2}{2h_{i+1}} + \frac{y_{i+1} - y_i}{h_{i+1}} - \frac{M_{i+1} - M_i}{6}h_{i+1} \tag{2.53}$$

$$\begin{aligned} C_{i+1}'(x_i) &= -M_i\frac{h_{i+1}}{2} + \frac{y_{i+1} - y_i}{h_{i+1}} - \frac{M_{i+1} - M_i}{6}h_i \\ C_i'(x_i) &= M_i\frac{h_i}{2} + \frac{y_i - y_{i-1}}{h_i} - \frac{M_i - M_{i-1}}{6}h_i \end{aligned} \tag{2.54}$$

which can be further simplified to[48, 49];

$$\begin{aligned} \mu_i M_{i-1} + 2M_i + \lambda_i M_{i+1} &= D_i \\ &where; \\ \mu_i &= \frac{h_i}{h_i + h_{i+1}} \\ \lambda_i &= 1 - \mu_i \\ D_i &= 6f[x_{i-1}, x_i, x_{i+1}] \end{aligned} \tag{2.55}$$

$f[x_{i-1}, x_i, x_{i+1}]$ is a divided difference function. There are two boundary conditions that need to be taken into consideration before proceeding[48, 49];

1. Assuming that the first derivatives at both ends are known; i.e. $C_1'(x_0) = f_0'$ and $C_n'(x_n) = f_n'$. Using equation 2.53, we can get;

$$\begin{aligned} C_1'(x_0) &= -M_0\frac{(x_1 - x_0)^2}{2h_1} + M_1\frac{(x_0 - x_0)^2}{2h_1} + \frac{y_1 - y_0}{h_1} - \frac{M_1 - M_0}{6}h_1 \\ C_n'(x_n) &= -M_{n-1}\frac{(x_n - x_n)^2}{2h_n} + M_n\frac{(x_n - x_{n-1})^2}{2h_n} + \frac{y_n - y_{n-1}}{h_n} - \frac{M_n - M_{n-1}}{6}h_n \end{aligned} \tag{2.56}$$

   which can be further simplified to ;

$$\begin{aligned} 2M_0 + M_1 &= 6f[x_0, x_0, x_1] \\ 2M_n + M_{n-1} &= 6f[x_{n-1}, x_n, x_n] \end{aligned} \tag{2.57}$$

Therefore, assuming the condition that $\lambda_0 = \mu_n = 1$, $D_0 = 6f[x_0, x_0, x_1]$ and $D_n = 6f[x_{n-1}, x_n, x_n]$ and using equation 2.55, we get the equation;

$$\begin{bmatrix} 2 & \lambda_0 & & & & & & \\ \mu_1 & 2 & \lambda_1 & & & & & \\ & \cdot & \cdot & \cdot & \cdot & \cdot & \cdot & \\ & \cdot & \cdot & \cdot & \cdot & \cdot & \cdot & \\ & \cdot & \cdot & \cdot & \cdot & \cdot & \cdot & \\ & & & & \mu_{n-1} & 2 & \lambda_{n-1} & \\ & & & & & \mu_n & 2 & \end{bmatrix} \begin{bmatrix} M_0 \\ M_1 \\ \cdot \\ \cdot \\ \cdot \\ M_{n-1} \\ M_n \end{bmatrix} = \begin{bmatrix} D_0 \\ D_1 \\ \cdot \\ \cdot \\ \cdot \\ D_{n-1} \\ D_n \end{bmatrix} \tag{2.58}$$

2. Assuming that the second derivatives at both ends are known; i.e. $C_1''(x_0) = M_0 = f_0''$ and $C_n''(x_n) = M_n = f_n''$. If $f_0'' = f_n'' = 0$, then it is called a *natural boundary condition.* Therefore, assuming the condition that $\lambda_0 = \mu_n = 0$, $D_0 = 2f_0''$ and $D_n = 2f_n''$ and using equation 2.55, we get the same equation as 2.58.

After solving these equations and receiving the values for $M_0, M_1, ..., M_n$, and substituting these values in equation 2.52, we get the the $C_i(x)$ between the points and in turn get $S(x)$ providing the curve fitting the provided set of data points.

Cubic Spline interpolation is used to compensate for the irregularity between the sensor readings because in real-time situations there will be inconsistent duration between consecutive samples. In order to use any spectral analysis method the data points need to be equally spaced in the time domain and cubic spline interpolation provides us with a more smoother approximation between the values; as shown in fig.2.54.

3

Tools and Software

3.1. Pine ROCKPro64

The whole setup and algorithms will be implemented upon a Pine ROCKPro64, which will also be connected to the sensors, cameras and a server. The ROCKPro64 is the most powerful single board computer from PINE64, featuring a Rockchip RK3399 hexa-core SOC as well as a quad-core Mali-T860MP4 and up-to 4GB of dual-channel LPDDR4 system memory.

3.2. Balance KH 8095 Blood Pressure Monitor

The *Balance KH 8095* is a *digital sphygmomanometer* (DSPHG) that will be used to measure the heart rate of the subject. This device follows an auscultatory method of measuring blood pressure[53]. An occluding cuff is attached to the arm along with a microphone or a listening device to hear the blood flow from the blood vessels in the arm; called as Korotkov sounds. The cuff inflates and stops the blood flow by applying pressure on the blood vessels above the systolic pressure. When that happens, then the microphone doesnot hear any sounds. Then the cuff starts releasing pressure slowly. When the microphone starts hearing sounds from the arterial blood flow in the arm, then point when that happens is the systolic pressure and the device records it and continues deflating. When the microphone stops hearing any sounds again, this means that the pressure is lower the diastolic pressure and records that value. Between the duration of identifying the systolic and diastolic pressure, the microphone is continuously hearing the arterial blood flow and also keeps track of the number of heart beats that happen during the measurement. Once it identifies both systolic and diastolic pressure, it calculates the average heart rate for the duration. The *Balance KH 8095* spends around 14-16 sec for inflating the cuff and another 15 sec for measuring the systolic/diastolic pressure and heart rate; implying that it averages the heart rate over a 15 sec duration and takes 30 sec to measure it.

3.3. Philips SureSigns VM6

The *Philips* **SureSigns VM6** is the ECG provided by TU Delft's Bioelectronics group. The VM6 is a 3 and 5 lead ECG that is capable of measuring heart rate, breath rate along with arrhythmia analysis, body temperature and SPO_2. For our experiments, we will be using only 3 leads that will be placed on the chest of the subject being monitored; as shown in fig.3.1, where the red electrode will be placed in the right arm(RA), the yellow electrode in left arm(LA) and the green electrode in the left leg(LL) or on the lower stomach; also referred as the Einthoven's triangle. The device has a USB port where an external storage device can be connected and the output of monitoring the subject is stored in a file named "TrendLijst_ID onbekend.xls", along with the timestamp of when the values were recorded. The values recorded will be the average of every 15 seconds of the recordings. Therefore, the timestamp of the device needs to be synchronized with the epoch timestamp in seconds before proceeding with the recordings in order to be compared with other sensor readings.

Biopotentials are generated throughout the body because of difference in ionic concentration of electrolytes

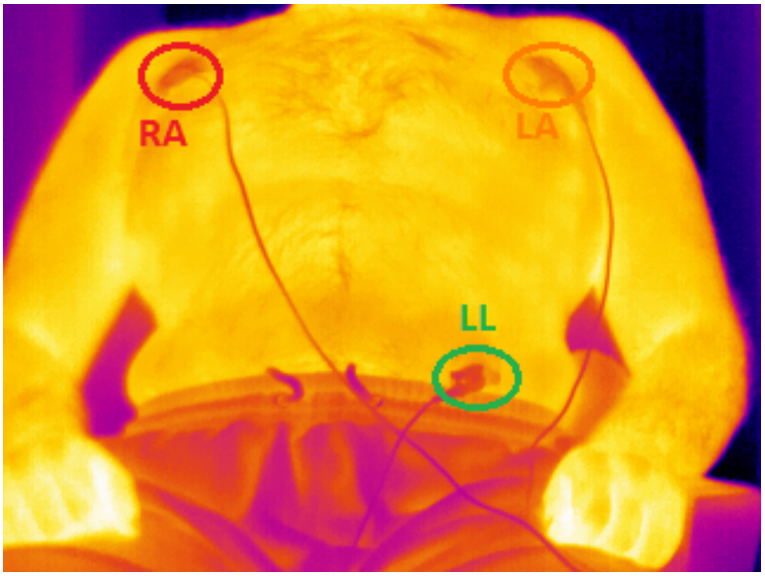

Figure 3.1: Placement of ECG electrodes on the chest in thermal images

(mainly Na+, K+, Cl- ions) across the cellular membrane of different cells, including the heart. The electrodes placed on the body read record the electrical activity of the heart by measuring these biopotentials and gives information about the cardiac activity[53]. As shown in fig.3.2, the electric activity of different parts of the heart contribute to the standard PQRST wave that is displayed by the ECG device.

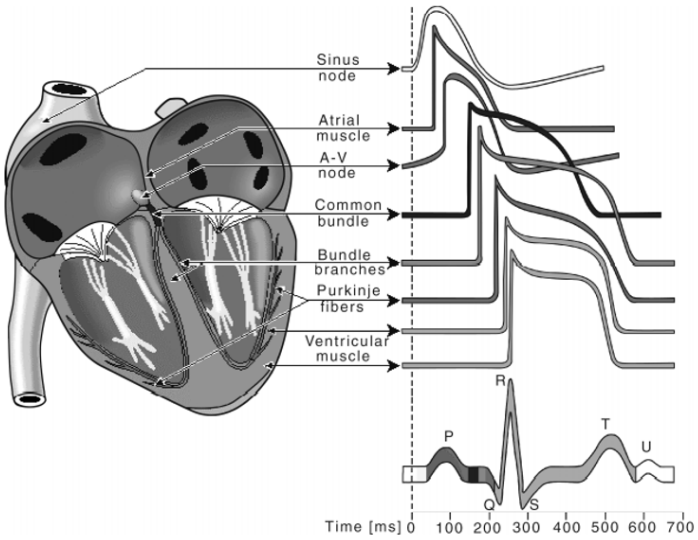

Figure 3.2: Electric activity of each part of the heart to make the PQRST wave[53]

The breath rate is measured by measuring the change in the trans-thoracic impedance between the RA and LL electrodes. This allows the device to monitor breathing activity even in cases like irregular or abdominal breathing and also for sleep apneas. The respiratory signal shows when the chest expands in case of inhaling; in which case the graph goes up, and contraction while exhaling; in which case the graph goes down. However, there is a drawback to this method of monitoring respiratory rate. Sometimes the values recorded are invalid because they are affected by the chest movement. As the impedance between electrodes is used to measure the breathing activity, any action like moving your chest or strain on your chest muscles which could affect the electrical activity will also be reflected on the ECG monitor. This will cause irregular readings and in turn gives wrong values for breath rate. Fortunately, this doesnot affect the recording of the cardiac activity unless the electrodes are disturbed or are not connected properly.

3.4. FLIR Infrared Camera and ResearchIR Software

The camera used is FLIR SC305 infrared camera. It has 9Hz frame rate and resolution of 320x240 pixels and is a LWIR camera(7μm-14μm).

3.4.1. Installation Procedure

First, download ResearchIR Max software from the flir website:

- Go to https://flir.custhelp.com/app/account/fl_download_software
- Create a new account (needed to download software)
- Select the product: Reporting and Analysis Software
- Select below that: FLIR ResearchIR
- Download the software

Then, follow the procedure to install the ResearchIR Max from the executable. After that, an activation code has to be inputted to activate the software.

3.5. PT100 Temperature Sensor and HP-3478A Multimeter Interface

In order to perform the thermal analysis of the incubator, a PT-100 temperature sensor was connected to a HP-3478A multimeter and the 4-wire resistance of the sensor was measured to determine the temperature. The formula for the temperature conversion given in equation 3.1 comes from the PT-100 manual.

$$temperature = 3383.81 - 0.287154 * \sqrt{159861899 - 210000 * 4WireResistance} \tag{3.1}$$

This gave the flexibility to measure and analyze each region specifically. However, the multimeter had a GPIB interface which could be used to interface and read values on the system. For this, the GPIB device drives and pyvisa python library needed to be installed on the system to be interfaced with the multimeter. The workings of the interface can be seen in fig3.3

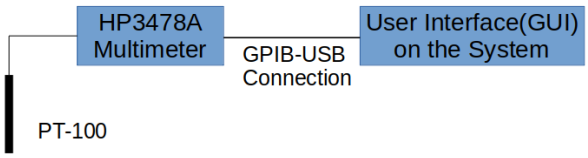

Figure 3.3: Working of the Multimeter Interface

A GUI was designed not only to read from the multimeter but also to record and graphically plot the acquired values.

The process comprises of controlling and reading from the multimeter, converting readings to temperature, filtering the temperature values, recording them and/or storing. The GUI searches for the available GPIB devices and displays the list but it will automatically connect to the first available device. All features of the multimeter are accessible through this interface, including changing precision, range or mode of the multimeter. The interface also implements displaying the values read from the multimeter in real-time. As mentioned earlier, the 4-Wire Resistance read from the multimeter can be converted into temperature. So the interface converts the acquired values into temperature and also applies moving average and kalman filter. These values are also displayed in a real-time graph. The frequency at which the values are read and displayed from the multimeter and the filter coefficients can be adjusted as per the user. The real-time display, conversion, filtering and/or recording of values happens when the "Run" button is pushed i.e. the process is running. The button needs to be pushed again to stop the process.

3.5.1. Software Used

- GPIB Device Drivers
- PY-Visa Python library
- PYQT5 Designer
- Other associated Python Libraries like Numpy, Math, Pyqtgraph, CSV, etc

3.6. TMP116 Interfaced with STM32L476G-DISCO

The TMP116 is a low-power and high-precision temperature sensor with integrated EEPROM memory. It provides a 16-bit temperature result with a resolution of 0.0078°C and an accuracy of up to ±0.2°C with no calibration. The STM32L476 Discovery kit (32L476G-DISCO) is a 32-bit microcontroller that is energy efficient with ultra-low-power capability and supported I2C communication. The TMP116 is also I2C compatible. So two of these sensors were attached on a PCB 10cm apart and both were given different addresses and interfaced by STM32L476G-DISCO over the I2C communication protocol. Temperature is read from both TMP116 sensors simultaneously.

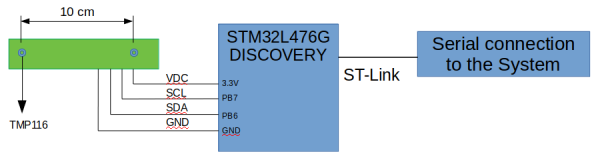

Figure 3.4: Working of the STM32L476G board with TMP116

In order to enable communication and read from the temperature sensors, a binary file was uploaded to STM32L476 via the ST-Link/USB connection to the system. The binary file was created using the Mbed Compiler by specifying the board and implementing the I2C example already provided by the compiler. After the binary file is created, connect the connections are made between the temperature sensor PCB and the STM32L476 board, with pins PB7 as SCL and PB6 as SDA. Then the microcontroller board was connected using the ST-Link/USB connection and the binary file was uploaded i.e. dragged and dropped to the device.

The binary was written in such a way that whenever the microcontroller setup was connected to the system, it would read from the temperature sensors and send data to the system via serial communication. To be able to read from the device via serial port, the ST-Link and OpenOCD drives needed to be installed to the system. Then a python program was written to read from the serial port of the system where the board was connected and record the values in a csv file for future reference.

3.6.1. Software Used

- M-bed Compiler
- ST-Link and OpenOCD drivers
- Other associated Python Libraries like CSV, Serial, etc

3.7. Edison Board

The Intel Edison compute module is a compact computing platform that's small by design but has great computing power and is easily interfaced with the system and other associated blocks. The 9-Degrees-of-Freedom(9DoF) block is a Intel Edison compatible module with many sensors like gyroscopes, accelerometers, a magnetometer and a temperature sensor on it. So the Intel Edison board was connected to the 9DoF block and the whole block was connected to the system using a microA USB connection. PuTTY was used to interface the block with the system over the serial connection over the serial line "/dev/ttyUSB0" with speed of 115200 MBps. We needed to read from the temperature sensor on the 9DoF block. So a C++ program was written to read and record the temperature sensor values and record them in a csv file for future analysis.

3.12. Dense Optical Flow Analysis of Infrared Camera Recording

The Gunnar Farneback Optical Flow was used to perform the analysis for Thermal Lensing and Heatflow of the portholes of the incubator. The ResearchIR software was used to read from the FLIR-SC305 IR camera and record the camera's output in a video(WMV) format.

The recording was done with a fixed temperature scale i.e. the colour of the recording will not auto adjust to the temperature scale. As the optical flow algorithm relies on the intensity of the pixels remaining the same, the fixed scale version would provide better results.

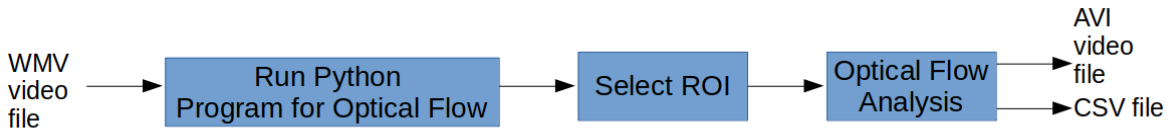

Figure 3.8: Optical Flow analysis of IR camera recordings

The Gunnar Farneback algorithm was implemented on the recordings using the OpenCV libraries in python, with functionality shown in 3.8. The following parameters were used for the Gunnar Farneback optical flow implementation;

- image scale: 0.5
- number of pyramid layers: 10
- averaging windows size: 20
- number of iterations for each pyramid level: 10
- size of the pixel neighborhood used to find the polynomial expansion: 10
- standard deviation: 5.0

These values were decided on a trial and error basis after observing which set of output was giving less noise; while trying not to dampen any possible patterns with low intensity. The python OpenCV program would take the input of the video file from ResearchIR and open it. It would display the first frame of the recording so that we can select the ROI we are interested in analyzing. The programs sets the points of interest on the ROI to record the output from, which in this case would be 3 concentric circles with 8 equidistant points on each circle i.e. 24 points in total. Then it would perform dense optical flow analysis on the specified region for the whole region and store the output of the analysis as a video(AVI) file (shown in figure 3.9) and a CSV file, recording the magnitude and direction of flow in each of the 24 points of interest.

3.12.1. Software Used

- ResearchIR
- OpenCV libraries for Python
- Other associated Python libraries like Numpy, CSV, Math etc.

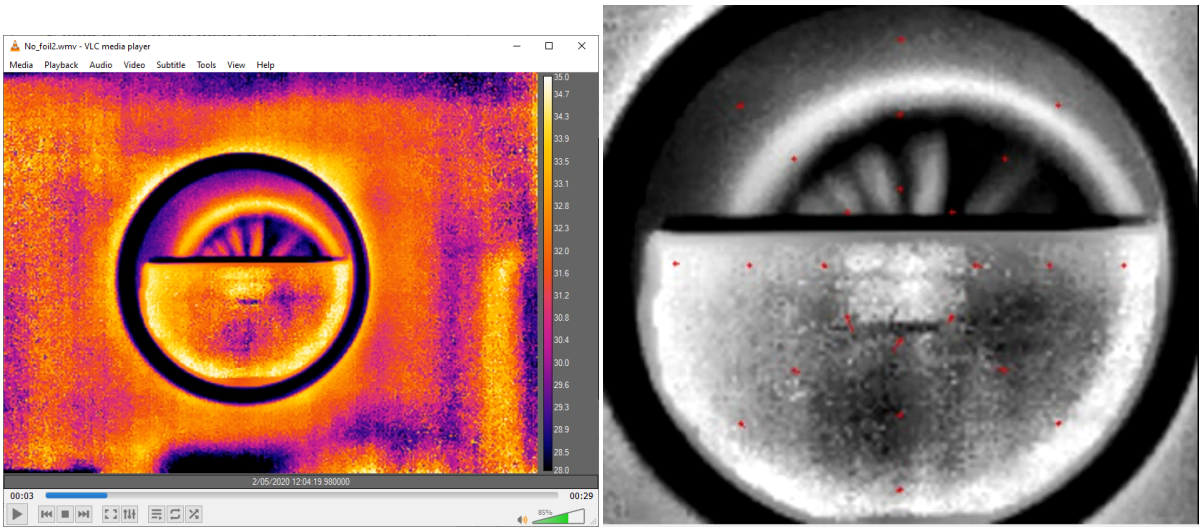

Figure 3.9: Left: snapshot of infrared video of aluminum block inside incubator and right: visualization of optical flow of the video

5

Pre-processing Filter Chain

The pre-processing of the algorithm will acquire the images data from the camera and process it until it can be used as suitable input to the vitals monitoring algorithm, as shown in figure 5.1. This filter chain was designed in collaboration with Erik Wirianto of TU Delft.

Figure 5.1: Filter chain for pre-processing of thermal images

The steps in the pre-processing are:

- Establishing communication between the IR camera and the system and enable data storage in the server.
- Set the camera the field of view (FOV) to the neonate placed inside the incubator.
- Adjust the focus and frames per second (FPS) of the camera.
- Acquire the raw data from the camera iteratively. The raw data is a 320x240 matrix with each element being a 16-bit unsigned integer. So the total size of each frame would be around 153.7 KBytes(size of matrix x 2Bytes for each element).
- Using heat map transformation to translate the raw data into displayable image.
- Normalize raw data value so it can be processed easier.
- Select and track global and local region of interest (ROI).

- Calculate the temperature from the raw data of the ROI.
- Combine image data and sensor data from the incubator and synchronize the timestamp.
- Compensate thermal error from of the temperature calculation based on the incubator data.
- Send the results to the server.

5.1. Data Normalization

Raw data received from the camera is 16-bit integer, ranging from 0 to 65.535 integer value. However, in normal condition where the temperature of objects inside the frame is around 20-40 °C, the raw data values are around 18.000 - 21.000 integer. Then, we can normalize the value into float value (between 0 to 1) with the maximum and minimum value from the whole frame. It will be easier to processed.

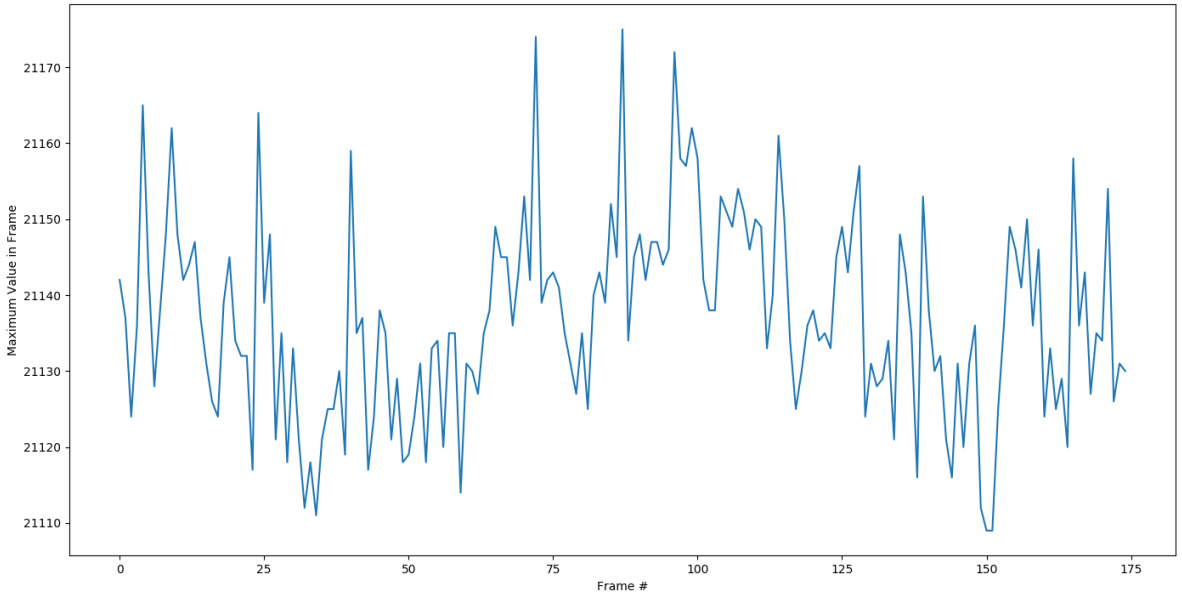

Figure 5.2: Raw data maximum value from 20 seconds video of unmoving person

However, since we know there is noise coming from the camera, the maximum and minimum value will go up and down with the noise, causing unstable normalized value. Moreover, from several observation, there is no recognizable pattern in the noise. To solve this, the normalization has to be done once rather than per frame. The average maximum and minimum value from several frames (e.g. 9 frames or 1 second) can be used as a maximum and minimum threshold for the normalization for the measurement. It will make the pixel normalized value more stable and help with the tracking process.

5.2. Global and Local ROI Tracking

6

Respiratory and Heart Rate Monitoring Algorithm

After the pre-processing part of the algorithm provides with the ROI's temperature after tracking and noise compensation, it will use this information to extract the information about the heart rate and the breath rate of the subject in the FOV.

6.1. Respiration Rate Measurement using Thermal Imaging

Among the non-contact method of measuring respiratory rate in thermal imaging, the most commonly used methods involve either monitoring the chest movement[52] or measuring the temperature activity of the nasal cavity region using an IR camera[3, 20, 64, 65]. As we exhale, the temperature of the nostrils goes up while the temperature is lower during inhalation. The heat flow rate of each respiration cycle; as shown in [2], is written as

$$\dot{Q}_{RR}(t) = \dot{Q}_{rad}(t) + \dot{Q}_{conv}(t) + \dot{Q}_{evap}(t) + \dot{Q}_{perf}(t) + \dot{Q}_{latent}(t) \tag{6.1}$$

where;

- $\dot{Q}_{rad}(t)$ = rate of heat dissipation between the air flow and the nasal surface
- $\dot{Q}_{conv}(t)$ = rate of heat dissipation between the nasal inner lining and air flow
- $\dot{Q}_{evap}(t)$ = rate of heat dissipation because of evaporation at the nasal surface
- $\dot{Q}_{perf}(t)$ = rate of heat dissipation because of blood perfusion
- $\dot{Q}_{latent}(t)$ = rate of heat dissipated because of latent heat loss through air flow

After monitoring the thermal activity of the nose and keeping a record of the change in average temperature over the duration, the frequency analysis of the signal is performed. The frequency component with the maximum power in the relevant frequency range would be the breath rate. The breath rate of a neonate lies in the range of 40-60 breaths/min[1, 30] or 0.667-1.000Hz. The adults breath rate lies around 10-40 breaths/min[20] or 0.167-0.667Hz but in stable conditions they lie around 12-24 breaths/min[30, 68] or 0.200-0.400Hz. Identifying which frequency component has the maximum power in these ranges provides us with the calculated breath rate. This methods also allows to monitor for conditions like breathing arrhythmia or sleep apnea. However, there are a few disadvantages of using this method on neonates in incubators;

1. Neonates have low lung volume, so they may not exhale enough heat or air to be detected by the IR camera
2. The nasal aperture is very small, about $0.08cm^2$[2] which may be hard to locate and track

3. The neonate might have a ventilator mask attached around the face or the nose. This will make reading from the nostrils a very difficult task. This also applies in case of adults. In these cases, monitoring chest movement will be able to provide better results[52].

4. The neonates might keep moving their faces around, i.e. not keeping it steady or in the same position. This makes it difficult to track the position of the nostrils and read from them. Face detection or different tracking methods are used to track the nostrils and make the algorithm motion robust[3, 20, 64, 65].

In [30], a different approach on monitoring respiration rate in neonates and adults is proposed. Instead of looking for specific ROI like nostrils or chest region, this algorithm proposes a black-box approach and considers the whole frame as its ROI and divides it into many equal sections; as shown in 6.1. The respiratory signal was extracted for each ROI and then analyzed with regard to its quality. Finally, suitable ROIs were automatically selected and information was fused in order to get robust estimations for respiration rate. By using a signal quality index and some sensor fusion techniques, the algorithm selects the ROI's responsible for good quality signals.

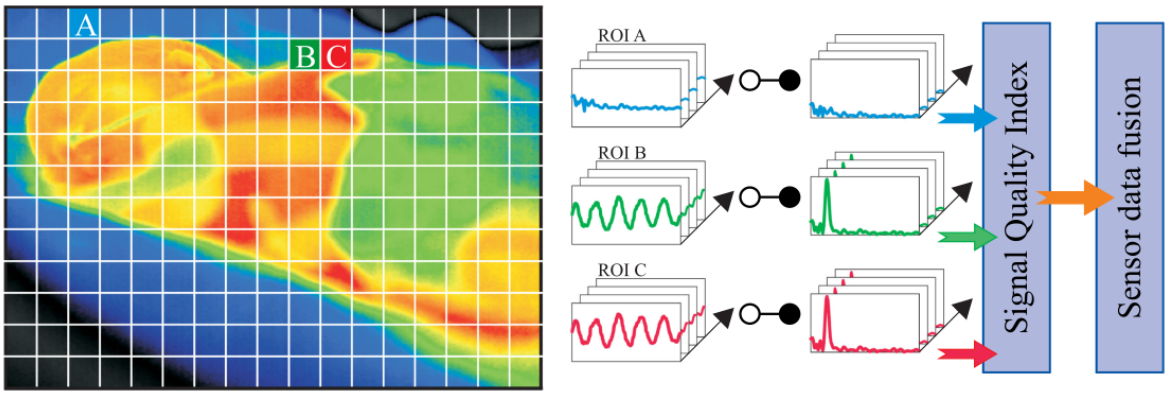

Figure 6.1: Respiration monitoring over the whole frame as mentioned in [30]

For this algorithm, there are three filter bands;

- Low-Pass (LP): f < 0.1Hz,
- Band-Pass (BP): 0.1Hz ≤ f ≤ 3 Hz,
- High-Pass (HP): f > 3 Hz.

In order to determine the quality of the signal from the ROI, a signal quality index (SQI) in equation6.2 was empirically developed for this algorithm, as mentioned in [30];

$$SQI = \begin{cases} 1 - \left[\frac{1}{2} * F_3 + \frac{1}{4} * (F_1 + F_2)\right], if\ F_4 \geq 2 \\ 1 - \frac{1}{2} * (F_1 + F_2), otherwise \end{cases} \tag{6.2}$$

where F1-F4 are taken from the normalized spectrum after frequency transformation of the signal;

- F1 is to the maximum within the HP-band.
- F2 is the percentage of values in the HP-band larger than a specified threshold
- F3 is the difference between maximum in the BP-band and maximum in the LP-band
- F4 is the ratio between the maximum in LP-band and maximum in BP-band

Then the output provided by SQI will be fed to three different sensor fusion methods;

- **Median:** Calculate median frequency for all ROIs
- **Best SQI:** Take ROI with the maximum SQI
- **Bayesian Fusion:** Using Bayes Law to get a posterior probability estimation

Algorithm	Frame Rate(Hz/fps)	Frame Resolution	Sampling Duration(sec)
Frequency analysis of all ROIs in a frame [30]	30	1024x768	15
Thermal activity of the nose [66]	30/60/115	640x512	34
Thermal activity of the nose and mouth region [67]	10	640x480	30

Table 6.1: System specifications of Respiration Monitoring Methods using LWIR

The method in [30] is a probabilistic approach that provides respiration rate without tracking any anatomical landmarks, making it a very robust algorithm with RMSE of 4.15 ± 1.44 bpm. However, the number of computations it performs per frame; considering all ROI's along with their frequency domain behaviours and sensor fusion of their results, makes it a very computationally intensive algorithm. Also, [30] did not explore on the possibility of which ROIs were responsible for providing valid results. This possibility can be further explored in the experiments for this project.

In table.6.1, the system parameters used by most of the systems for monitoring breath rate are provided to demonstrate the range of system requirements that have been used for respiration monitoring in LWIR. Most of the algorithms; including the ones in table.6.1, have a sampling rate higher than 30 fps with one exception and frame resolution higher than 640x480. Given that the FLIR SC305 camera has a maximum frame rate of 9Hz and frame resolution of 320x240, our experiments concerning breath rate measurements will be centred around the following objectives;

- Reducing frame rate, frame resolution or sampling duration for measuring breath rate.
- Exploring the possibility of breath rate measurement from ROIs other than the nose.

6.2. Heart Rate Measurement using Thermal Imaging

Among the methods for measuring heart rate through IR camera, using thermal analysis on the regions with the superficial blood vessels under the skin is one of the most commonly used methods for all IR ranges. As seen in fig.6.2, the major blood vessel complex on the upper body are clearly visible from an IR camera. The images in fig.6.2 are take from a MWIR camera[15]. The same method can also be used for acquiring heart rate from a LWIR camera [21, 66, 68], .

Figure 6.2: Thermal imaging of the carotid, superficial and radial vessel complex respectively [15]

Instead of isolating the blood vessels; as shown in fig.6.2, methods involving remote photoplethysmography(rPPG) isolate relevant ROIs like the forehead, cheek, neck etc and track these instead[69, 70]. Face detection and tracking also helps the algorithm to be motion robust and this can be done in all ranges of IR recordings.

After isolating these relevant regions, the average temperatures of these ROIs are recorded. In order to acquire the heart rate, frequency analysis of the signal is performed and the frequency component with the maximum power in the relevant frequency range is to be identified. The heart rate of a neonate lies in the range of 120-180 bpm[1] or 2.000-3.000Hz. The adults heart rate lies around 40-100 bpm[15] or 0.667-1.667Hz but in stable situations the resting heart rate of an adult lies around 60-100 bpm[68] or 1.000-1.667Hz. Identifying which frequency component has the maximum power in these ranges provides us with the calculated heart rate.

In table.6.2, the system parameters used by most of the systems for monitoring heart rate are provided to demonstrate the range of system requirements that have been used for heart rate monitoring in LWIR. Al-

Algorithm	Frame Rate(Hz/fps)	Frame Resolution	Sampling Duration(sec)
Frequency analysis of Forehead [69]	27	640x480	10
Temperature analysis of facial blood vessels [66]	30/60/115	640x512	34
Temperature analysis of neck blood vessels [21]	12	320x240	30
Wavelet analysis of Forehead [68]	100	640x512	-

Table 6.2: System specifications of Heart Rate Monitoring Methods using LWIR

most all algorithms for heart rate monitoring use a sampling rate higher than 25Hz and most algorithms use a sampling duration of 30sec. In case of monitoring thermal activity of blood vessels, the accuracy of the measurements range around 85-95% in MWIR[15] but in some methods using LWIR have provided accuracy around 95% and higher[21, 66] with average RMSE of 2.83[66]. Methods that have used rPPG instead of monitoring the blood vessels also have provided accuracy around 95% with average RMSE of 2.83[71]. However most of rPPG methods to extract heart rate have been used for RGB or NIR videos. One method in LWIR used rPPG[69] for the extraction of heart rate by monitoring the forehead but it gave a RMSE of 33.18. Given that all other methods used a sampling duration of 30 sec but the algorithm in [69] used a 10 sec window, it might be because of the lower sampling duration despite having the sampling frequency in the same range as the other algorithms. For our experiments, we will be considering a sampling duration of 15-30 sec; as the FLIR SC305 camera has a maximum frame rate of 9Hz and frame resolution of 320x240, with exploring the following objectives;

- Reducing frame rate, frame resolution or sampling duration for measuring heart rate compared to other algorithms.
- Exploring the possibility of heart rate measurement from ROIs other than the Face or by isolating the blood vessels.

6.3. Experiments and Recording

The recordings were performed in the hall available in the 3mE building of TU Delft. Due to the COVID-19 pandemic it was not possible to take recordings of the neonates in the incubators as any external contact could endanger them. In order to test the algorithm, the recordings of adults were taken instead. There were two sets of measurements performed months apart from each other;

1. Recordings of 1 min duration on 5 test subjects; age ranging from 24-60 years, at 9 Hz/fps. A DSPHG was used to measure the heart rate of the subject during the recordings. Only one measurement of the heart rate was taken by the measurement device for the whole duration of the measurement. The ROIs considered for this measurements are face, neck, leg, arm, chest and back and there were a total of 40 recordings. The environment conditions i.e the atmospheric temperature and the humidity of the room were also measured during the recordings using the BME280 sensor.
2. Recordings of 2 min duration on 6 test subjects; age ranging from 24-60 years, at 9 Hz/fps. The SureSigns VM6 ECG was used to measure the heart rate and the breath rate of the subject during the recordings. The ECG stored the measurements in a *.xls* file every 15 sec; after averaging the values for the previous 15 sec. The ROIs considered for this measurements are face, neck, leg, arm, chest and back and there were a total of 60 recordings. Some of the recordings also contained movements in order to test the motion-robustness of the algorithm. The environment conditions i.e the atmospheric temperature and the humidity of the room were also measured during the recordings using the BME280 sensor.

Each of these experiments were analyzed differently and their results will be discussed in details in the next sections.The humidity and atmospheric temperature are recorded to give it as an input to the temperature calculation in the pre-processing part of the filter chain. Then the pre-processing filter chain provides with the average temperature of the ROI that has been selected along with the epoch timestamp of when the frame was taken. This provides us with a time-list of the data which is provided as an input to the vitals monitoring algorithm; as shown in fig.6.3. The respiration and heart rate monitoring filterchain was designed based on the photoplethysmography(PPG) and the spectral analysis principles that were used for monitoring these

vitals; as shown in table.6.1 and table.6.2.

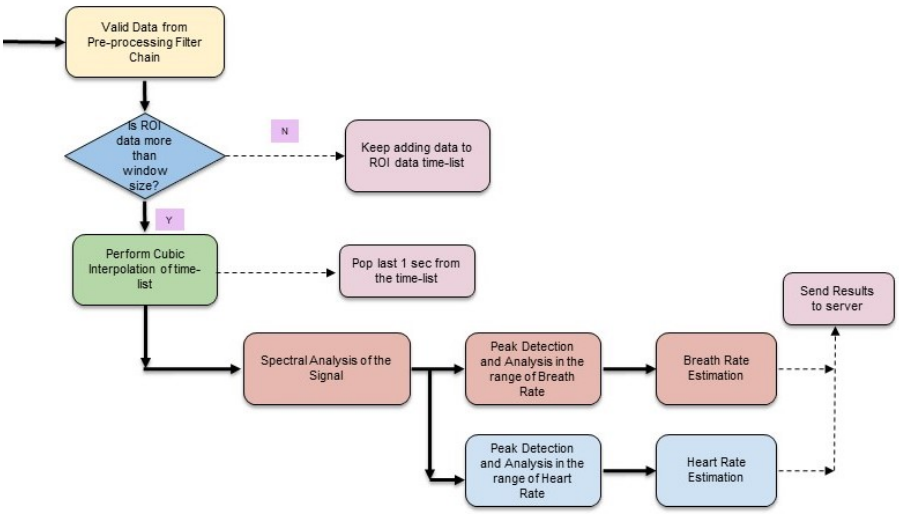

Figure 6.3: Vitals Monitoring Filter Chain

The recordings were given as an input to the front-end shown in fig.3.5 during the simulation so that the ROIs in the recordings can be user selected. After the recordings were given as input to the front-end shown in fig.3.5, the following procedure was followed for testing and generating results;

1. The humidity and atmospheric temperature were given as inputs to the front-end GUI in fig.3.5.
2. The ROI was selected manually for the recording. ROIs that were considered in the recordings are shown in fig. 6.4.
3. The measurements of the ROI begin after it is selected and the time-list of the average temperature of the ROI is created.
4. In the vitals monitoring filter chain; shown in 6.3, if the length of the time-list is greater than the specified sampling duration, then the algorithm proceeds with the next step or else it continues appending to the time-list.
5. Once the time-list is viable for calculation, it proceeds with the cubic spline interpolation to compensate for the inconsistencies in timing between samples.
6. Spectral analysis is performed on the interpolated list to calculate the PSD of the signal i.e determine which frequency components are present in the acquired signal.
7. Peak detection is performed on the PSD to determine the active frequency components present. After they are identified, they are split into the relevant frequency ranges for heart/breath rate calculation.
8. The frequency component with the maximum amplitude in the relevant frequency range for heart/breath rate calculation is identified and these results are sent to the server.

After the simulation is complete, the output of the algorithm; even for different spectral analysis methods, are stored in their respective *csv* files along with their epoch timestamps so that they can be compared in the future.

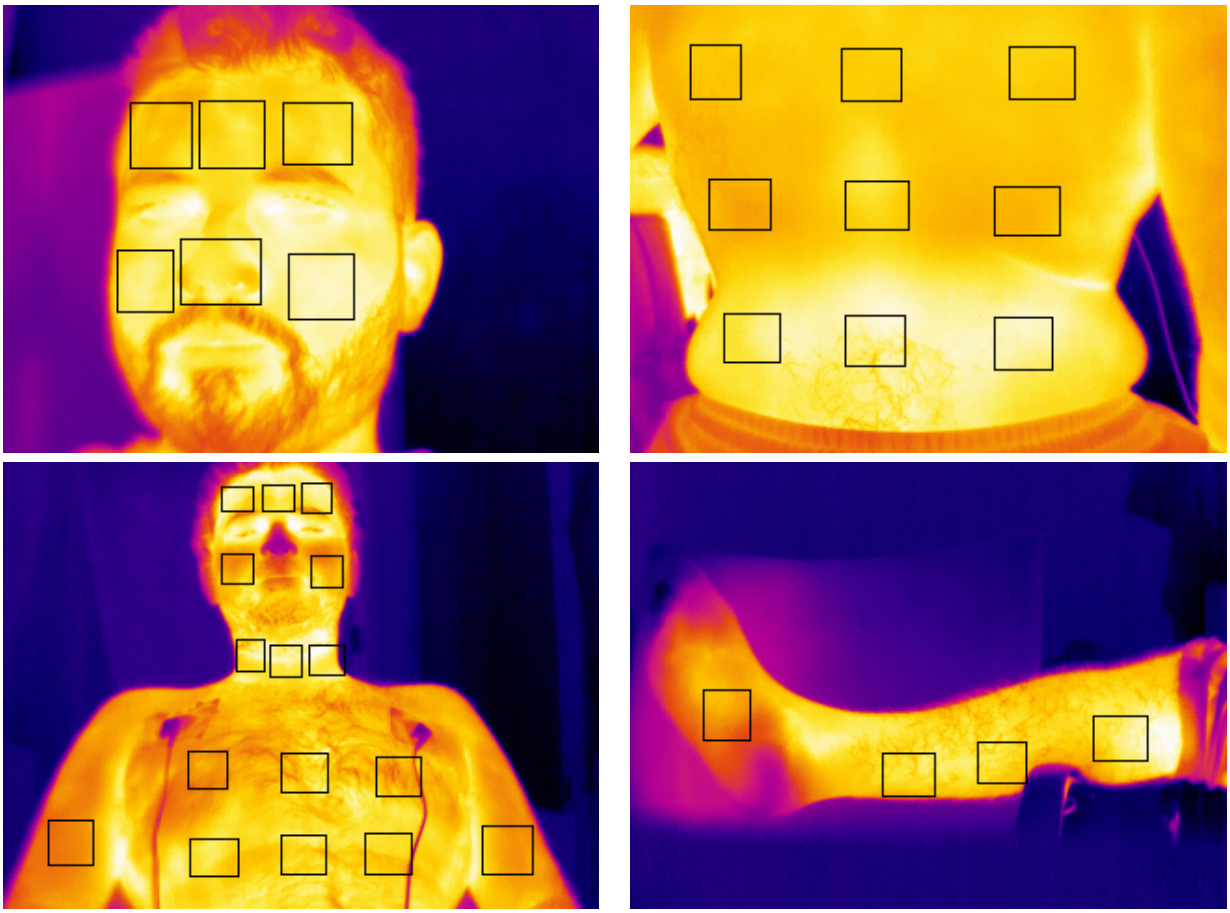

Figure 6.4: Different ROIs selected on the face, chest, back, legs and biceps

7

Analysis of the Experiments with Digital Sphygmomanometer

The first set of recordings were performed using a DSPHG. The subject was told to be still and in upright position and the DSPHG was cuffed to the arm. As the device took 30 sec to provide with an output and the recordings were for 1 min duration, there was only one measurement for the heart rate of the subject during the recordings. Breath rate was not measured for these recordings. The following parameters were considered for the spectral analysis of the signal;

- The minimum length of the time-list needed i.e. the sampling duration for processing was tested from 5-25 sec. As the recordings were done at 9Hz, this gives us 45-225 samples every time the signal is analyzed.
- The spectral analysis methods considered for this experiments were;
    1. Standard Periodogram using Hamming/Hann Window and no zero-padding
    2. Welch Periodogram using Hamming/Hann Window and no zero-padding with each segment length of 80% length of the original signal and sliding of 1 sample
    3. Standard Periodogram using Hamming/Hann Window and no zero-padding after the signal was smoothened using a moving average filter of length 2
    4. Welch Periodogram using Hamming/Hann Window and no zero-padding with each segment length of 80% length of the original signal and sliding of 1 sample after the signal was smoothened using a moving average filter of length 2
    5. Standard Periodogram using Hamming/Hann Window and no zero-padding after the signal was smoothened using a kalman filter
    6. Welch Periodogram using Hamming/Hann Window and no zero-padding with each segment length of 80% length of the original signal and sliding of 1 sample after the signal was smoothened using a kalman filter
    7. Lomb-Scargle Periodogram before/after the cubic spline interpolation was applied to the signal
    8. Lomb-Scargle Periodogram after the cubic spline interpolation was applied to the signal and the signal was smoothened using a moving average filter of length 2 or a kalman filter
- For the heart rate measurement, the range of frequencies that were being monitored were 45-120 bpm or 0.750-2.000Hz.

7.1. Analysis of Different Spectral Analysis Methods

As mentioned earlier, there were 16 spectral analysis methods that were considered. As the DSPHG took 15 sec to calculate the heart rate, for the first analysis we have used a 15 sec window. In the results, there will be two different phases;

- **During Measurement**: This is the duration when the DSPHG is calculating the heart rate during the recording.
- **After Measurement**: This is the instance when the DSPHG is done calculating and provides the heart rate. The values being compared in the results will be from this instance when the values were provided.

The Standard and Welch Periodograms using Hamming/Hann windows provided with the best results. For one of the recordings, the face of the subject is being monitored and the heart rate recorded during the recording was 60 bpm. The output of these methods range from 58.8-60.4 bpm providing us with an error of 0.4-1.2 bpm(see fig.A.1 in appendix).

As seen in fig.7.1 during measurement; the values are significantly higher as compared to when the measurements were taken and then varies a few seconds after they have been measured. This happens because of the method the DSPHG employs for measuring the heart rate. As it blocks the blood vessel and then slowly releases pressure, this can cause stress on the heart and the blood vessels. The device takes 30 sec to measure the heart rate which is a significant duration, this can effect the measurements and show up as a higher or very low heart rate. This results are also visible for other recordings too (see fig.A.2 in appendix). The comparison of Welch Periodograms with Hamming window for 15 sec on different subjects is shown in fig.7.1 including the change in heart rate because of the DSPHG.

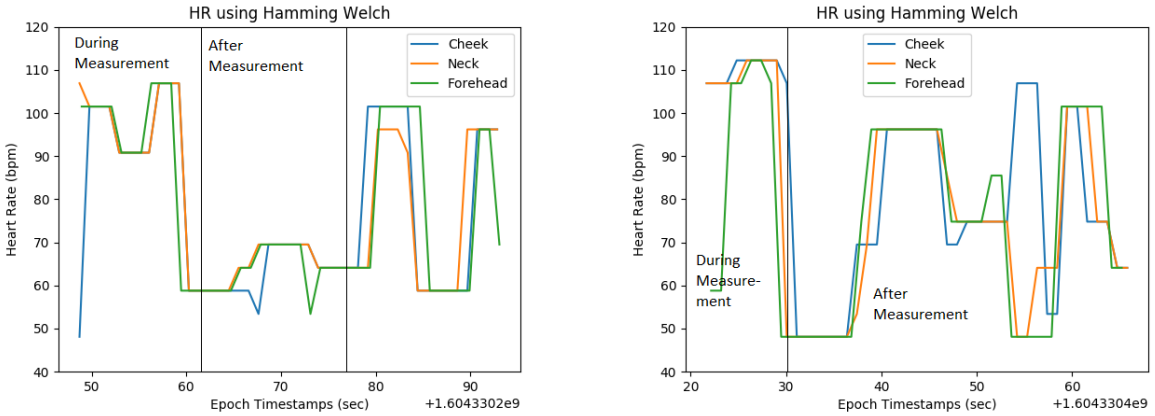

Figure 7.1: Results of monitoring ROIs on the face for different subjects with recorded heart rate of (1) 60 bpm (2) 48bpm.

In case of using the Lomb-Scargle Periodogram, the results show similar behaviour as compared to Standard and Welch Periodogram but is more noisy(see fig.A.3, fig.A.2 and fig.A.1 in the appendix). This behaviour is visible in all cases of using the Lomb-Scargle method.

In fig.7.2, it can be seen that increasing the sampling duration to 25 sec for the Lomb-Scargle method can provide less noisy results. However, as the results in the *after measurement* duration is similar to that of using the Welch method for 15 sec duration; as seen in fig.7.1(1). So, it is preferable to use the Welch method over Lomb-Scargle method.

Using the Welch Periodogram after smoothing the signal using a moving average and kalman filter also does not show significant change in result for most of the test cases(see fig.A.5 in appendix). As Welch Periodogram was already averaging the signal in the frequency domain, averaging it again in the time domain is not necessary. Therefore, the Welch Periodogram was preferred for further analysis of the recordings and also for analysis in the second set of recordings using the ECG.

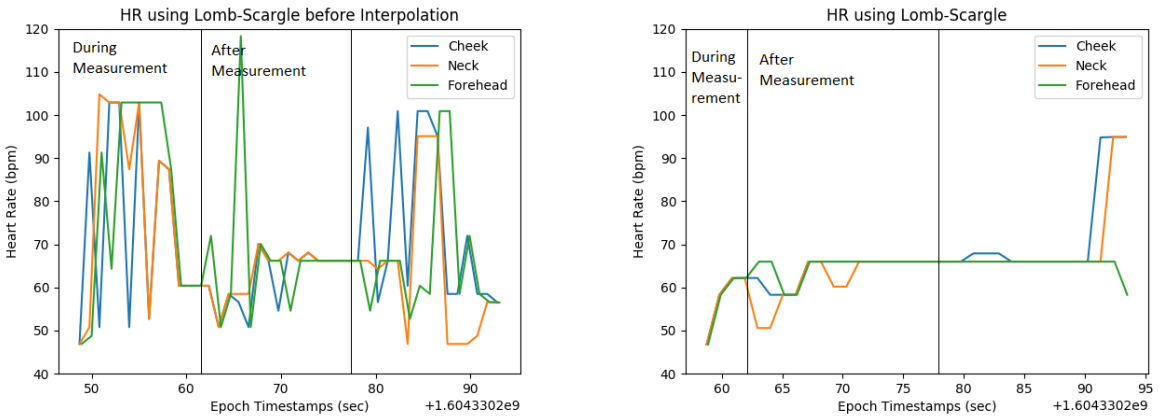

Figure 7.2: Results of monitoring ROIs on the face (same signal as fig.7.1(1)) using Lomb-Scargle Periodogram for (1) 15 sec, (2) 25 sec.

7.2. Analysis of Different Window Size

As mentioned earlier, the window size for the signal was taken from 5-25 sec. This was done to check what would be the minimum duration required to get a viable signal. The window size is also the delay between when the measurements were started and when we start getting the output of the algorithm, implying that the window size needs to be as small as possible. Taking into account the fluctuations in readings caused by the DSPHG, the cases with measured heart rates between 45-90 bpm were considered. The results of using different window lengths can be seen in fig.A.6 in the appendix.

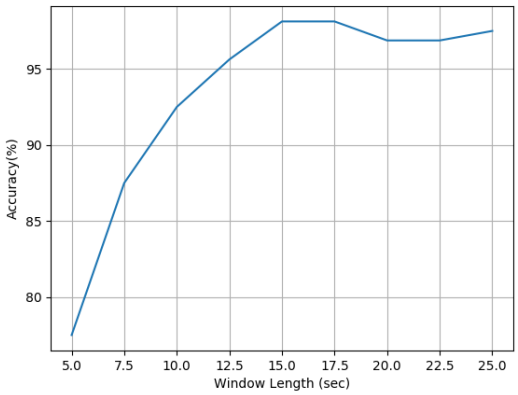

Figure 7.3: Accuracy v.s. Length of time window

Using the 5 sec window provides us with very noisy results. It's not until the window size is around 12.5 sec until we start seeing more stable results and they results appear to be consistent after 15 sec (see fig.A.6 in appendix). Taking into account the values that have been observed in the after measurement duration, there is high error if the window length is 5 sec but it drops as it's increased and it saturates at 15 sec. In fig.7.3, the accuracy of the results are compared with the time window's length showing how the accuracy saturates at 15 sec with close to 97% accuracy. Therefore it is convenient to have at least 15 sec of signal before using it for analyzing the results.

7.3. Analysis of Different ROIs

The ROIs that were monitored are the face, chest, back, legs and hand; as shown in fig.6.4. As mentioned in the earlier sections, the output is calculated using the Welch Periodogram with the Hamming window and a length of 15 sec. Table A.1 in the appendix gives the comparison of the measured and calculated values for

different ROIs. In most of the cases the accuracy of the results are above 90% but in case of using the chest or the back as the ROI the values gave higher error as compared to the face or hands and legs. However, most of the readings from the face give an average error of **1.8 bpm** with an average accuracy of 97%. Even the arm and the leg give a higher accuracy as compared to the chest and the back. As seen in fig.6.2, the superficial blood vessels are more easily visible in the face and the limbs.

So it is possible that the presence of these blood vessels in the region being monitored provided better results than the one where they were not present. So, the face, arms and the legs would be a more suitable ROI for monitoring the heart rate of the subject. This observation will be tested again in the second set of experiments done with the ECG.

8

Analysis of the Experiments with VM6 SureSigns ECG

The second set of recordings were performed using the VM6 SureSigns ECG. The electrodes of the ECG device were connected to the subject as shown in fig.3.1. The duration of each recording was 2 min and the ECG recorded the average of 15 sec of data every 15 sec for both heart and breath rate. Some of the recordings also contained videos with movement in order to test the motion robustness of the algorithm. The following parameters were considered for the spectral analysis of the signal;

- The minimum length of the time-list needed i.e. the sampling duration for processing was tested from 16-31 sec. As the recordings were done at 9Hz, this gives us 144-279 samples every time the signal is analyzed.
- The Welch Periodogram was used to analyze the output of this method with the following parameters;
    1. For all cases, the length of the segment chosen was 1 sec less than the length of the signal with sliding for every sample. E.g if the signal was 16 sec or 144 samples long, then for Welch analysis the signal was divided into 15 sec or 135 samples overlapping chunks with sliding of 1 sample between segments. This is done to reduce the white noise in the signal but not compromise on the frequency resolution.
    2. Both cases of channelized and non-channelized signals were considered. For channelized signals, the number of bands used were 2, 4, 8, 16 and 32.
    3. The following windowing methods were considered;
        (a) Boxcar
        (b) Triangular
        (c) Hamming
        (d) Hann
        (e) Bohman
        (f) Parzan
        (g) Nuttall
        (h) Flattop
        (i) Blackman-Harris
        (j) Bartlett-Hann
        (k) Kaiser ($\beta = 4, 8, 12$)

(l) Chebwin ($at = 100dB$)

(m) Tukey ($\alpha = 0.8, 0.5$)

4. For non-channelized signal, zero-padding was performed for 0-4 times the length of the signal; 0 times zero-padding implies that no zero padding was done. For channelized signal, zero-padding was performed for 0-2 times the length of the signal. The results for the channelized signal was not calculated when the nose was taken as the ROI.

- For the heart rate measurement, the range of frequencies that were being monitored were 54-90 bpm or 0.900-1.500Hz. For the heart rate measurement, the range of frequencies that were being monitored were 6-30 bpm or 0.100-0.500Hz.

8.1. Calculating Breath Rate

In order to analyze the breath rate from the thermal recordings, two different situations were considered;

- Monitoring the thermal behaviour of the nose. This is only possible for videos where the face and the nostrils are visible.
- Monitoring the thermal behaviour of the ROIs other than the nose. This is done to see if the thermal behaviour of other ROIs are comparable to the results from the ECG. For face videos, this will be used to compare how similar the results from the other ROIs is similar to that of the ECG and the nose.

In case of monitoring the nose and mouth region as the ROI for a 20 sec duration, all windowing methods appear to give quiet similar results except the Flattop window which seems to give a more erroneous result (see fig.B.1 and fig.B.2 in appendix). The Flattop window has provided with the worst results while most of the other windows provide a more desired output.

When the window length is 30 sec, all the windowing methods appear to provide the results similar to the ECG measurements. However, after reducing the window length to 20 sec, only Kaiser ($\beta = 12$) and Hamming window seem to provide better results. For 20 sec window length, other windowing methods like Bohman, Parzan, Nuttall and Dolph-Chebyshev(Chebwin) also provide better results(see fig.B.7 in appendix). None of the windowing methods were able to provide reasonable results at 15 sec window length and no zero-padding. After using zero-padding; the Kaiser ($\beta = 12$) widow of 15 sec length the results are comparable to using a 20 sec window (see fig.B.8 in appendix).

The effect of using different window lengths for windows can be seen in fig.B.3,B.4,B.5,B.6 in the appendix.

So, zero-padding the signal can help reduce the minimum size of the window needed for better results but only for one time the length of the original signal otherwise it seems to make the results more noisy. The same improvement in the results can also be seen for other windowing methods like Bohman, Parzan, Nuttall and Dolph-Chebyshev(Chebwin)(see fig.B.9 and fig.B.10 in appendix). The average RMSE of these methods can be seen in table.8.1.

Window	Bohman	Parzan	Nuttall	Kaiser ($\beta = 12$)	Dolph-Chebyshev
Average RMSE(bpm)	1.814±0.889	2.009±0.846	1.901±0.791	1.874±0.791	2.037±0.848

Table 8.1: Average RMSE for monitoring the nose for a window of 15 sec and zero-padding once the length of the signal.

There were a few results where the ECG provided with invalid measurements and that were visible in some of the analysis (see fig.B.16 in appendix) that the measurements follow the pattern of the ECG but with a significant offset. This happens because;

- ECG electrodes are not connected properly to the subject
- Subject being monitored was talking and/or laughing during the recordings

These faulty recordings were not used for breath rate analysis. However, they still provided viable heart rate measurements which will be used for analysis later.

In case of monitoring ROI's other than the nose, none of the results are comparable to that of the ECG recordings or from monitoring the nose. As shown in fig.8.2, there is no improvement in results despite using a 30

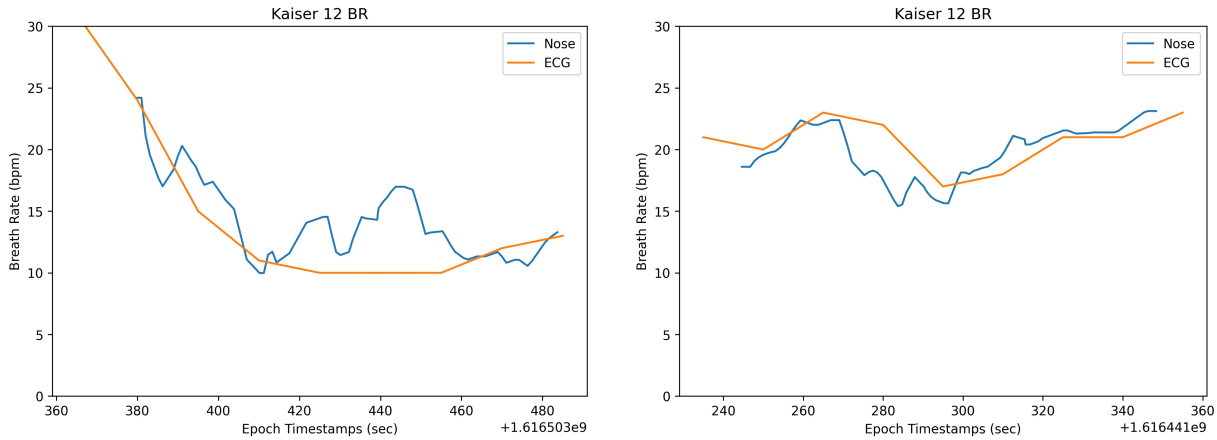

Figure 8.1: Results of monitoring breath rate from the nose using Kaiser ($\beta = 12$) window of 15 sec and zero-padding of once the length of the original signal

sec window or zero-padding. This is the same case despite using a channelizer or for other window lengths and irrespective of the ROIs other than the nose and mouth region that have been taken into consideration (see fig fig.B.12, fig.B.11, fig.B.10, fig.B.13, fig.B.14 and fig.B.15 in appendix).

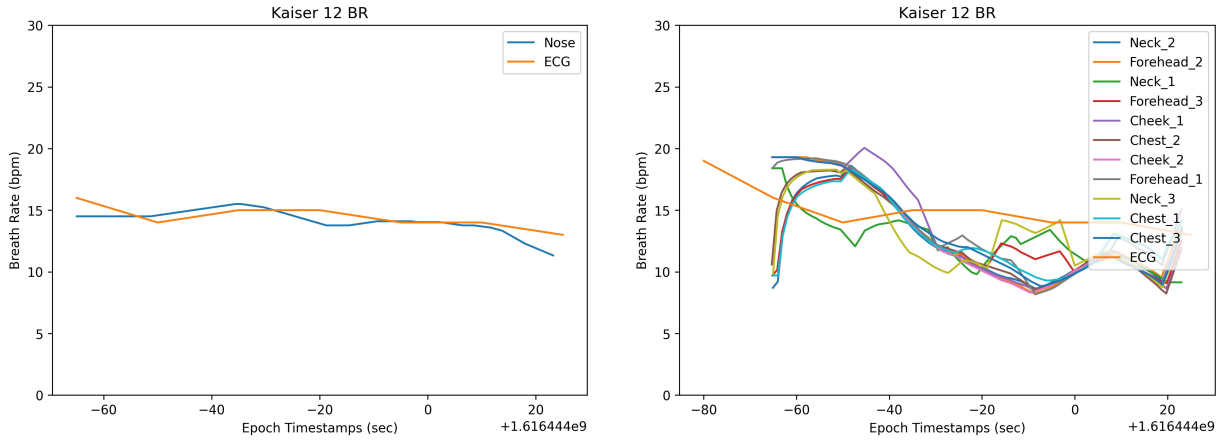

Figure 8.2: Results of monitoring the breath rate from (1) the nose, (2) ROIs other than the nose; for the same recording using Kaiser ($\beta = 12$) window of 30 sec and zero-padding of once the length of the original signal

As the other ROIs didnot provide reasonable results despite the use of different windowing methods, zero-padding and channelizer; monitoring the thermal activity of the nose is preferable for monitoring the breath rate as it would be easier to get results and it would react faster to any change in the breath rate. In table 8.1, the average RMSE of the best performing algorithms are shown; Bohman, Parzan, Nuttall, Kaiser ($\beta = 12$) and Dolph-Chebyshev windows of length 15 sec and zero-padding once the length of the signal. This shows an improvement in terms of computational intensity and performance as compared to algorithms shown in table 6.1.

8.2. Calculating Heart Rate

For heart rate monitoring, the ROIs considered are the face, leg, chest and back. Unlike analyzing the breath rate, the nose was not used as an ROI. Using a 30 sec window gives results quiet different than the ECG measurements (see fig.B.17 in appendix). The error between the measured and the calculated values can be greater than 10 bpm. However,if we use a 15 sec window instead, the Flattop window is able to provide better results when compared to the other windowing methods for different subjects and ROI as seen in fig.8.3. The average RMSE of these favourable results is around **4.246±0.659 bpm**. See fig.B.18, fig.B.19, fig.B.20 and

fig.B.23 in the appendix for results from more test cases.

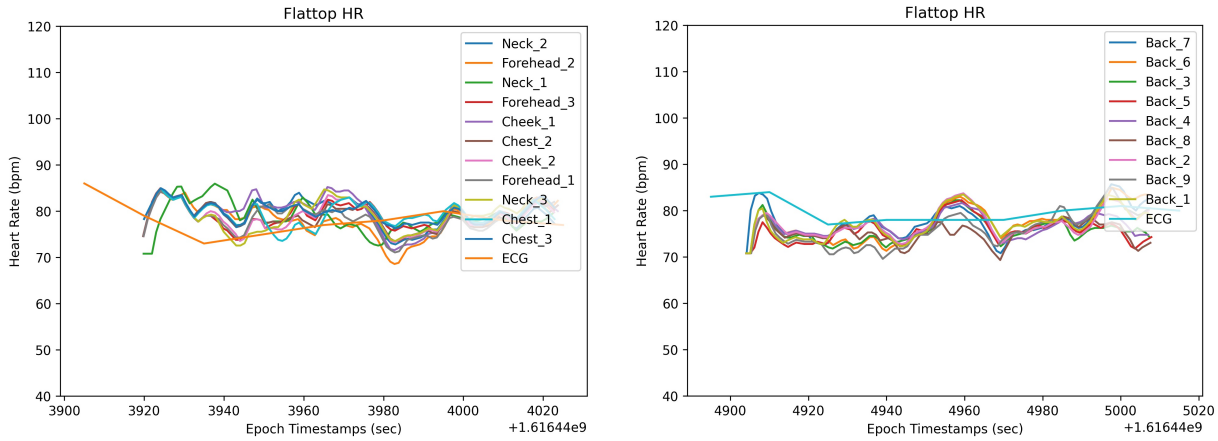

Figure 8.3: Results of monitoring the heart rate from (1) the face, (2) the back; using Flattop window of 15 sec and no zero-padding.

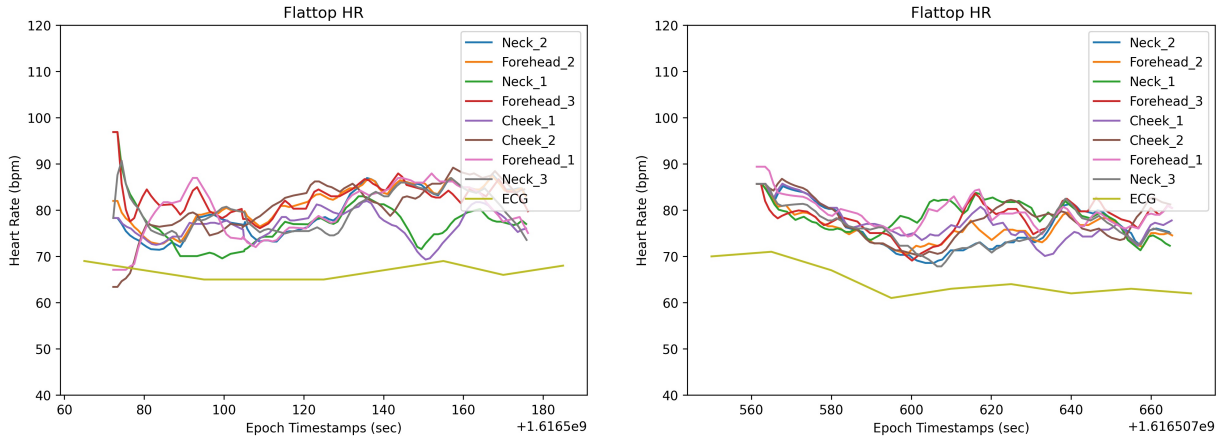

Figure 8.4: Results of monitoring the heart rate from the face for subjects different than the ones in fig.8.3 using Flattop window of 15 sec and no zero-padding.

Looking further into the other recordings, there were cases where despite the Flattop window providing us the best possible results, the error was still too high. For different cases, the results are either more chaotic or have a constant error when compared to the ECG recordings; as seen in fig.8.4 (see fig.B.26 in appendix for more results). The results are consistent despite of using zero-padding or a channelizer (see fig.B.24 and fig.B.25 in the appendix). The average RMSE for these recordings is **15.224±0.336 bpm** which is much higher compared to the other recordings.

The Flattop window is the only windowing method that was able to better results compared to the other windowing methods but despite that it was able to give more desired results for only half of the test cases while the other methods did not work as effectively for any of them. This could be possible either because of the difference in physiologies of the different test subjects in terms of age and fitness or because of the lower sampling rate (9Hz) that has been used compared to the other algorithms mentioned in table .6.2. So, for monitoring the heart rate of the subject using the PPG method used in other researches [68, 69] doesnot provide valid results for the system and the FLIR camera used for these experiments.

9

Conclusions

9.1. Research Goals

- To reduce the system requirements like frame rate or frame resolution for monitoring heart or breath rate in order to make the algorithm more computationally efficient. Other research have used frame rates of around **10-60 fps/Hz** with a frame resolution of **640x480** or higher. The frame rate used in this project is around **9 fps/Hz** with a frame resolution of **320x240**.
- To be able to measure breath rate from the nose region and from ROIs other than the nose and compare to see if they have similar performance so that breath rate monitoring is not dependent on one ROI unlike previous research[30, 66, 67].
- To be able to acquire the heart rate using methods similar to remote photoplethysmography(rPPG) rather than isolating the superficial blood vessels in the ROI being monitored.
- To be able to acquire both heart rate and breath rate from the same ROI (other than the nose) like the forhead or cheek etc as used in rPPG applications by other research [67–70].
- To make the algorithm motion robust by using image processing techniques to track the selected ROI rather than face recognition as used by other research [67–70].

9.2. Research Conclusions

Comparison between the previous research and the implementation used for this project for breath rate monitoring [30, 66, 67] and heart rate [15, 66, 68] are shown in tables.9.1 and 9.2 respectively.

The results of this research are:

- This system can calculate the breath rate of the subject by monitoring the thermal activity of the nose and mouth region at a frame rate of 9 fps and frame resolution of 320x240 pixels for a sampling duration of 15 sec by using a Welch Periodogram with windowing methods like Bohman, Parzan, Nuttall, Kaiser ($\beta = 12$) and Dolph-Chebyshev providing an average RMSE of around 1.814 ± 0.889 bpm. This work has shown that we are able to calculate the breath rate of a subject with lower frame rate, frame resolution and sampling duration making it more efficient than that of the previous research[30, 66, 67].
- Calculating the breath rate by monitoring the thermal activity from ROIs other than the nose leads to RMSE of 6.413 ± 0.337 bpm which is much higher error than the results calculated by monitoring the nose and also from the results of previous research[30, 66, 67]. So, it is not possible to get the breath rate of the subject by monitoring ROIs other than the nose.
- The photoplethysmographic (PPG) method of monitoring the heart rate from thermal recordings in this system gave mixed results. The best performance was provided by using the Flattop window of 15 sec length and no zero-padding with results having RMSE of $4.246 \pm 0.659 bpm$ in the best case scenarios and around 15.224 ± 0.336 bpm in the worst case scenarios; accuracy in range of 75-95%. These results are not better than the previous research[15, 66, 68] which gave an RMSE around 2.8 bpm. This may be

Previous Research	**Project's Current Implementation**
Only monitored the thermal activity of the nose, other ROI was not explored extensively (only chest movement)	ROIs ranging from face, chest, back and arms/legs were also considered
The ROI tracking involved face recognition	A different and less computationally intensive ROI tracking algorithm was used
Spectral analysis methods included either wavelet transform or a Standard Periodogram using Hamming/Hann window	The Standard, Welch and Lomb-Scargle Periodograms were considered with 16 different windowing methods, zero-padding and channelizer
Distance between the camera and the subject was around 1.2m	Distance between the camera and the subject was around 1.2-1.5m
Frame rates used was around 10-60 fps	Frame rates used was around 9 fps
Frame resolution is atleast 640x480 fps	Frame resolution is 320x240
Almost all the research has used at least 30sec of sampling duration to get an error of 2.2 br/min. Those that used 15sec sampling duration had RMSE of around 4.15 ± 1.44 br/min	Achieved RMSE of around 1.814 ± 0.889 br/min using a 15sec sampling duration

Table 9.1: Comparison of breath rate algorithms with other research

Previous Research	**Project's Current Implementation**
Monitored ROI mostly on the face like the forehead, neck or the cheek and in some cases the hand	ROIs ranging from face, chest, back and arms/legs were also considered
The ROI tracking involved face recognition	A different and less computationally intensive ROI tracking algorithm was used
Heart rate was calculated by either isolating blood vessels from the recordings or just selecting a specific ROI region like the forehead or cheek and then performing frequency analysis i.e. remote photplethysmography(rPPG)	All the ROIs were analyzed using rPPG method
Spectral analysis methods included either wavelet transform or a Standard Periodogram using Hamming/Hann window	The Standard, Welch and Lomb-Scargle Periodograms were considered with 16 different windowing methods, zero-padding and channelizer
Distance between the camera and the subject was around 1.2m	Distance between the camera and the subject was around 1.2-1.5m
Frame rates is around 15-60 fps for rPPG	Frame rates used was around 9 fps
Frame resolution is atleast 640x480 for rPPG	Frame resolution is 320x240
Only ECG was used to measure heart rate	ECG and digital sphygmomanometer was used
Used sampling duration of 30sec to get an average error of 2.8 bpm	Using digital sphygmomanometer gave error of get an average error of 1.8 bpm but the ECG gave RMSE of atleast 4.246 ± 0.659 bpm

Table 9.2: Comparison of heart rate algorithms with other research

because of the lower sampling rate of the setup. So for the current limitations of the setup used for the research, the PPG method of monitoring the heart rate will not provide valid results[9, 59].

- The breath rate monitoring is dependent on the nose region to provide with less error and faster response as compared to other ROIs. This eliminates the possibility of measuring breath rate from monitoring the thermal activity of ROIs other than the nose. This also eliminates the possibility of acquiring both heart and breath rate from other ROIs simultaneously for the setup used in this project.
- The average error of measuring heart rate using a digital sphygmomanometer (DSPHG) is **1.8 bpm** with an average accuracy of 97%. However, the auscultatory method of monitoring heart rate used by a DSPHG contributes to the temperature fluctuations which in turn contributes to the final output. So, it is important to use a vitals monitoring device which does not affect the output of the experiments;

making ECG a more viable option for monitoring.

9.3. Recommendations for Future Work

- Creating more thermal recordings for both neonates and adults can help test the algorithm for multiple situations.
- Investigating the possibility of acquiring breath rate from ROIs other than the nose over more number of test cases.
- Investigating the effect of distance on the accuracy of the measurements and exploring the maximum possible range for test cases in a closed room and open room situation.
- Investigate if a higher frame rate for the spectral analysis methods used in this project improves the performance of the method used for heart rate measurement in thermal imaging.
- Exploring using the other spectral analysis methods like Polyphase-FFT Filter Bank,Welch or Lomb-Scargle Periodograms with different windowing methods for non-contact monitoring of other vitals like HRV, blood pressure or SPO2 in both RGB and thermal imaging.
- Improving the working of the ROI tracking algorithm could improve its speed and reduce computational load.

List of Abbreviations

BF Brute-Force

BPM Beats/Breaths per Min

BRIEF Binary Robust Independent Elementary Features

BR Breath Rate

CSV Comma-Separated Value

DSPHG Digital Sphygmomanometer

ECG Electrocardiogram

FAST Features from Accelerated Segment Test

FFT Fast Fourier Transform

FIR Far Infrared

FLANN Fast Library for Approximate Nearest Neighbors

FOV Field of View

FPS Frames per Second

GA Gestational Age

GLOH Gradient Location-Orientation Histogram

GUI Graphical User Interface

HR Heart Rate

IR Infrared

LWIR Long Wave Infrared

MWIR Mid Wave Infrared

NIR Near Infrared

NUC Non-Uniformity Correction

ORB Oriented FAST and Rotated BRIEF

PPG Photplethysmography

PSD Power Spectral Density

RMSE Root Mean Square Error

ROI Region of Interest

SIFT Scale Invariant Feature Transform

SPO2 Oxygen Saturation

SURF Speeded-Up Robust Features Descriptor

TCP/IP Transmission Control Protocol/Internet Protocol

Bibliography

[1] **Embedded Neonatal Respiration Monitoring**: *Hoeben, R. M., and Technische Universiteit Eindhoven (TUE). Stan Ackermans Instituut. Design and Technology of Instrumentation (DTI) (2011). Embedded neonatal respiration monitoring. Eindhoven: Technische Universiteit Eindhoven.*

[2] **Neonatal non-contact respiratory monitoring based on real-time infrared thermography**: *Abbas K Abbas, Konrad Heimann, Katrin Jergus, Thorsten Orlikowsky and Steffen Leonhardt, BioMed Eng OnLine 10, 93 (2011). https://doi.org/10.1186/1475-925X-10-93*

[3] **Intelligent neonatal monitoring based on a virtual thermal sensor**: *Abbas K Abbas and Steffen Leonhardt, BMC medical imaging. https://doi.org/10.1186/1471-2342-14-9.*

[4] **Thermoregulation and Thermography in Neonatal Physiology and Disease**: *Robin B. Knobel, Bob D. Guenther and Henry E. Rice, Biol Res Nurs. 2011 Jul;13(3):274-82. doi: 10.1177/1099800411403467. Epub 2011 May 17. PMID: 21586499; PMCID: PMC3775585.*

[5] **A Calibration Approach for Accuracy Infrared Temperature**: *Liang Yan-hua and Qian Ze-dong, 2016 International Conference on Intelligent Networking and Collaborative Systems (INCoS), 2016, pp. 407-410, doi: 10.1109/INCoS.2016.37.*

[6] **Contactless monitoring of heart and respiratory rate in anesthetized pigs using infrared thermography**: *Carina Barbosa Pereira, Henriette Dohmeier, Janosch Kunczik, Nadine Hochhausen, René Tolba, Michael Czaplik, PLoS One. 2019 Nov 6;14(11):e0224747. doi: 10.1371/journal.pone.0224747. PMID: 31693688; PMCID: PMC6834247.*

[7] **Forehead reflectance photoplethysmography to monitor heart rate: preliminary results from neonatal patients**: *M.R.Grubb, J.Carpenter, J.A.Crowe, J.Teoh, N.Marlow, C.Ward, C.Mann, D.Sharkey and B.R.Hayes-Gill, Physiol Meas. 2014 May;35(5):881-93. doi: 10.1088/0967-3334/35/5/881. Epub 2014 Apr 17. PMID: 24742972.*

[8] **Monitoring of Heart and Respiratory Rates in Newborn Infants Using a New Photoplethysmographic Technique**: *Anders Johansson, Per Aîke Oëberg and Gunnar Sedin, J Clin Monit Comput. 1999 Dec;15(7-8):461-7. doi: 10.1023/a:1009912831366. PMID: 12578044.*

[9] **Non-Contact, Simple Neonatal Monitoring by Photoplethysmography**: *Juan-Carlos Cobos-Torres, Mohamed Abderrahim and José Martínez-Orgado, Sensors (Basel). 2018;18(12):4362. Published 2018 Dec 10. doi:10.3390/s18124362*

[10] **Heart Rate Monitoring in Newborn Babies: A Systematic Review**: *Oana Anton, Ramon Fernandez, Elizabeth Rendon-Morales, Rodrigo Aviles-Espinosa, Harriet Jordan, Heike Rabe, Neonatology. 2019;116(3):199-210. doi: 10.1159/000499675. Epub 2019 Jun 27. PMID: 31247620.*

[11] **Review of Biomedical Applications of Contactless Imaging of Neonates Using Infrared Thermography and Beyond**: *Abbas K. AlZubaidi, Yahya Ethawi, Georg M. Schmölzer, Michael Narvey and Molly Seshia, Methods Protoc. 2018;1(4):39. Published 2018 Oct 29. doi:10.3390/mps1040039*

[12] **Noncontact Detection of Respiration Rate Based on Forward Scatter Radar**: *Fan Yang, Zhiming He, Yuanhua Fu, Liang Li, Kui Jiang and Fangyan Xie, Sensors 2019, 19, 4778. https://doi.org/10.3390/s19214778*

[13] **Non-Contact Respiratory Monitoring in Neonates**: *Caillin Eastwood-Suthedand, Timothy J. Galet, Peter A. Dargaville and Kevin Wheeler, The 7th 2014 Biomedical Engineering International Conference, 2014, pp. 1-5, doi: 10.1109/BMEiCON.2014.7017373.*

[14] **Neonatal infrared thermography imaging: Analysis of heat flux during different clinical scenarios**: *Abbas, A. K., Heimann, K., Blazek, V., Orlikowsky, T., & Leonhardt, S. (2012).* Infrared Physics & Technology, 55(6), 538–548. https://doi.org/10.1016/j.infrared.2012.07.001

[15] **Contact-Free Measurement of Cardiac Pulse Based on the Analysis of Thermal Imagery**: *Marc Garbey, Nanfei Sun, Arcangelo Merla, and Ioannis Pavlidis, IEEE Transactions on Biomedical Engineering, vol. 54, no. 8, pp. 1418-1426, Aug. 2007, doi: 10.1109/TBME.2007.891930.*

[16] **Automated Respiration Detection from Neonatal Video Data**: *Ninah Koolen, Olivier Decroupet, Anneleen Dereymaeker, Katrien Jansen, Jan Vervisch, Vladimir Matic, Bart Vanrumste, Gunnar Naulaers, Sabine Van Huffel and Maarten De Vos, ICPRAM 2015 - 4th International Conference on Pattern Recognition Applications and Methods, Proceedings. 2. 10.5220/0005187901640169.*

[17] **Real-Time Vision Based Respiration Monitoring System**: *K. S. Tan, R. Saatchi, H. Elphick, and D. Burke, 2010 7th International Symposium on Communication Systems, Networks & Digital Signal Processing (CSNDSP 2010), 2010, pp. 770-774, doi: 10.1109/CSNDSP16145.2010.5580316.*

[18] **Remote Respiration Rate Determination in Video Data Vital Parameter Extraction based on Optical Flow and Principal Component Analysis**: *Christian Wiede, Julia Richter, Manu Manuel and Gangolf Hirtz*

[19] **Video-based respiration monitoring with automatic region of interest detection**: *Janssen, R.J.M., Wang, W., Moço, A., & de Haan, G. (2016). Video-based respiration monitoring with automatic region of interest detection. Physiological Measurement, 37(1), 100-114. https://doi.org/10.1088/0967-3334/37/1/100*

[20] **Combination of near-infrared and thermal imaging techniques for the remote and simultaneous measurements of breathing and heart rates under sleep situation**: *Menghan Hu, Guangtao Zhai, Duo Li, Yezhao Fan, Huiyu Duan, Wenhan Zhu, Xiaokang Yang. https://doi.org/10.1371/journal.pone.0190466*

[21] **Remote Heart Rate Monitoring Method Using Infrared Thermal Camera**: *Yoonkyoung Kim, Yosep Park, Jinman Kim, Eui Chul Lee, International Journal of Engineering Research and Technology, Volume 11,2018,pp 493-500*

[22] **Intermediate Physics for Medicine and Biology**: *Hobbie, R. K., & Roth, B. J. (2015)* https://doi.org/10.1007/978-3-319-12682-1

[23] **Wideband optical transmission properties of seven thermoplastics**: *Lytle, J. D., Wilkerson, G. W., & Jaramillo, J. G. (1979).* Applied Optics, 18(11), 1842. https://doi.org/10.1364/ao.18.001842

[24] **Basic heat and mass transfer (Third ed.)**: *Mills, A., & Coimbra, Carlos F.M. (2015).* San Diego, California: Prentice Hall.

[25] **Non-contact skin emissivity: measurement from reflectance using step change in ambient radiation temperature**: *Togawa, T. (1989). Clinical Physics and Physiological Measurement, 10(1), 39–48. https://doi.org/10.1088/0143-0815/10/1/004*

[26] **Spectral emissivity of skin and pericardium**: *Steketee, J. (1973).* Physics in Medicine and Biology, 18(5), 686–694. https://doi.org/10.1088/0031-9155/18/5/307

[27] **Contactless heart rate variability measurement by IR and 3D depth sensors with respiratory sinus arrhythmia**: *Kaveh Bakhtiyari, Nils Beckmann, Jürgen Ziegler, Procedia Computer Science Volume 109 2017,Pages 498-505, ISSN 1877-0509, https://doi.org/10.1016/j.procs.2017.05.319.*

[28] **Effect of respiratory pattern on automated clinical blood pressure measurement: an observational study with normotensive subjects**: *Natalia Herakova, Nnenna Harmony Nzeribe Nwobodo, Ying Wang, Fei Chen and Dingchang Zheng, Clin Hypertens 23, 15 (2017). https://doi.org/10.1186/s40885-017-0071-3*

[29] **Infrared thermography : errors and uncertainties**: *Minkina, W. & Dudzik, S. (2009). Chichester, U.K: J. Wiley.*

[30] **Noncontact Monitoring of Respiratory Rate in Newborn Infants Using Thermal Imaging**: *Carina Barbosa Pereira, Xinchi Yu, Tom Goos, Irwin Reiss, Thorsten Orlikowsky, Konrad Heimann, Boudewijn Venema , Vladimir Blazek, Steffen Leonhardt and Daniel Teichmann, IEEE Transactions on Biomedical Engineering, vol. 66, no. 4, pp. 1105-1114, April 2019, doi: 10.1109/TBME.2018.2866878.*

[31] **Observations on the finger volume pulse recorded photoelectrically**: *Hertzman AB, Spealman CR., Am. J. Physiol 1937;119:334–335.*

[32] **Photoplethysmography and its application in clinical physiological measurement**: *Allen, J.Physiol. Meas. 2007 Mar;28(3):R1-39. doi: 10.1088/0967-3334/28/3/R01. Epub 2007 Feb 20. PMID: 17322588.*

[33] **Visible and invisible mirages: Comparing inferior mirages in the visible and thermal infrared**: *Vollmer, Michael, Shaw, Joseph & Nugent, Paul. (2015).* Applied Optics. 54. 10.1364/AO.54.000B76.

[34] **ORB: an efficient alternative to SIFT or SURF**: *Ethan Rublee, Vincent Rabaud, Kurt Konolige, Gary Bradski, 2011 International Conference on Computer Vision, 2011, pp. 2564-2571, doi: 10.1109/ICCV.2011.6126544.*

[35] **Image Feature Detectors and Descriptors**: *Ali Ismail Awad, Mahmoud Hassaballah*

[36] **Computer Vision:Algorithms and Applications**: *Richard Szeliski*

[37] **Image Matching Using SIFT, SURF, BRIEF and ORB: Performance Comparison for Distorted Images**: *Ebrahim Karami, Siva Prasad, and Mohamed Shehata*

[38] **Scalable Nearest Neighbor Algorithms for High Dimensional Data**: *Marius Muja and David G. Lowe, IEEE Transactions on Pattern Analysis and Machine Intelligence, vol. 36, no. 11, pp. 2227-2240, 1 Nov. 2014, doi: 10.1109/TPAMI.2014.2321376.*

[39] **TCP/IP Network Administration**: *Craig Hunt, Third Edition*

[40] **Two-Frame Motion Estimation Based on Polynomial Expansion**: *Gunnar Farnebäck, Computer Vision Laboratory, Linköping University,SE-581 83 Linköping, Sweden,http://www.isy.liu.se/cvl/*

[41] **Mathematical Models in Computer Vision: The Handbook**: *N.Paragios, Y.Chen and O.Faugeras, Chapter 15, Springer, 2005, pp. 239-258*

[42] **The Computation of Optical Flow**: *S.S.Beauchemin and J.L.Barron, ACM Computing Surveys Vol. 27, No. 3, pp. 433-467, 1995*

[43] **The Use of the Fast Fourier Transform for the Estimation of Power Spectra: A method based on time averaging over short, modified periodograms**: *P. Welch, IEEE Trans. Audio Electroacoust. vol. 15, pp. 70-73, 1967, IEEE Transactions on Audio and Electroacoustics, vol. 15, no. 2, pp. 70-73, June 1967, doi: 10.1109/TAU.1967.1161901.*

[44] **Least-Squares Frequency Analysis of Unequally Spaced Data**: *N.R. Lomb , Astrophysics and Space Science, vol 39, pp. 447-462, 1976, https://doi.org/10.1007/BF00648343*

[45] **Fast Calculation of the Lomb-Scargle Periodogram using Graphics Processing Units**: *R.H.D. Townsend,The Astrophysical Journal Supplement Series, vol 191, pp. 247-253, 2010, doi: 10.1088/0067-0049/191/2/247*

[46] **Multirate Filtering for Digital Signal Processing**: *Harris, Fredric J, Prentice Hall PTR, 2004*

[47] **Thermal Image Resolution on Angular Emissivity Measurements using Infrared Thermography**: *Nunak, T., Rakrueangdet, K., Nunak, N. & Suesut, Taweepol. (2015).*

[48] **A Practical Guide to Splines**: *Carl de Boor, Springer-Verlag, 1978*

[49] **Numerical Analysis-Ninth Edition**: *Richard L. Burden, J. Douglas Faires, 1978, pp. 144-164*

[50] **Contact-Based Methods for Measuring Respiratory Rate**: *Carlo Massaroni, Andrea Nicolò, Daniela Lo Presti, Massimo Sacchetti, Sergio Silvestri and Emiliano Schena; Sensors 2019, 19, 908;* doi:10.3390/s19040908

[51] **Non-Contact Measurement of Heart and Respiration Rates based on Kinect**: *Natascia Bernacchia, Lorenzo Scalise, Luigi Casacanditella, Ilaria Ercoli, Paolo Marchionni, Enrico Primo Tomasini, 2014 IEEE International Symposium on Medical Measurements and Applications (MeMeA), 2014, pp. 1-5, doi: 10.1109/MeMeA.2014.6860065.*

[52] **Remote Respiration Rate Determination in Video Data: Vital Parameter Extraction based on Optical Flow and Principal Component Analysis**: *Christian Wiede, Julia Richter, Manu Manuel and Gangolf Hirtz,* DOI: 10.5220/0006095003260333, ISBN: 978-989-758-225-7

[53] **Encyclopedia of Medical Devices and Instrumentation - Second Edition** : *John G. Webster, 2006, Volume-1,3,5*

[54] **Design of Heart Rate Monitor based on Piezoelectric Sensor using an Arduino**: *Veni Setyowati1, Jodelin Muninggar, Made R. S. Shanti.N.A,*doi:10.1088/1742-6596/795/1/012016

[55] **Non-contact heart rate tracking using Doppler radar**: *H. Tan, D. Qiao and Y. Li, 2012 International Conference on Systems and Informatics (ICSAI2012), 2012, pp. 1711-1714, doi: 10.1109/ICSAI.2012.6223372.*

[56] **Measurement of respiration rate in preterm infants by laser Doppler vibrometry**: *L. Scalise, I. Ercoli, P. Marchionni and E. P. Tomasini, 2011 IEEE International Symposium on Medical Measurements and Applications, 2011, pp. 657-661, doi: 10.1109/MeMeA.2011.5966740.*

[57] **A Neonatal Thorax Phantom for Contact-less Magnetic Induction Vital Parameter Monitoring**: *A. Cordes, N. Conzelmann and S. Leonhardt, 2012 Annual International Conference of the IEEE Engineering in Medicine and Biology Society, 2012, pp. 1161-1164, doi: 10.1109/EMBC.2012.6346142.*

[58] **Ultrasound sensors and its application in human heart rate monitoring**: *A. Shahshahani, D. R. Nafchi and Z. Zilic, 2017 IEEE International Symposium on Circuits and Systems (ISCAS), 2017, pp. 1-4, doi: 10.1109/ISCAS.2017.8050899.*

[59] **Remote PPG based Vital Sign Measurement using Adaptive Facial Regions**: *H. E. Tasli, A. Gudi and M. den Uyl, 2014 IEEE International Conference on Image Processing (ICIP), 2014, pp. 1410-1414, doi: 10.1109/ICIP.2014.7025282.*

[60] **Hybrid Optical Imaging Technology for long-term Remote Monitoring of Skin Perfusion and Temperature Behavior**: *Nikolai Blanik, Abbas K. Abbas, B.V.V.B.S.L. Journal of Biomedical Optics 2014, 19, 19–19 –11. doi:10.1117/1.JBO.19.1.016012*

[61] **Optical imaging in medicine: II. Modelling and Reconstruction- Physics in Medicine and Biology**: *Arridge, S.R.; Hebden, J.C. 1997, 42, 841*

[62] **Infrared thermography imaging for contactless neonatal monitoring and care**: *Abbas, A.K. ; Number 24 in Aachener Beiträge zur Medizintechnik, Shaker: Aachen, 2015*

[63] **Development of noninvasive measurement of peripheral circulation and its medical application**: *Nakamura, H. Environmental Health and Preventive Medicine 1997, 2, 1. doi:10.1007/BF02931222.*

[64] **Analysis of Breathing Air Flow Patterns in Thermal Imaging**: *J. Fei and I. Pavlidis, 2006 International Conference of the IEEE Engineering in Medicine and Biology Society, 2006, pp. 946-952, doi: 10.1109/IEMBS.2006.260117.*

[65] **Exploratory Study to Evaluate Respiratory Rate Using a Thermal Imaging Camera**: *Elphick HE, Alkali AH, Kingshott RK, Burke D, Saatchi R. 2019;97(3):205-212. doi: 10.1159/000490546. Epub 2019 Jan 3. PMID: 30605906.*

[66] **Vital sign estimation from passive thermal video**: *Ming Yang, Qiong Liu, T. Turner and Ying Wu, 2008 IEEE Conference on Computer Vision and Pattern Recognition, 2008, pp. 1-8, doi: 10.1109/CVPR.2008.4587826.*

[67] **Contact-Free Respiration Rate Monitoring Using a Pan–Tilt Thermal Camera for Stationary Bike Telerehabilitation Sessions**: *R. Chauvin et al. in IEEE Systems Journal, vol. 10, no. 3, pp. 1046-1055, Sept. 2016, doi: 10.1109/JSYST.2014.2336372.*

[68] **A Non-contact Method for Extracting Heart and Respiration Rates**: *C. Hessler, M. Abouelenien and M. Burzo, 2020 17th Conference on Computer and Robot Vision (CRV), 2020, pp. 1-8, doi: 10.1109/CRV50864.2020.00009.*

[69] **Thermal Camera Based Physiological Monitoring with an Assistive Robot**: *S. Coşar, Z. Yan, F. Zhao, T. Lambrou, S. Yue and N. Bellotto, 2018 40th Annual International Conference of the IEEE Engineering in Medicine and Biology Society (EMBC), 2018, pp. 5010-5013, doi: 10.1109/EMBC.2018.8513201.*

[70] **Non-Contact Photoplethysmogram and Instantaneous Heart Rate Estimation from Infrared Face Video**: *N. Martinez, M. Bertran, G. Sapiro and H. Wu, 2019 IEEE International Conference on Image Processing (ICIP), 2019, pp. 2020-2024, doi: 10.1109/ICIP.2019.8803109.*

[71] **Motion Robust Remote-PPG in Infrared**: *M. van Gastel, S. Stuijk and G. de Haan, IEEE Transactions on Biomedical Engineering, vol. 62, no. 5, pp. 1425-1433, May 2015, doi: 10.1109/TBME.2015.2390261.*

Appendices

A

Appendix: Results of Experiments with Digital Sphygmomanometer

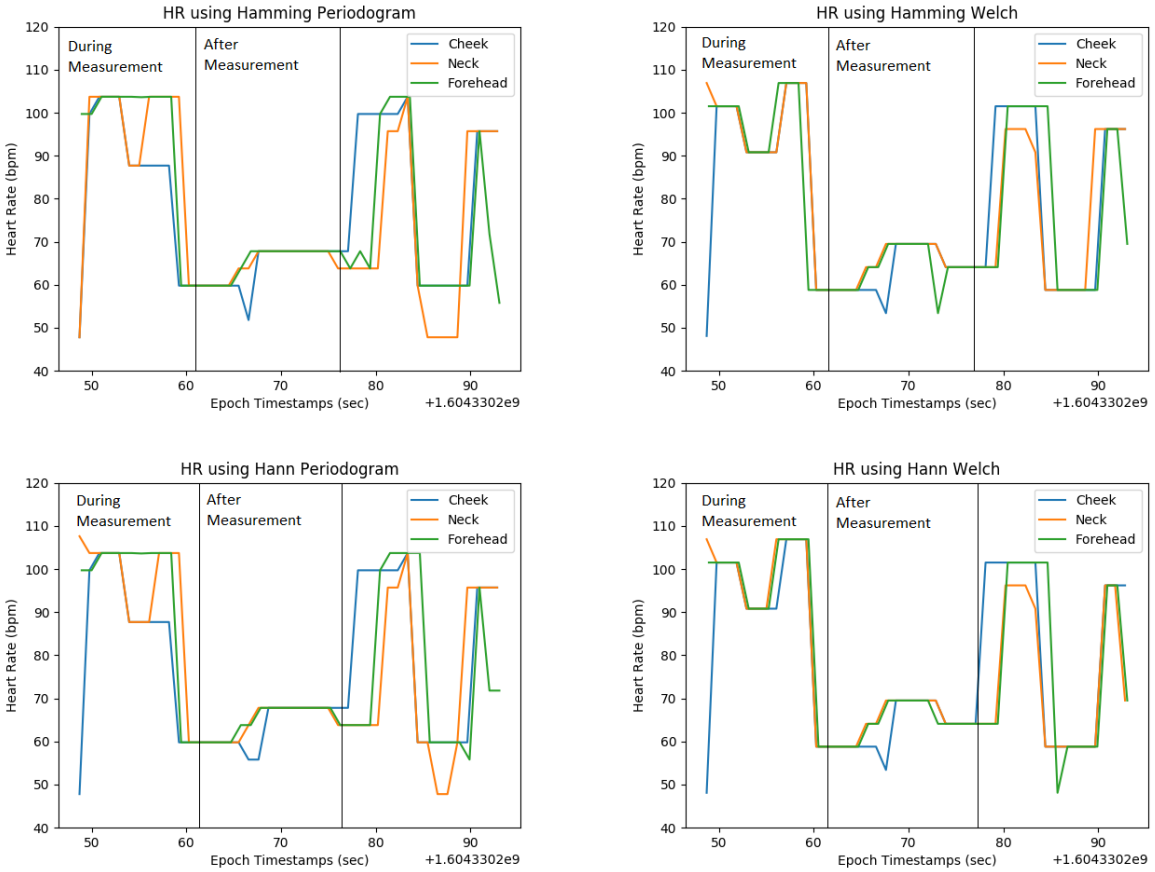

Figure A.1: Results of monitoring ROIs on the face with recorded heart rate of 60 bpm and a 15 sec window was used.

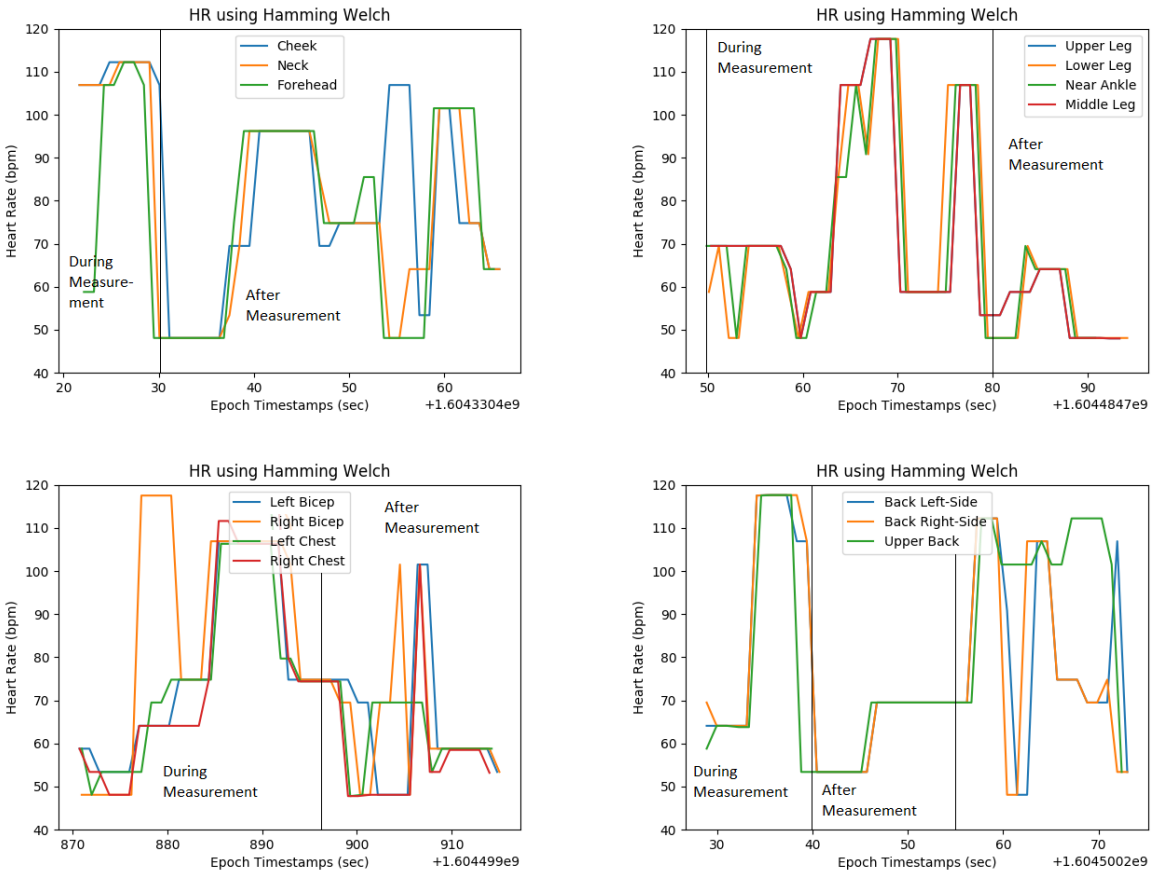

Figure A.2: Results of monitoring ROIs on the (1)face (48 bpm), (2)right leg (65 bpm), (3)chest (81 bpm), (4)back (87 bpm). A 15 sec window was used.

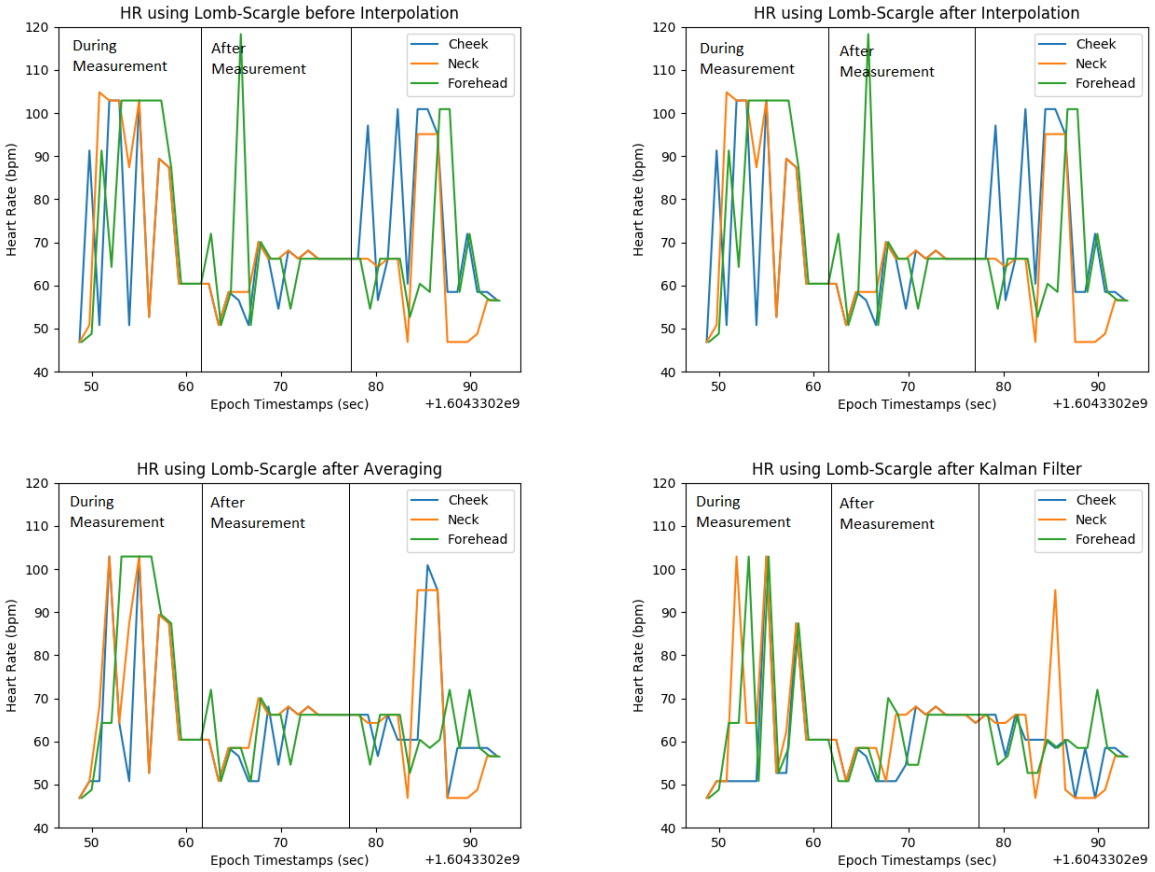

Figure A.3: Results of monitoring the same ROIs and signal as shown in fig.A.1

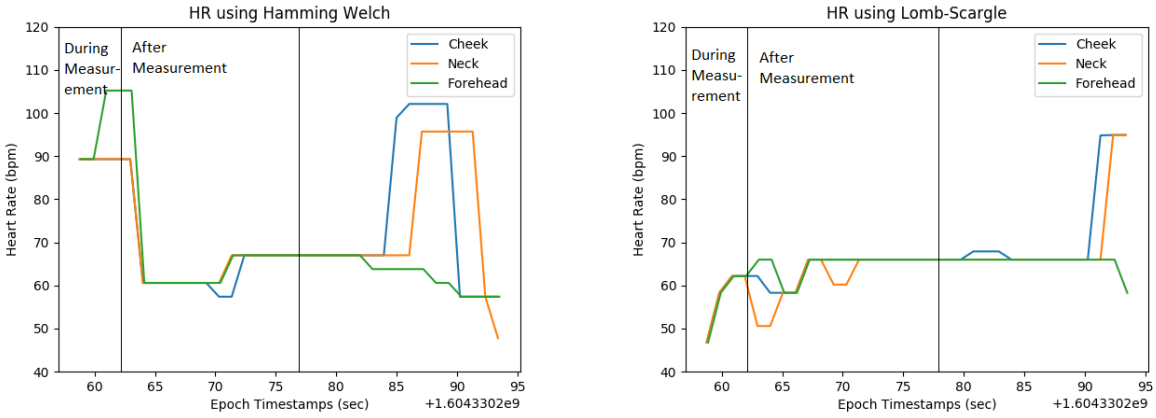

Figure A.4: Results of monitoring the same ROIs and signal as shown in fig.A.1 but using a 25 sec window instead of 15 sec

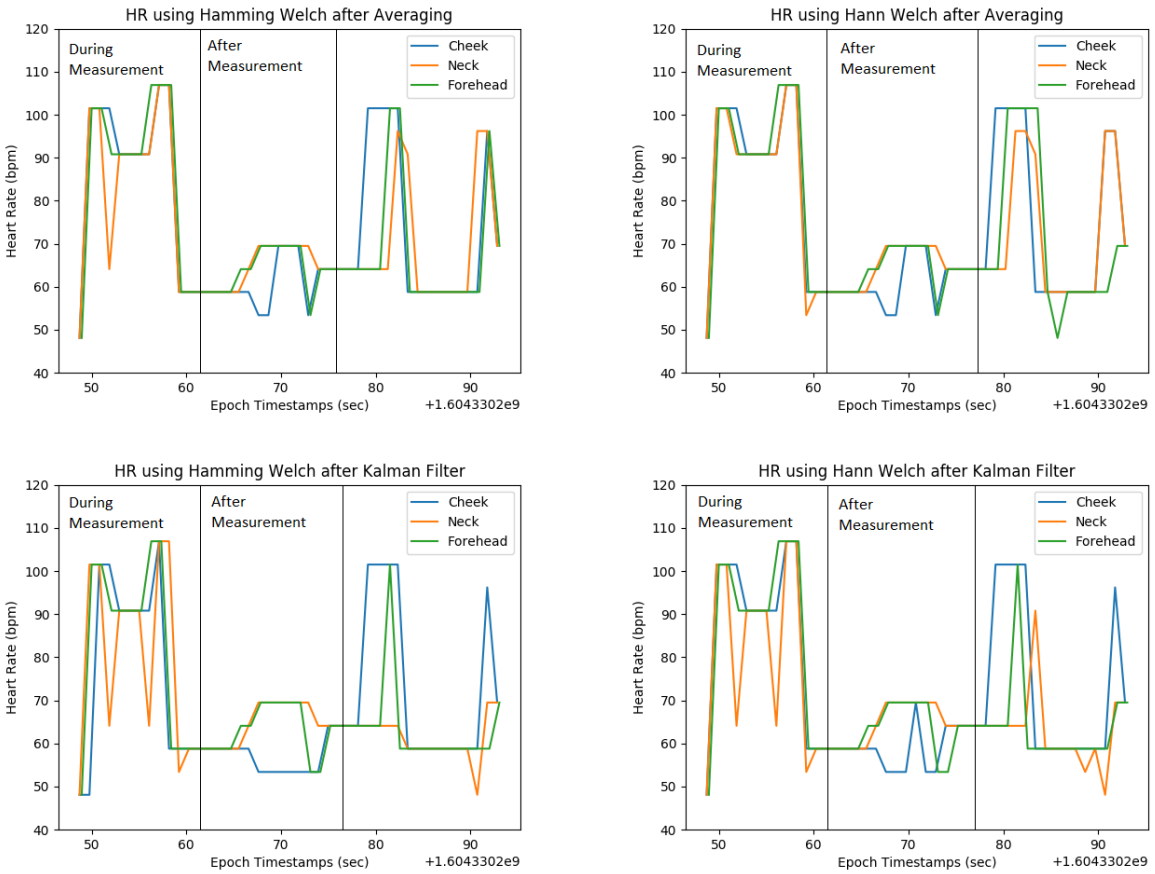

Figure A.5: Results of monitoring the same ROIs and signal as shown in fig.A.1 after the signals have been smoothened using either a moving average or a kalman filter.

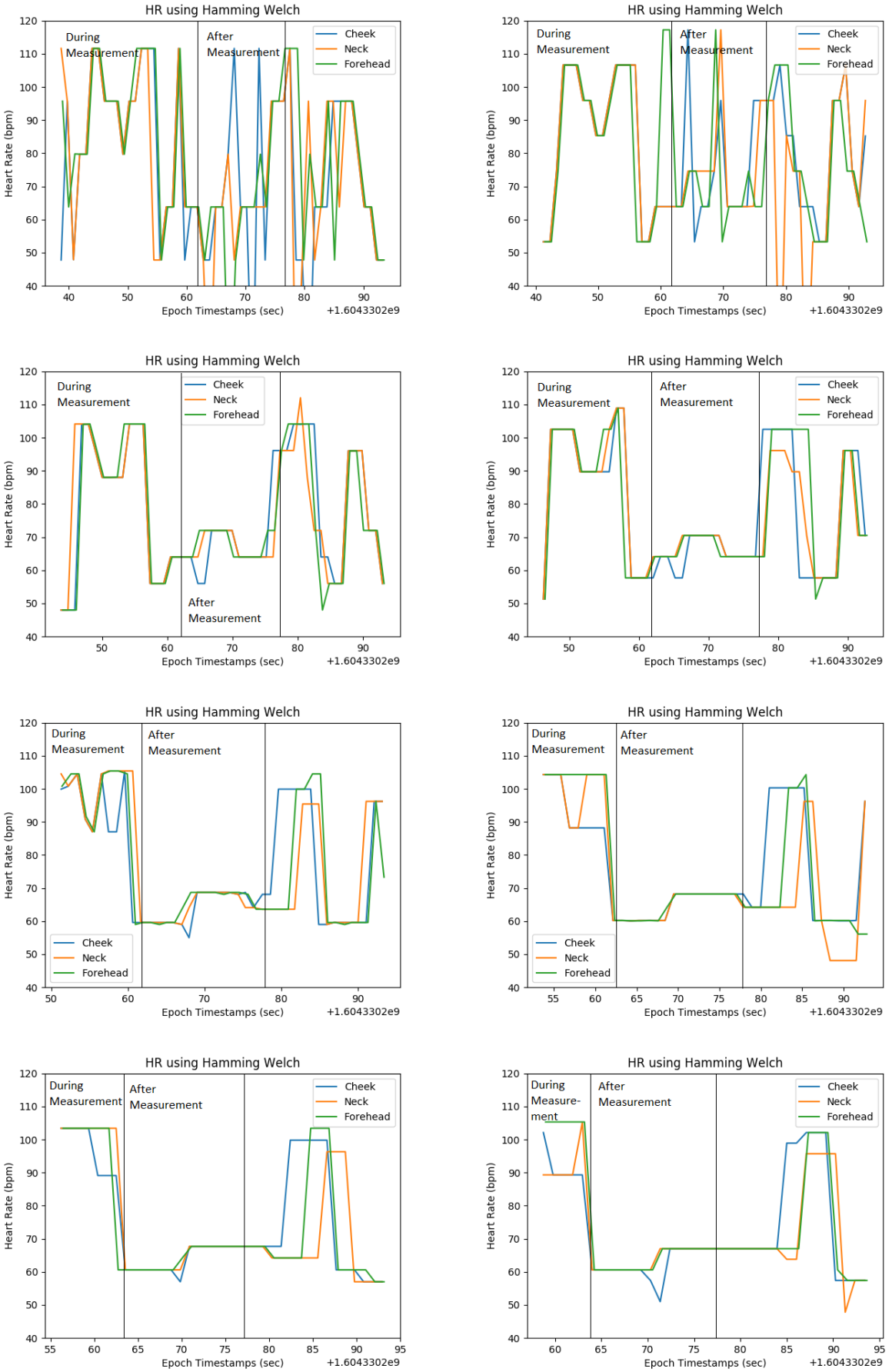

Figure A.6: Results of monitoring the same ROIs and signal as shown in fig.A.1 but using window length other than 15 sec; (1) 5 sec, (2) 7.5 sec, (3) 10 sec, (4) 12.5 sec, (5) 17.5 sec, (6) 20 sec, (7) 22.5 sec, (8) 25 sec

ROI	Measured Heart Rate(bpm)	Calculated Heart Rate(bpm)	Error(bpm)	Accuracy(%)
Face	48	48.1	0.1	99.79
Face	48	48.8	0.8	98.33
Face	53	53.4	0.4	99.24
Face	53	54.4	1.4	97.35
Face	60	58.8	1.2	98.00
Face	60	64.1	4.1	93.16
Face	68	64.1	3.9	94.26
Face	68	68.5	0.5	99.26
Face	69	69.5	0.5	99.27
Face	69	64.1	4.9	92.89
Face	70	74.8	4.8	93.14
Face	70	69.5	0.5	99.28
Face	75	69.5	5.5	92.66
Face	75	74.8	0.2	99.73
Face	76	80.1	4.1	94.60
Face	76	74.8	1.2	98.42
Face	82	85.5	3.5	95.73
Face	82	77.9	4.1	95.00
Face	82	86.9	4.9	94.02
Face	92	90.8	1.2	98.69
Face	92	96.2	4.2	95.43
Face	95	96.2	1.2	98.73
Face	95	95.7	0.7	99.26
Hand	60	58.8	1.2	98.00
Hand	60	64.1	4.1	93.16
Hand	71	69.1	1.9	97.32
Hand	71	74.4	3.4	95.21
Hand	76	75.6	0.4	99.47
Hand	76	74.8	1.2	98.42
Hand	76	78.5	2.5	96.71
Hand	85	85.5	0.5	99.41
Hand	85	80.2	4.8	94.35
Leg	65	64.1	0.9	98.61
Leg	65	63.7	1.3	98.00
Leg	73	69.5	3.5	95.20
Leg	73	74.8	1.8	97.53
Leg	75	74.4	0.6	99.20
Leg	83	85.5	2.5	96.98
Leg	84	79.7	4.3	94.88
Leg	84	85.5	1.5	98.21
Chest	81	74.8	6.2	92.34
Chest	81	79.7	1.3	98.39
Chest	81	69.5	11.5	85.80
Chest	91	85.2	5.8	93.63
Chest	91	79.9	11.1	87.80
Back	87	74.8	12.2	85.98
Back	87	70.5	16.5	81.03
Back	80	85.7	5.7	92.87
Back	80	85.5	5.5	93.12
Back	80	87.7	7.7	90.30
Back	80	74.6	5.4	93.25
Back	80	85.8	5.8	92.75
Back	90	85.5	4.5	95.00
Back	90	85.7	4.3	95.22
Back	90	102.1	12.1	86.56

Table A.1: Results from Different ROIs in different recordings

B

Appendix: Results of Experiments with VM6 SureSigns ECG

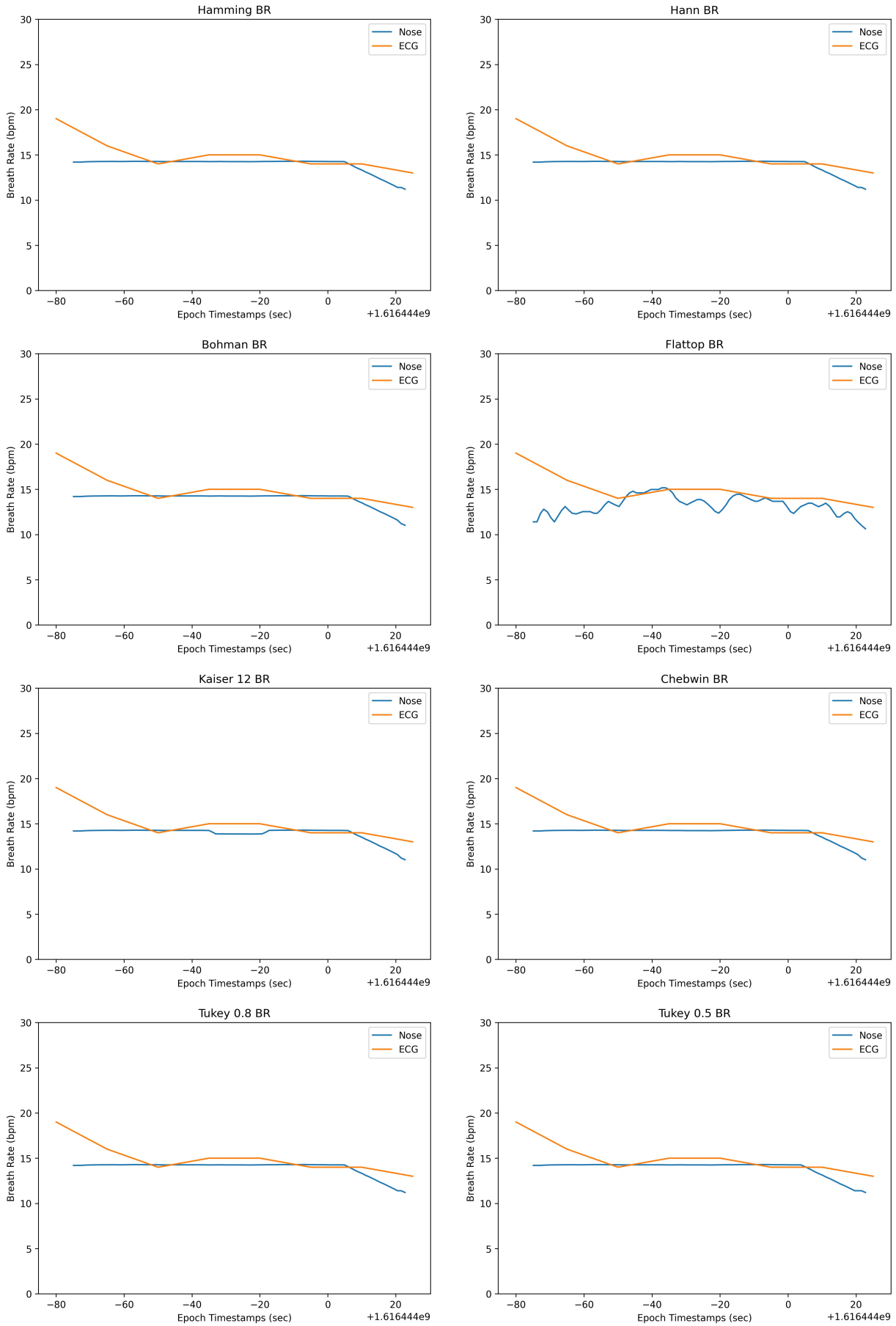

Figure B.1: Results of monitoring uniform breath rate from the nose using different windowing methods with window size of 20 sec and no zero-padding

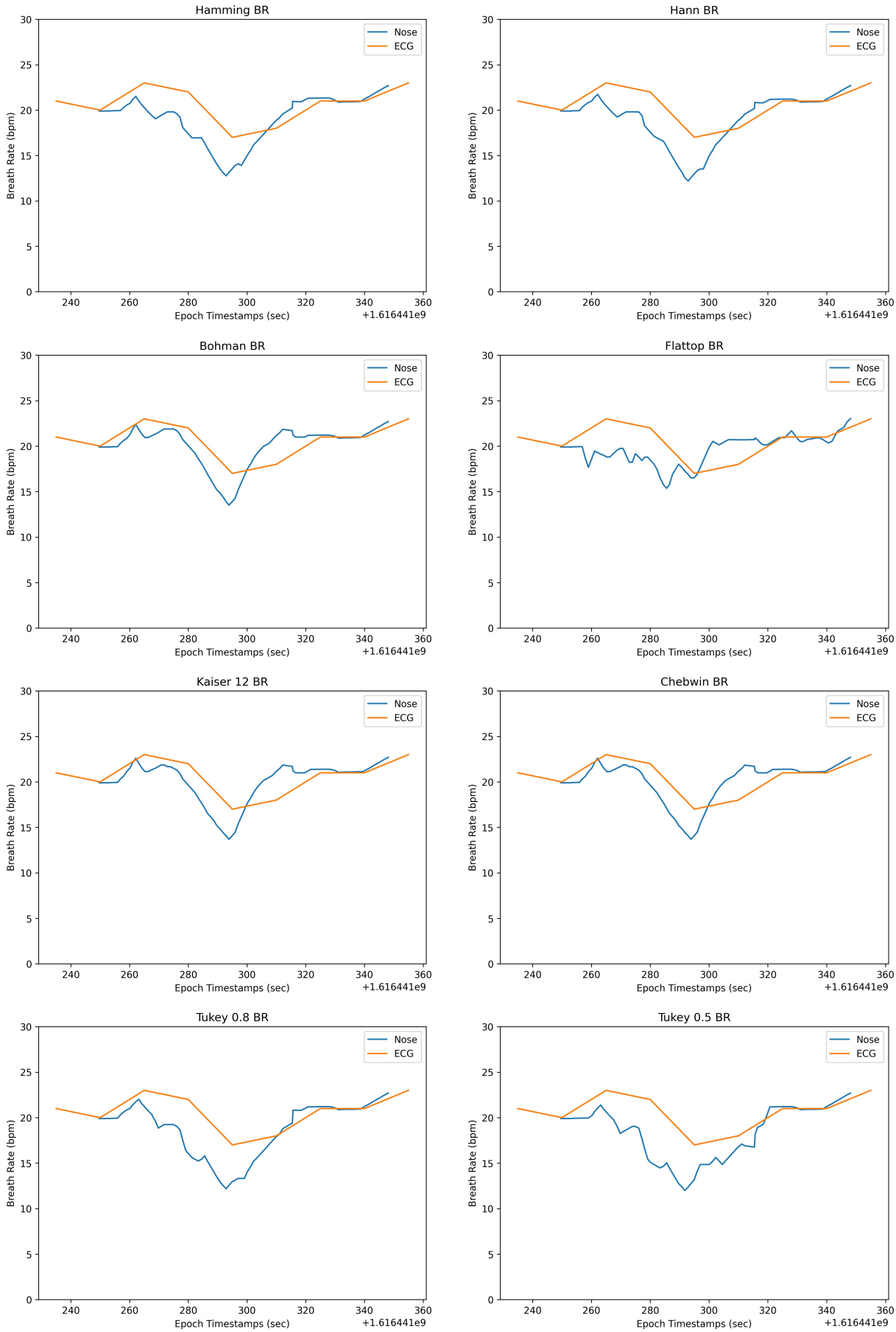

Figure B.2: Results of a recording with changing breath rate by monitoring the nose using different windowing methods with window size of 20 sec and no zero-padding

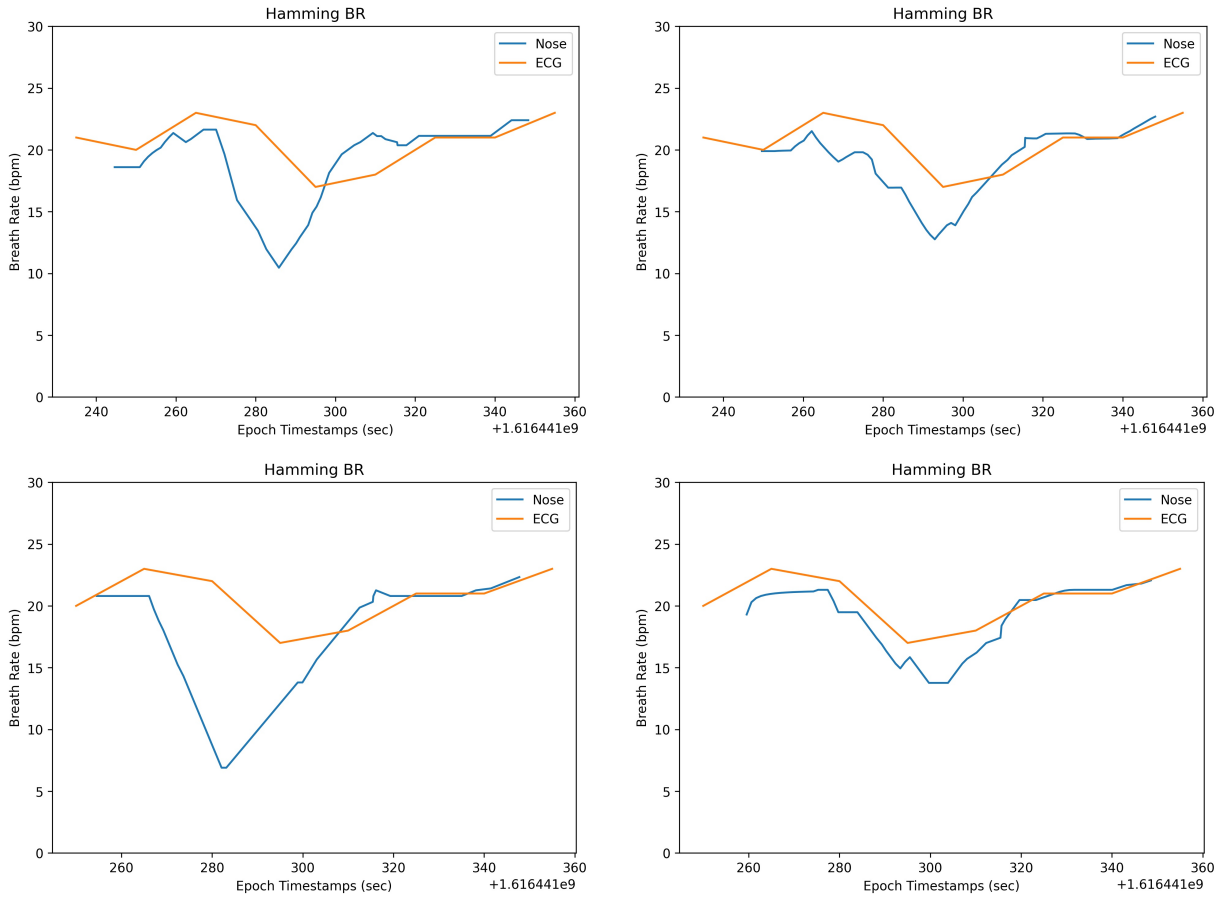

Figure B.3: Results of a recording with changing breath rate by monitoring the nose using Hamming window over window size of (1) 15 sec (2) 20 sec (3) 25 sec (4) 30 sec; and no zero-padding

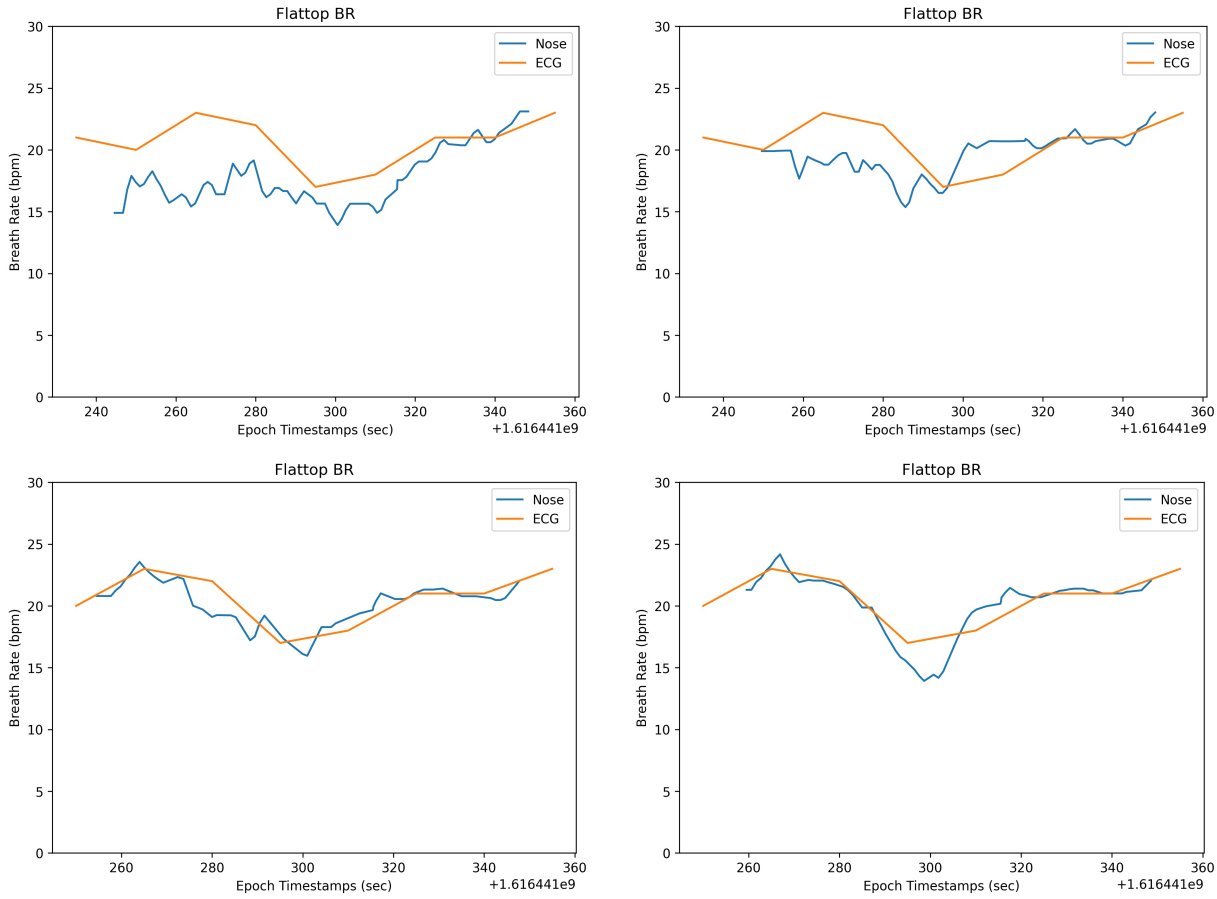

Figure B.4: Results of a recording with changing breath rate by monitoring the nose using Flattop window over window size of (1) 15 sec (2) 20 sec (3) 25 sec (4) 30 sec; and no zero-padding

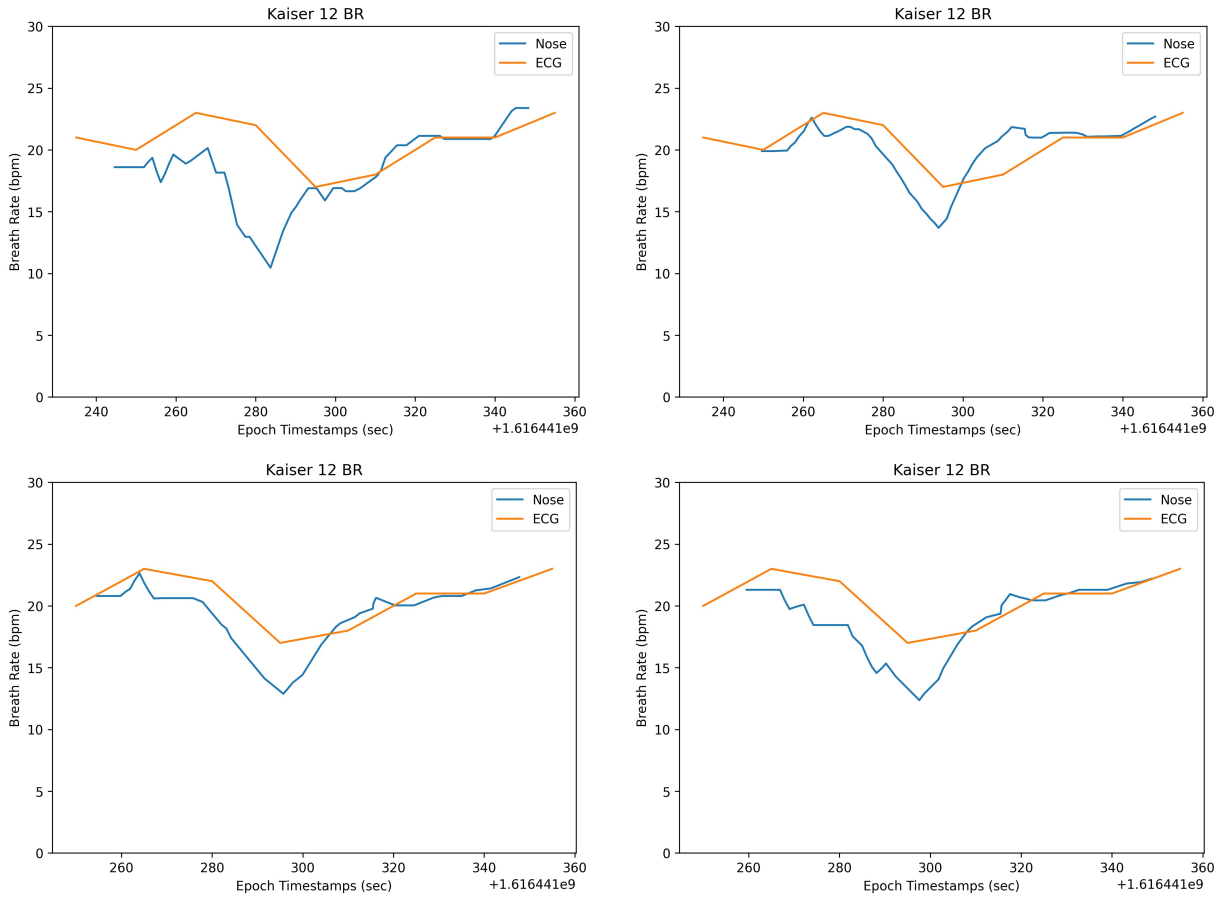

Figure B.5: Results of a recording with changing breath rate by monitoring the nose using Kaiser ($\beta = 12$) window over window size of (1) 15 sec (2) 20 sec (3) 25 sec (4) 30 sec; and no zero-padding

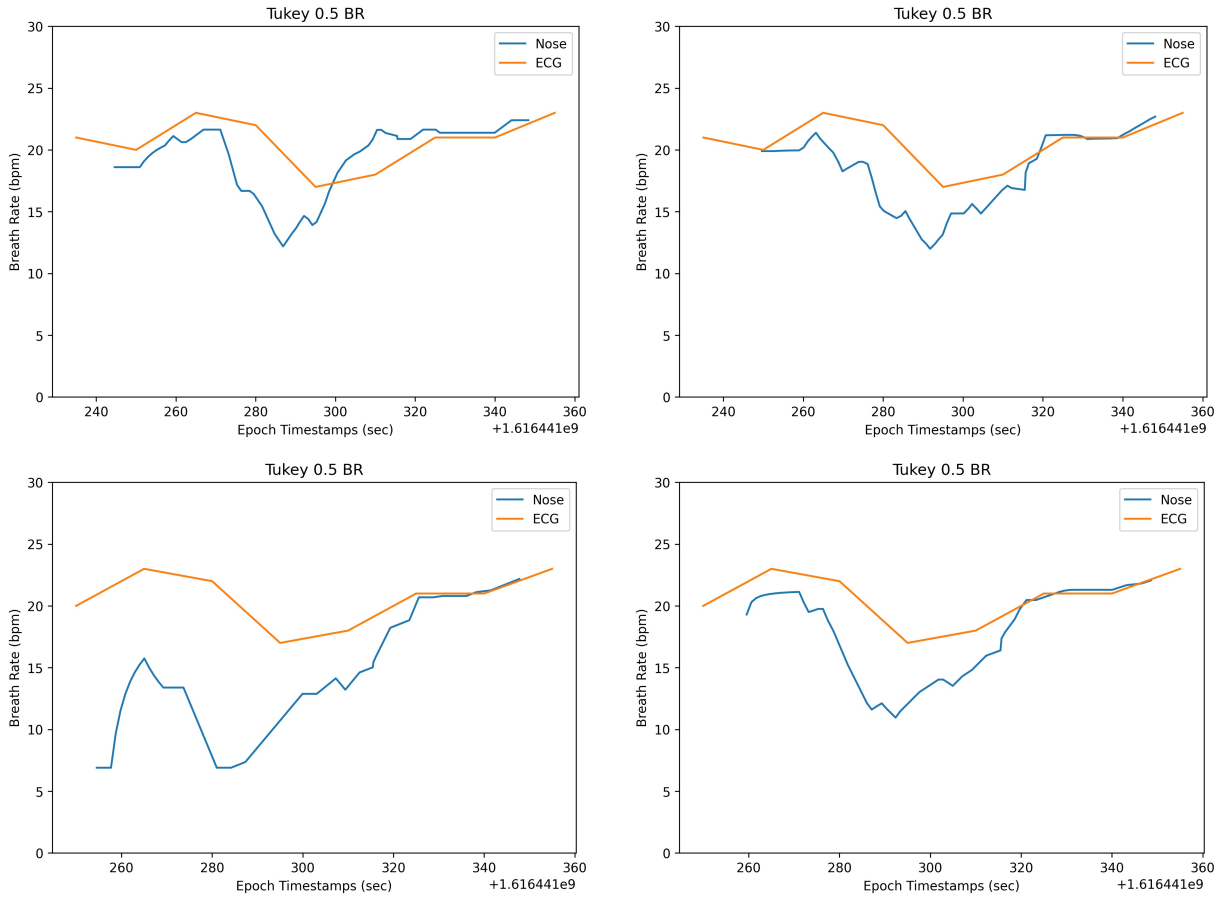

Figure B.6: Results of a recording with changing breath rate by monitoring the nose using Tukey ($\alpha = 0.5$) window over window size of (1) 15 sec (2) 20 sec (3) 25 sec (4) 30 sec; and no zero-padding

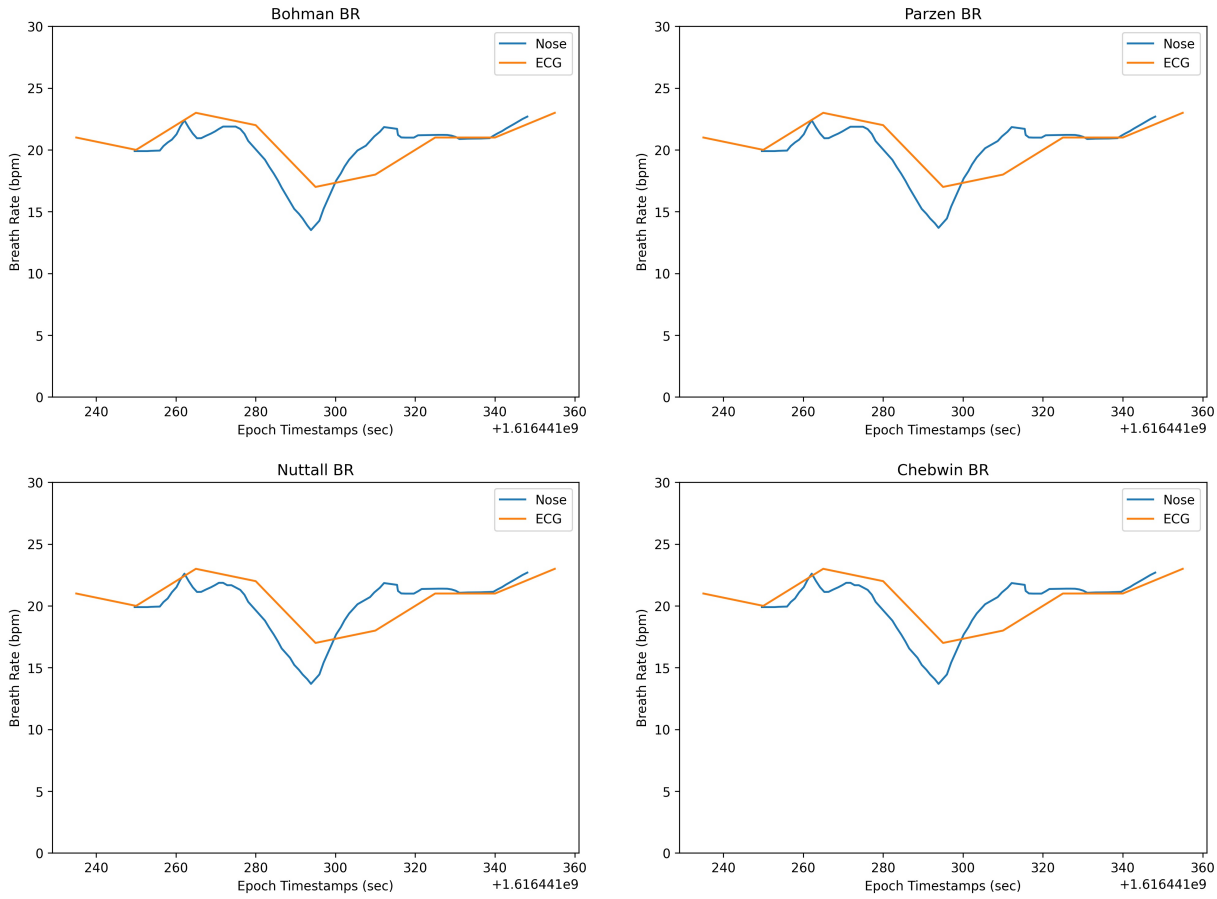

Figure B.7: Results of a recording with changing breath rate by monitoring the nose using 30 sec window and no zero-padding with windowing methods (1) Bohman (2) Parzan (3) Nuttall (4) Dolph-Chebyshev(Chebwin)

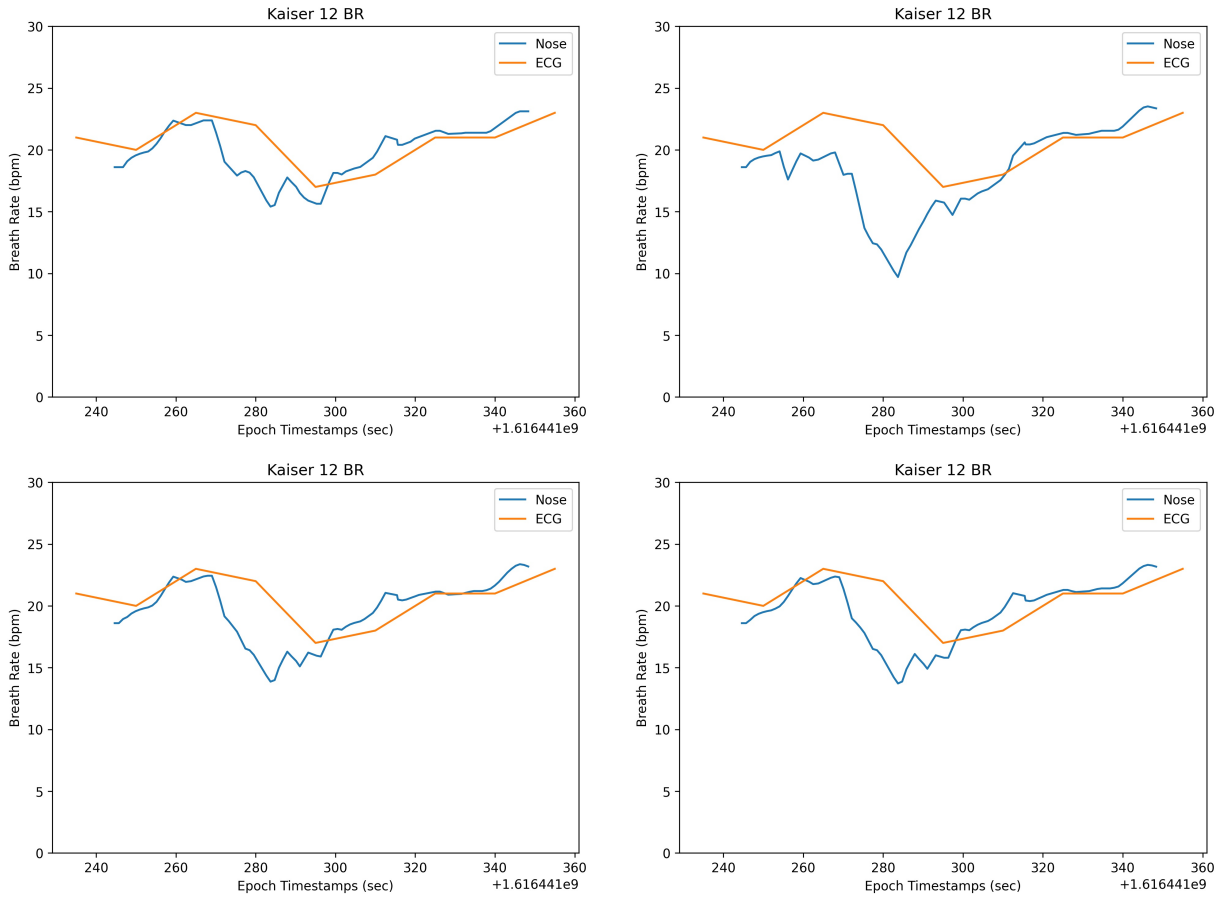

Figure B.8: Results of a recording with changing breath rate by monitoring the nose using 15 sec window and Kaiser ($\beta = 12$) with zero-padding of the signal (x length of the signal) (1) 1 time (2) 2 times (3) 3 times (4) 4 times

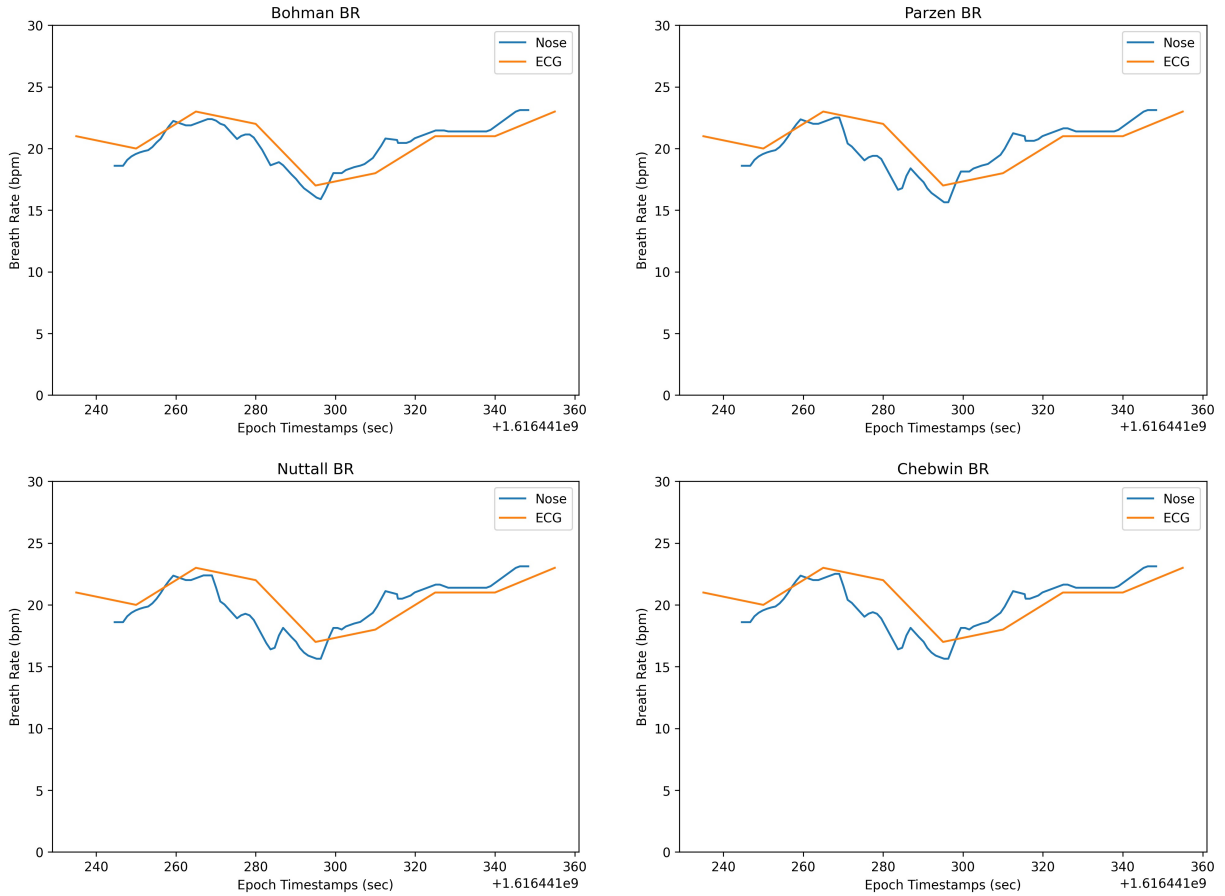

Figure B.9: Results of a recording with changing breath rate by monitoring the nose using 15 sec window and zero-padding once the length of the original signal, with windowing methods (1) Bohman (2) Parzan (3) Nuttall (4) Dolph-Chebyshev(Chebwin)

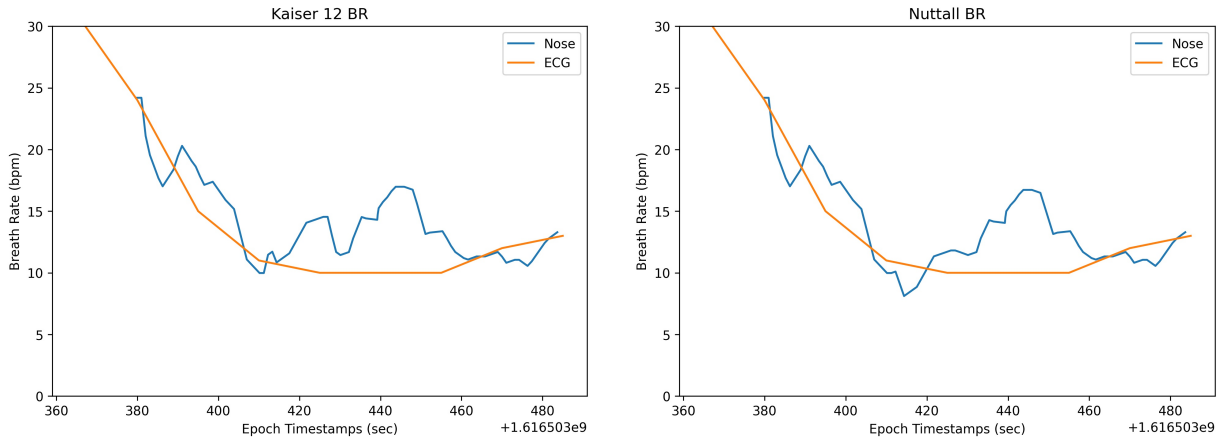

Figure B.10: Results of a recording with changing breath rate by monitoring the nose using 15 sec window and zero-padding once the length of the original signal, with windowing methods (1) Kaiser ($\beta = 12$) (2) Nuttall

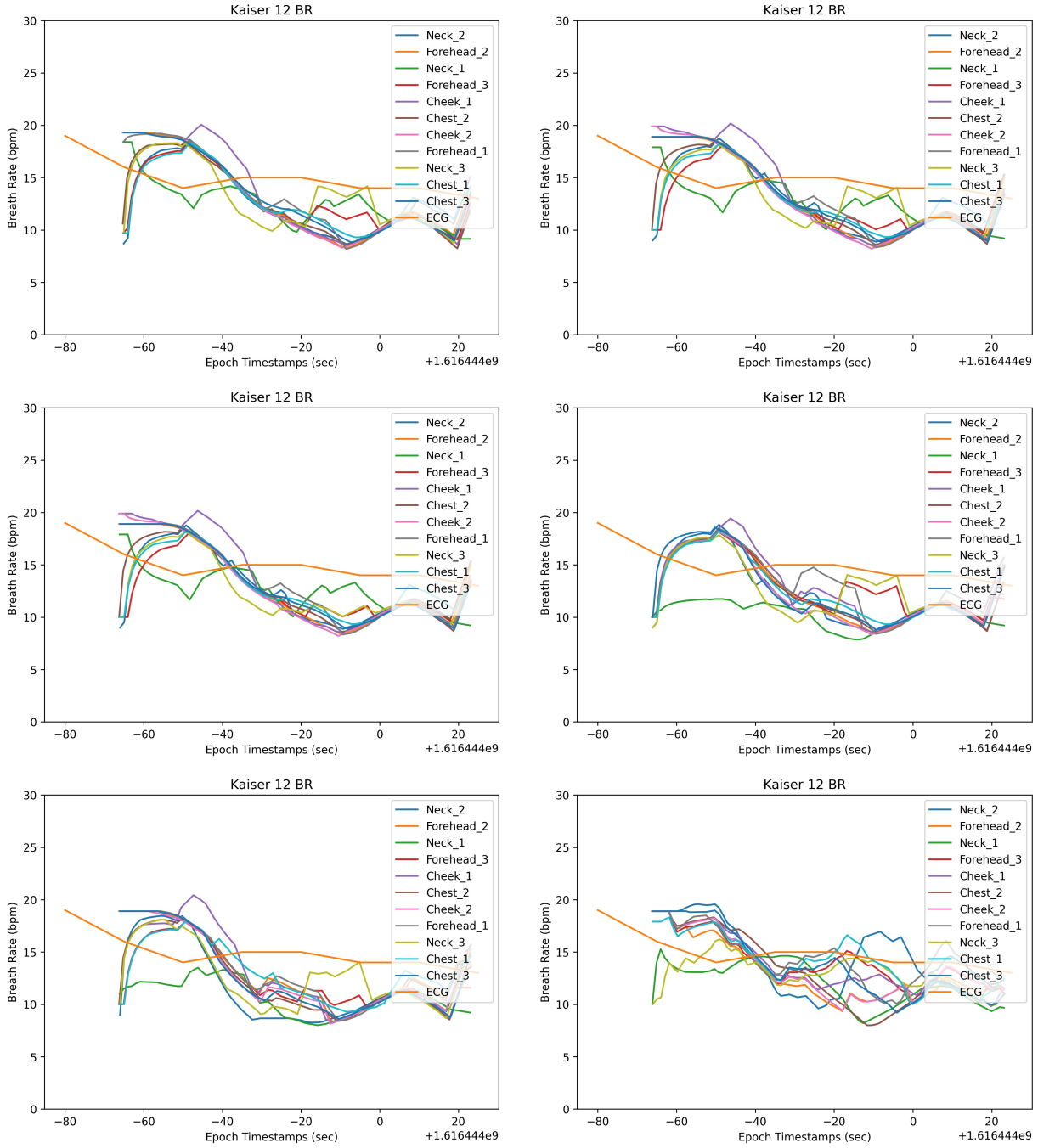

Figure B.11: Results of monitoring uniform breath rate from ROIs other than the nose using Kaiser ($\beta = 12$) window of 30 sec length and zero-padding once the length of the original signal and using a channelizer with (1) no bands, (2) 2 bands, (3) 4 bands, (4) 8 bands, (5) 16 bands, (6) 32 bands,

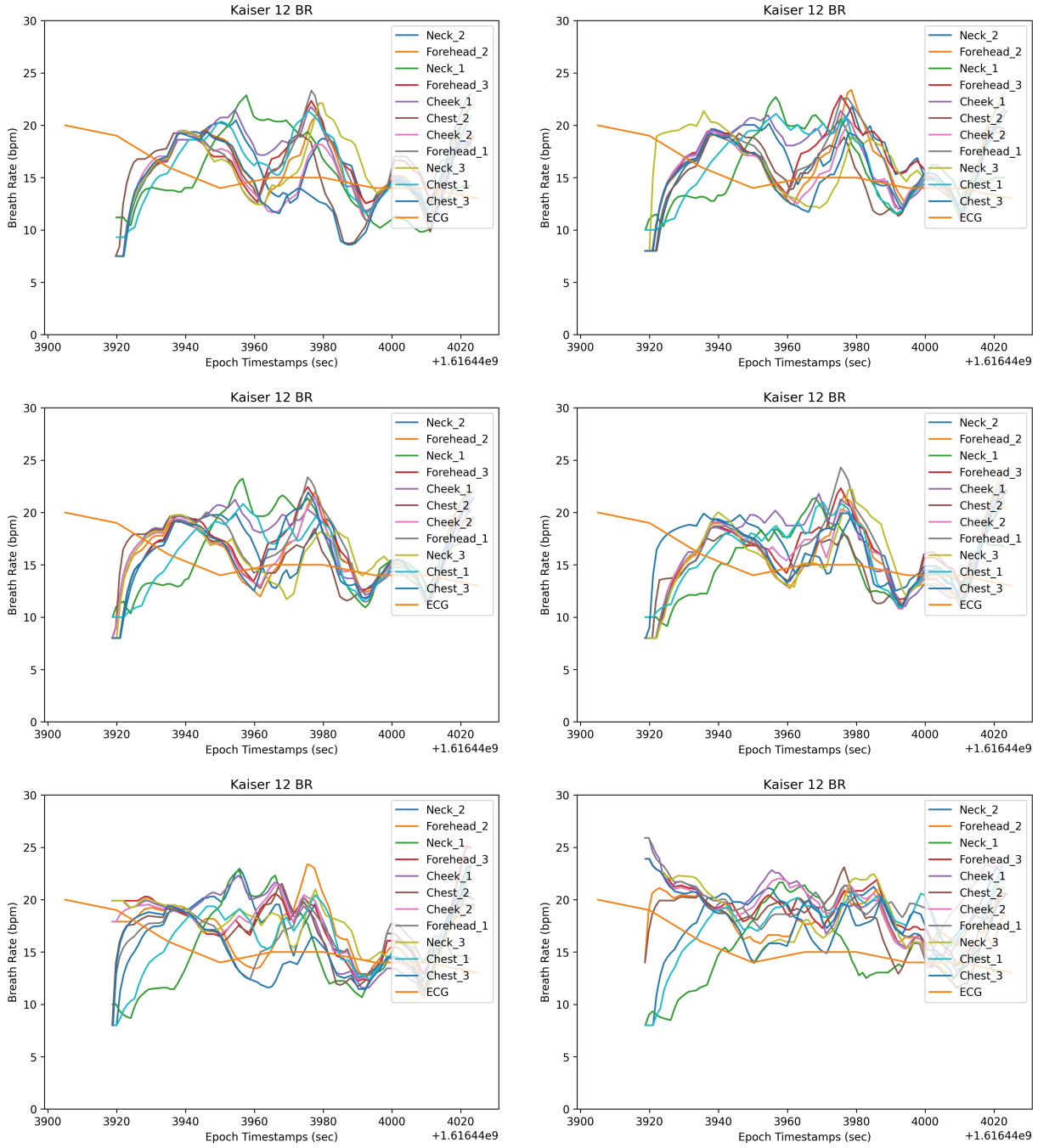

Figure B.12: Results of monitoring uniform breath rate from ROIs other than the nose using Kaiser ($\beta = 12$) window of 15 sec length and zero-padding once the length of the original signal and using a channelizer with (1) no bands, (2) 2 bands, (3) 4 bands, (4) 8 bands, (5) 16 bands, (6) 32 bands, using the same signal as fig.B.11

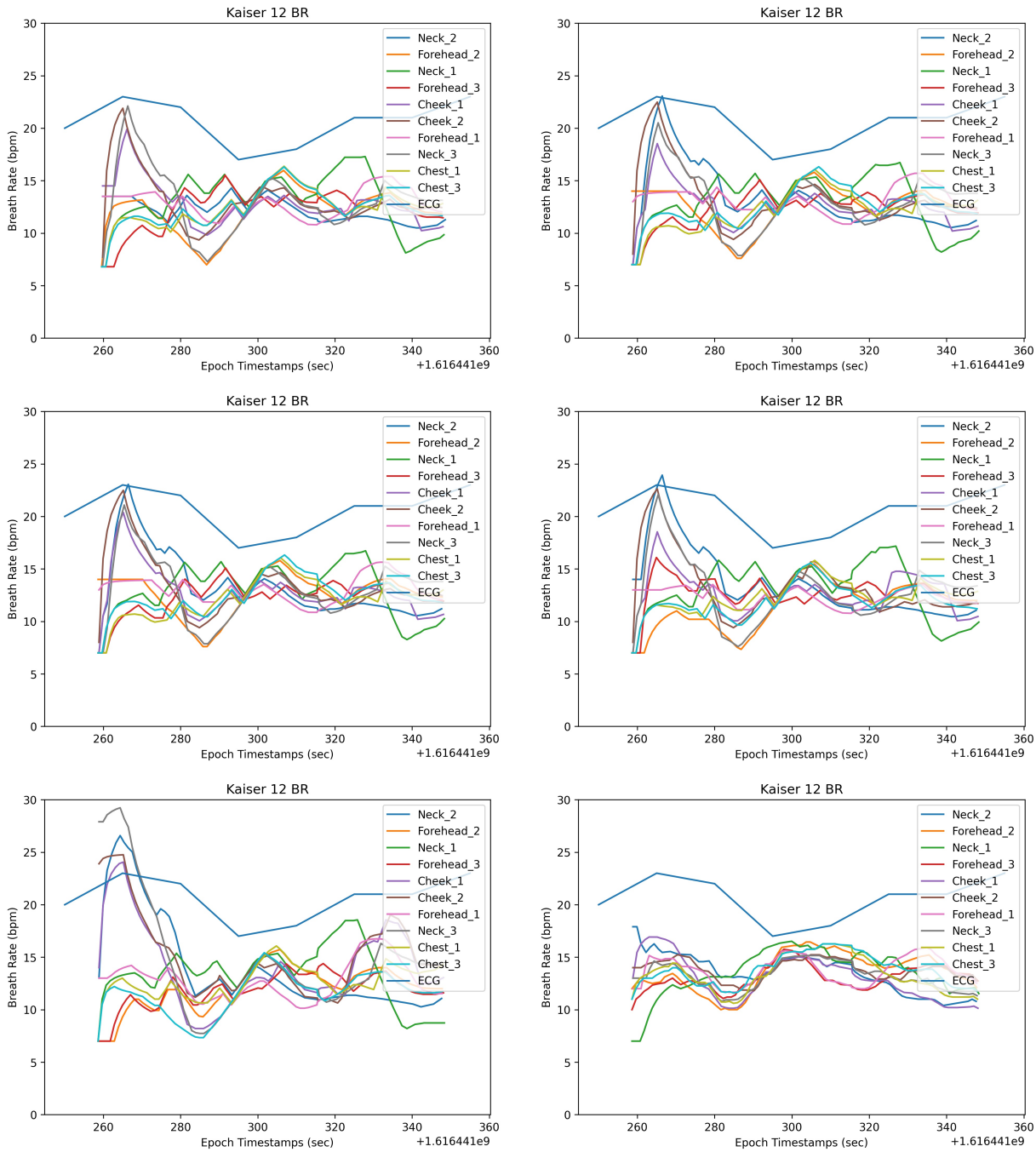

Figure B.13: Results of a recording with changing breath rate by monitoring the ROIs other than the nose using Kaiser ($\beta = 12$) window of 30 sec length and zero-padding once the length of the original signal and using a channelizer with (1) no bands, (2) 2 bands, (3) 4 bands, (4) 8 bands, (5) 16 bands, (6) 32 bands,

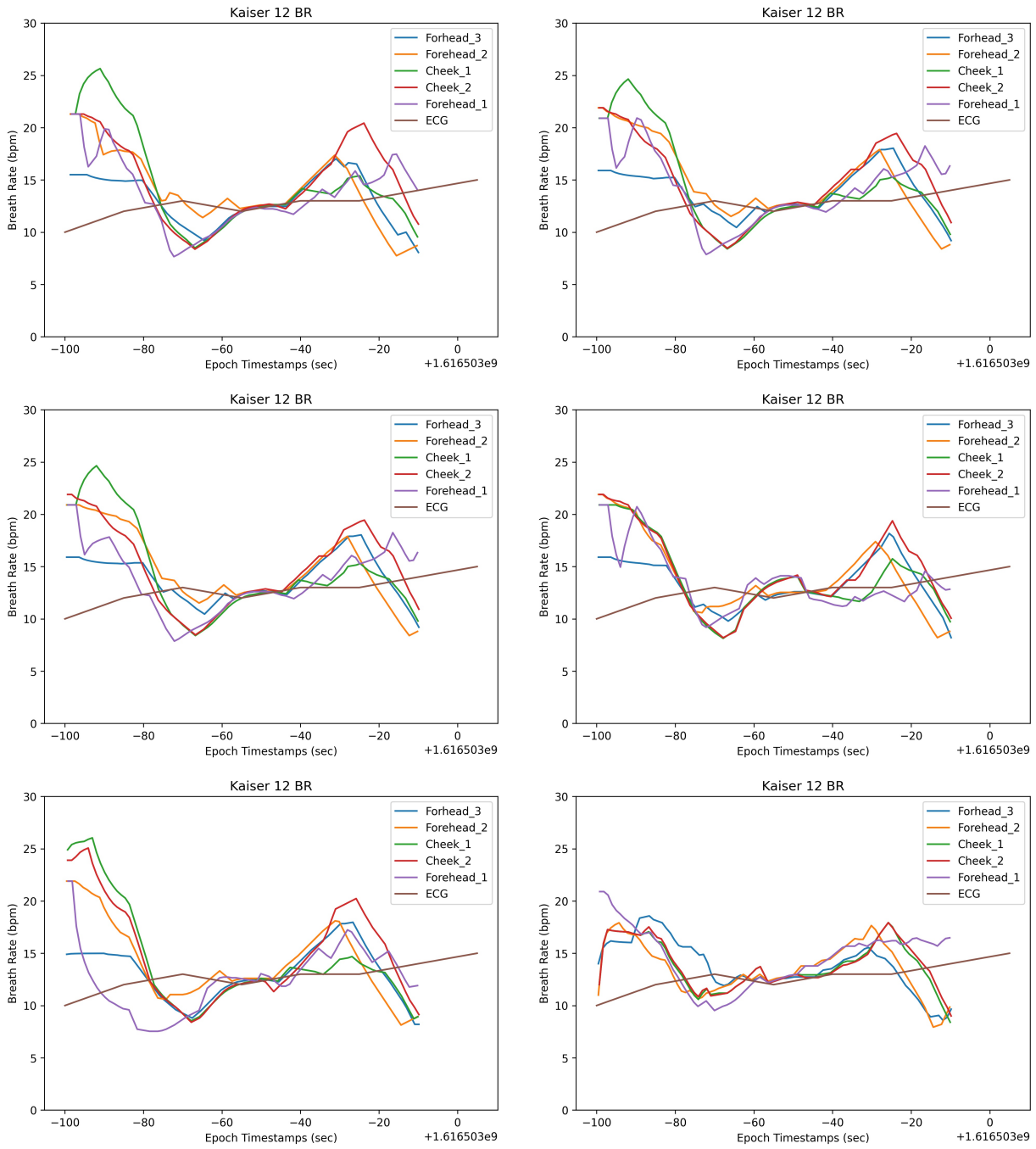

Figure B.14: Results of a recording with changing breath rate by monitoring the ROIs other than the nose using Kaiser ($\beta = 12$) window of 30 sec length and zero-padding once the length of the original signal and using a channelizer with (1) no bands, (2) 2 bands, (3) 4 bands, (4) 8 bands, (5) 16 bands, (6) 32 bands,

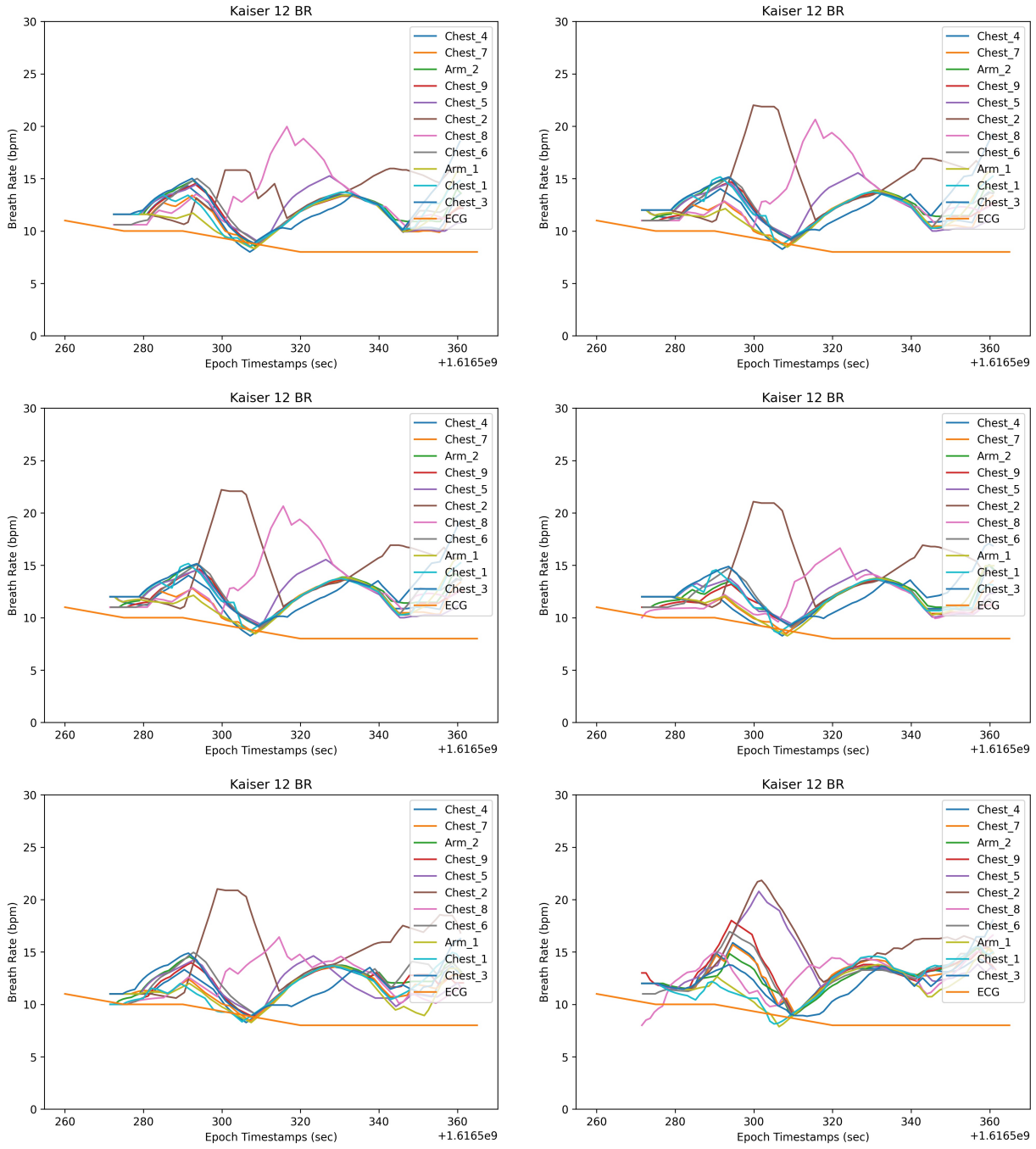

Figure B.15: Results of monitoring breath rate from the chest using Kaiser ($\beta = 12$) window of 30 sec length and zero-padding once the length of the original signal and using a channelizer with (1) no bands, (2) 2 bands, (3) 4 bands, (4) 8 bands, (5) 16 bands, (6) 32 bands,

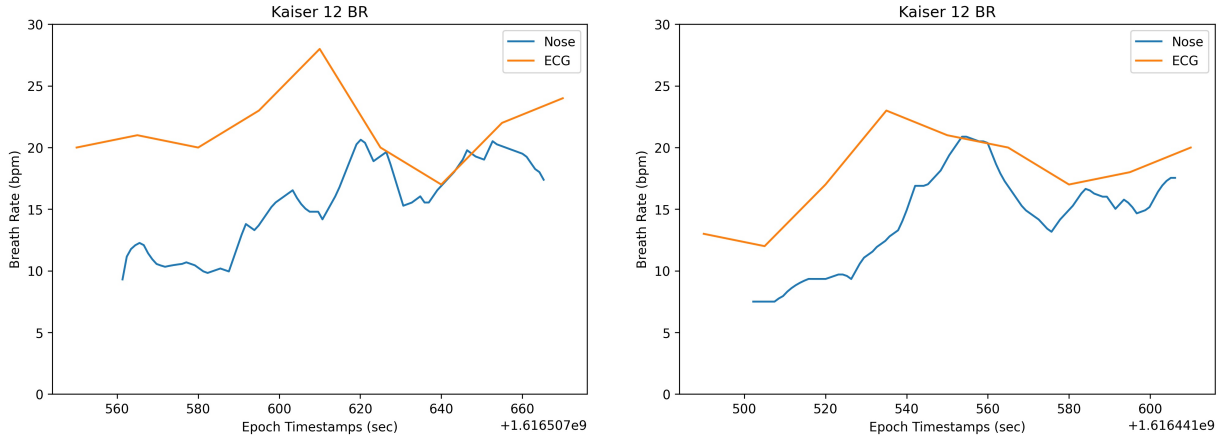

Figure B.16: Results of monitoring breath rate from the chest using Kaiser (β = 12) window of 15 sec length and zero-padding once the length of the original signal. In these situations, ECG provided incorrect readings because of (1) Talking and laughing during the recording (2) Improperly connected electrodes

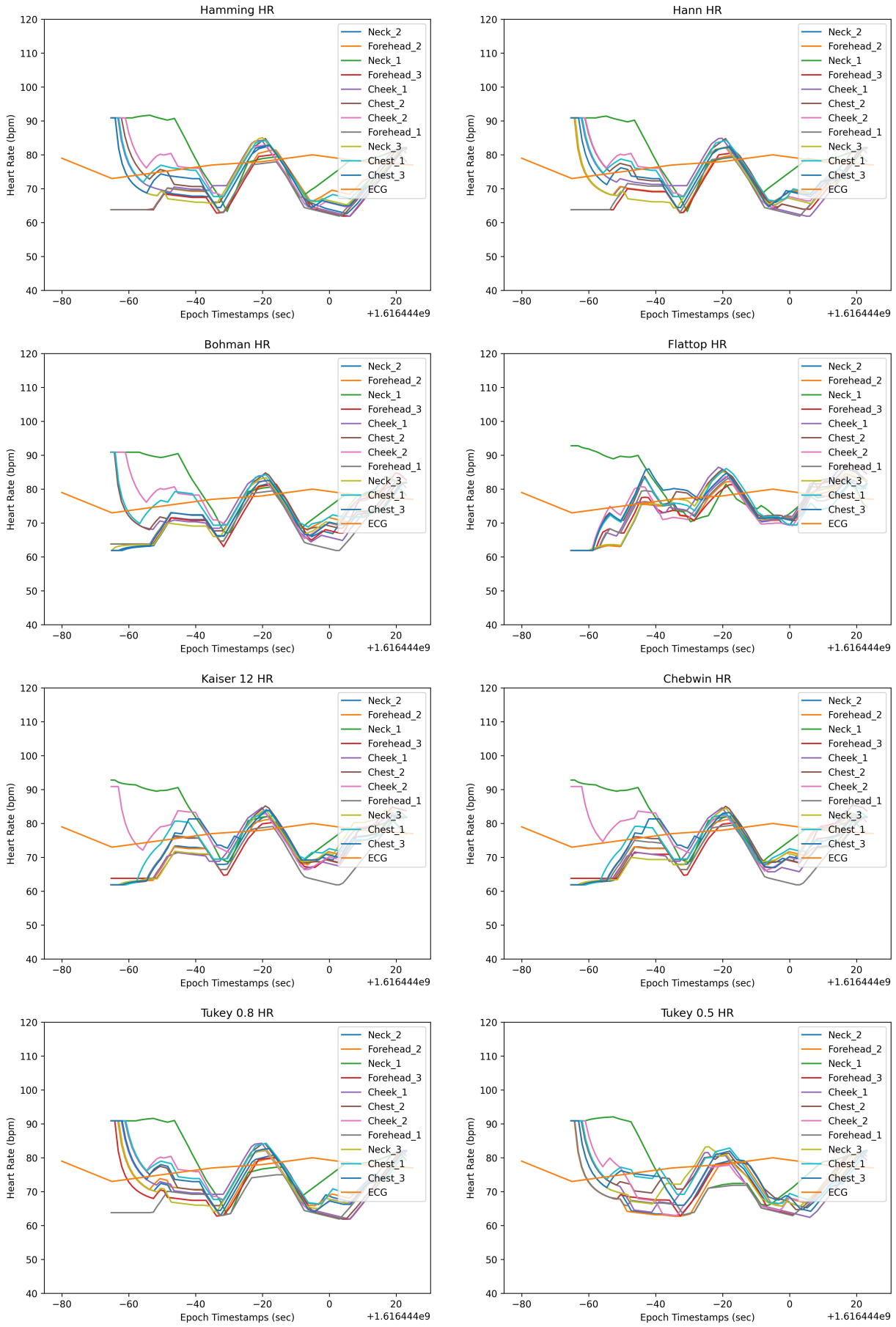

Figure B.17: Results of monitoring heart rate from different ROIs on the face, neck and chest using different windowing methods with window size of 30 sec and no zero-padding

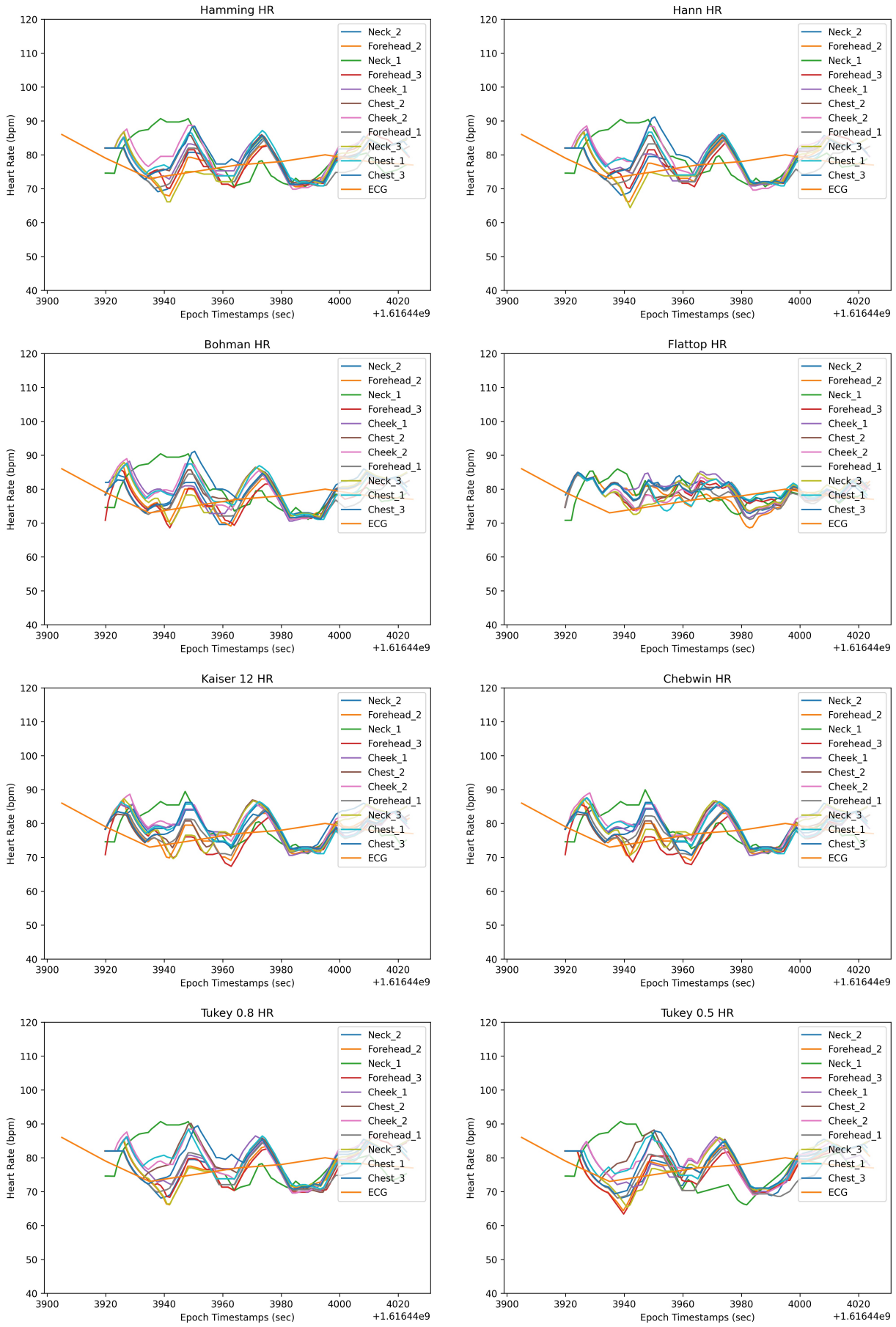

Figure B.18: Results of monitoring heart rate from the same recording as fig.B.17 using different windowing methods with window size of 15 sec and no zero-padding

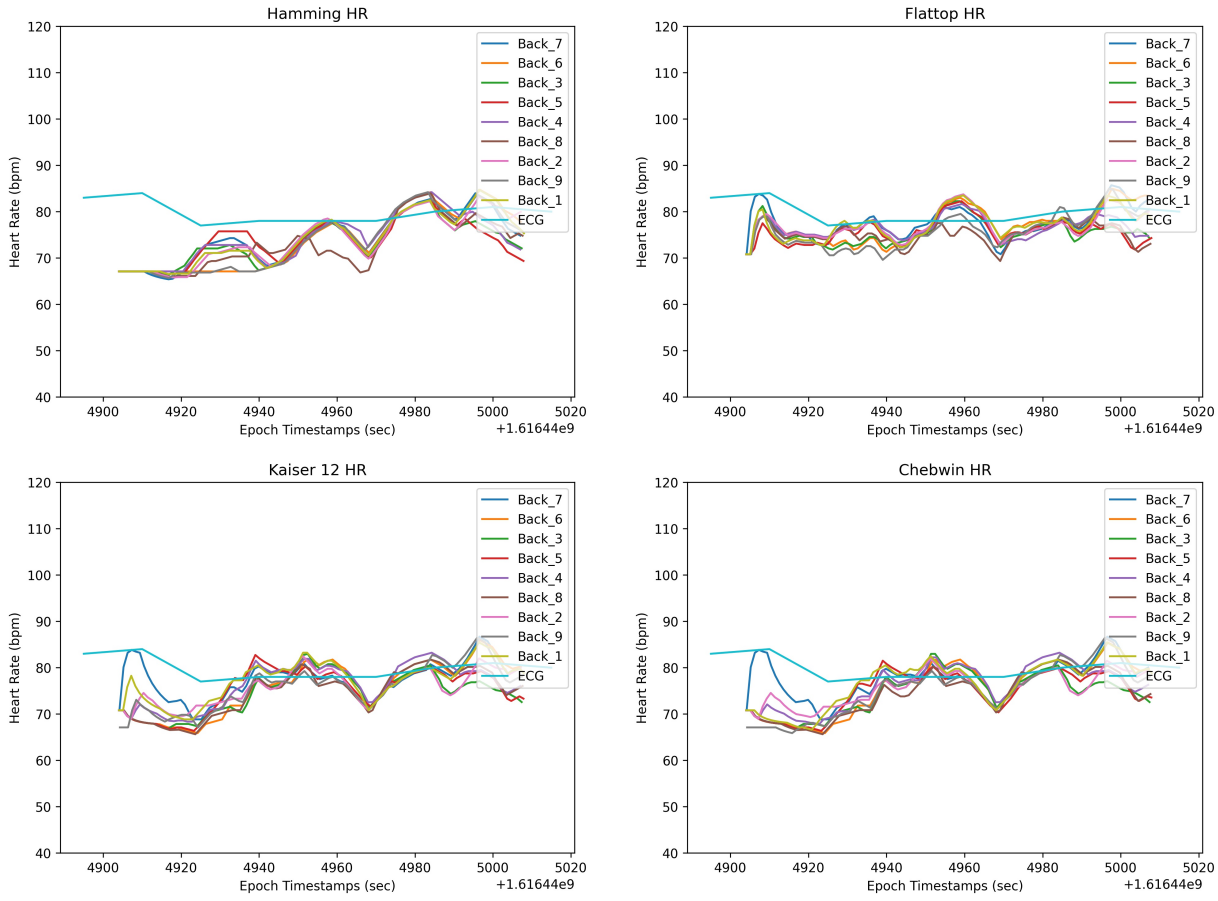

Figure B.19: Results of monitoring heart rate from different ROIs on the back using different windowing methods with window size of 15 sec and no zero-padding

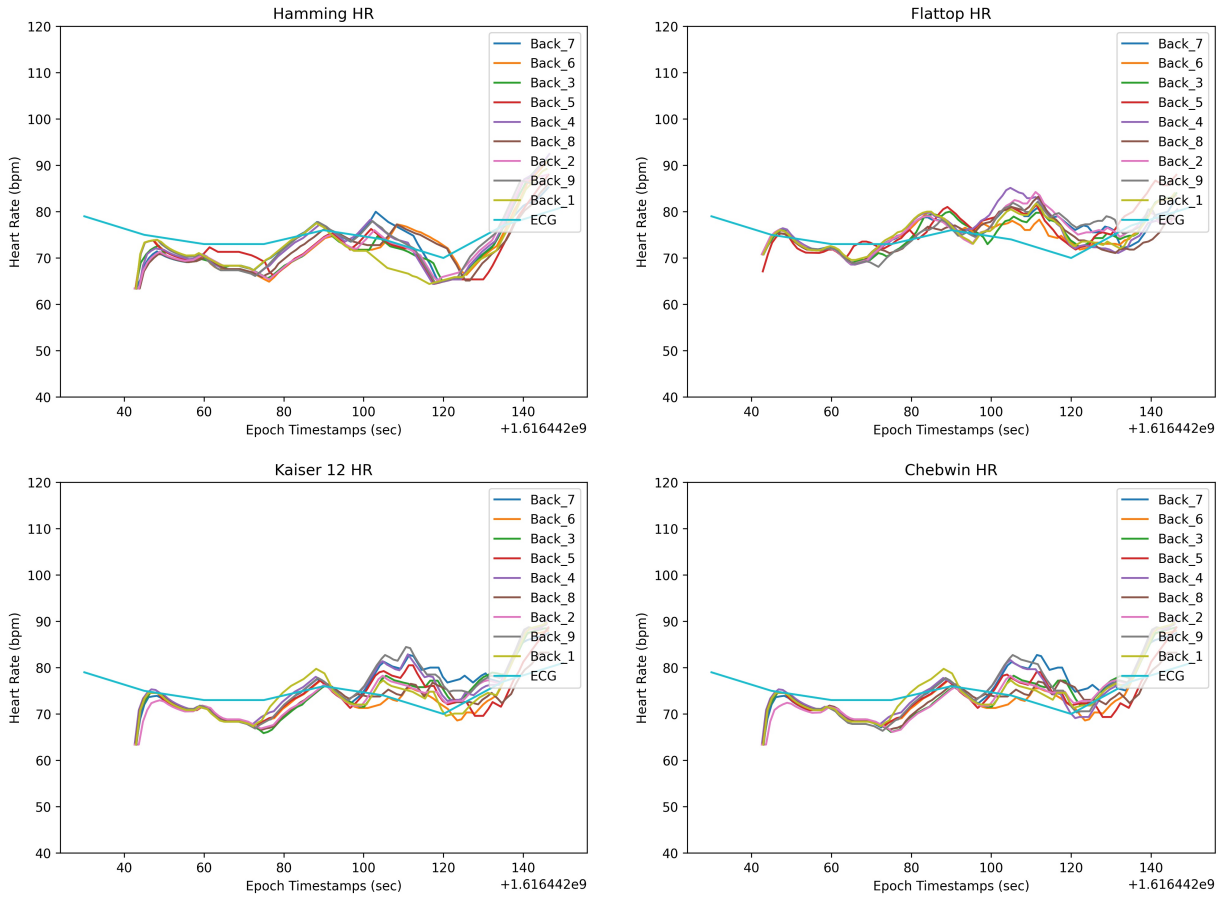

Figure B.20: Results of monitoring heart rate from different ROIs on the back of another subject using different windowing methods with window size of 15 sec and no zero-padding

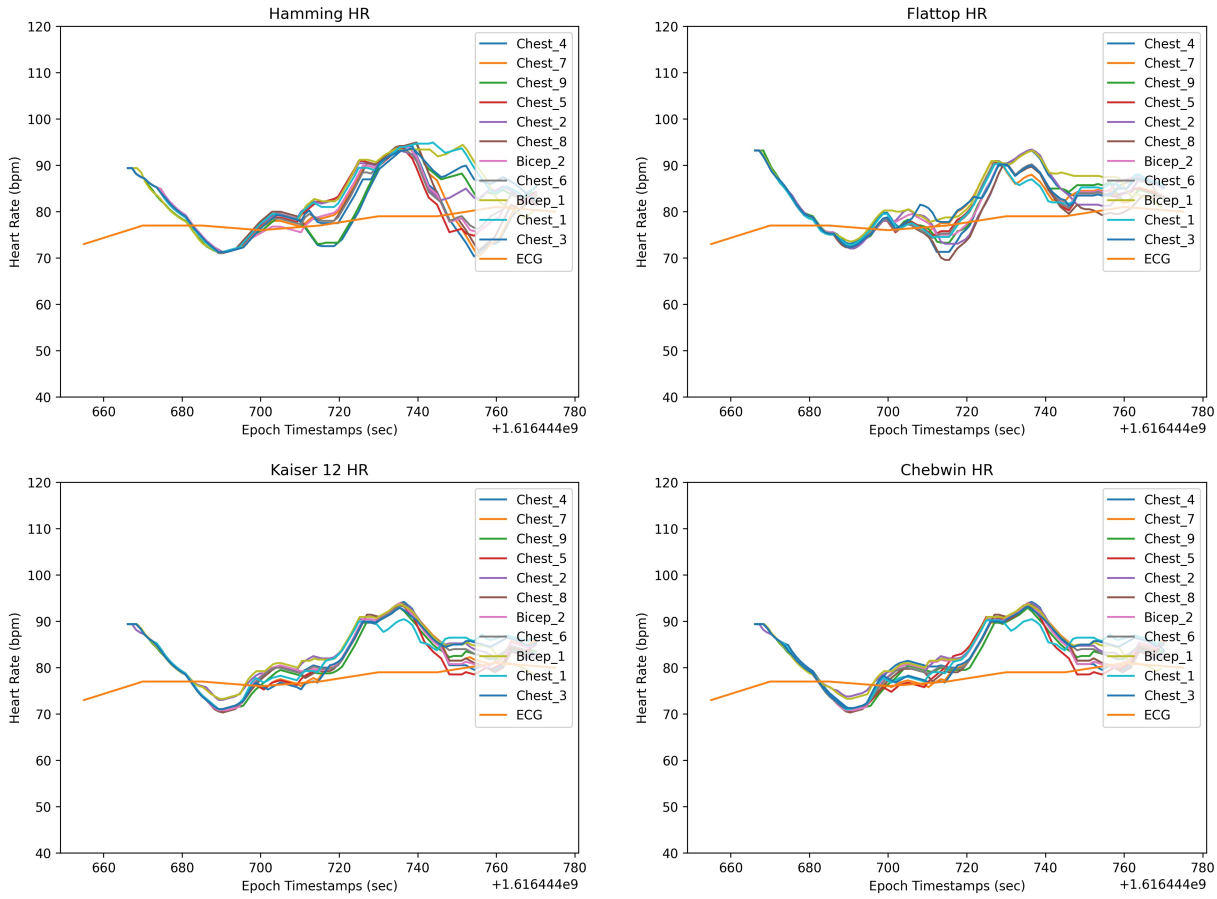

Figure B.21: Results of monitoring heart rate from different ROIs on the chest using different windowing methods with window size of 15 sec and no zero-padding

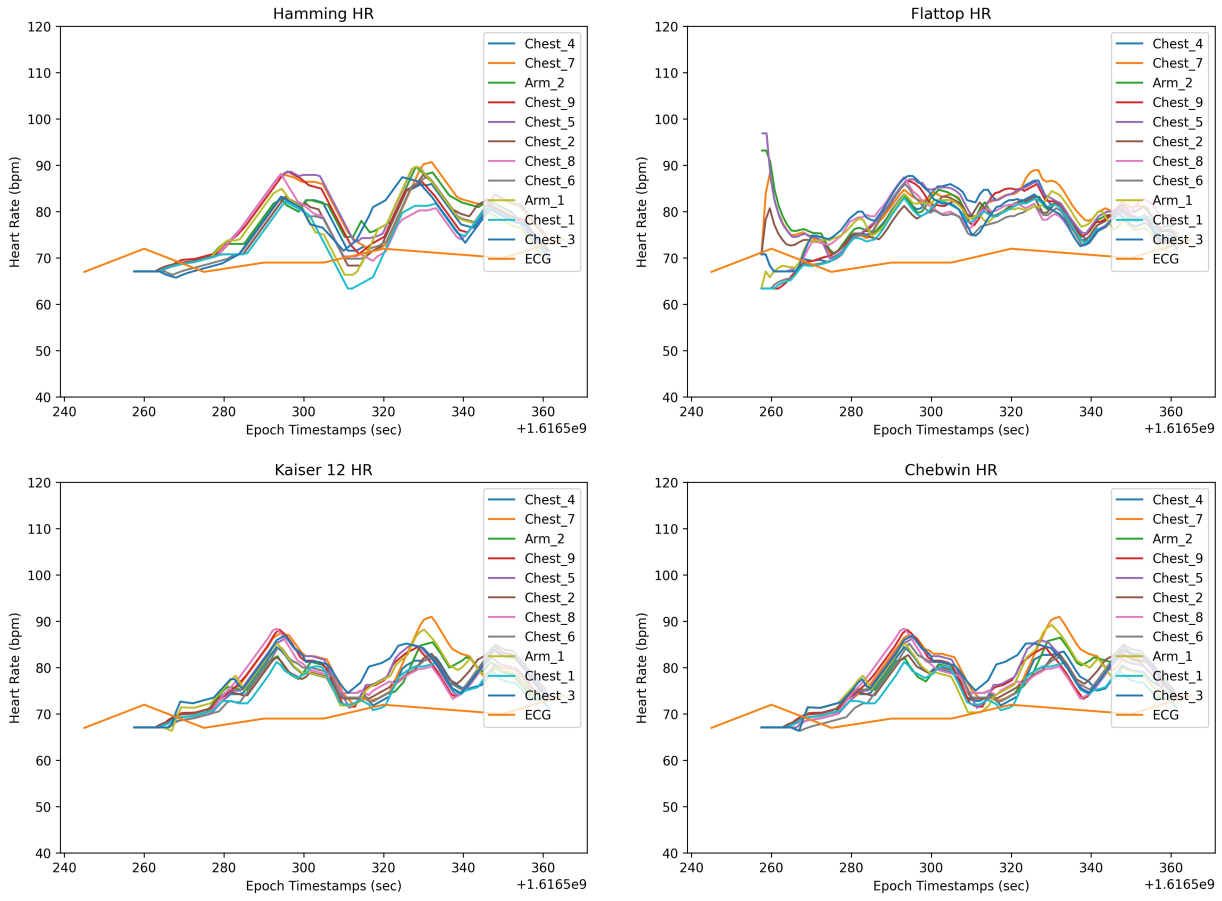

Figure B.22: Results of monitoring heart rate of a different subject from different ROIs on the chest using different windowing methods with window size of 15 sec and no zero-padding

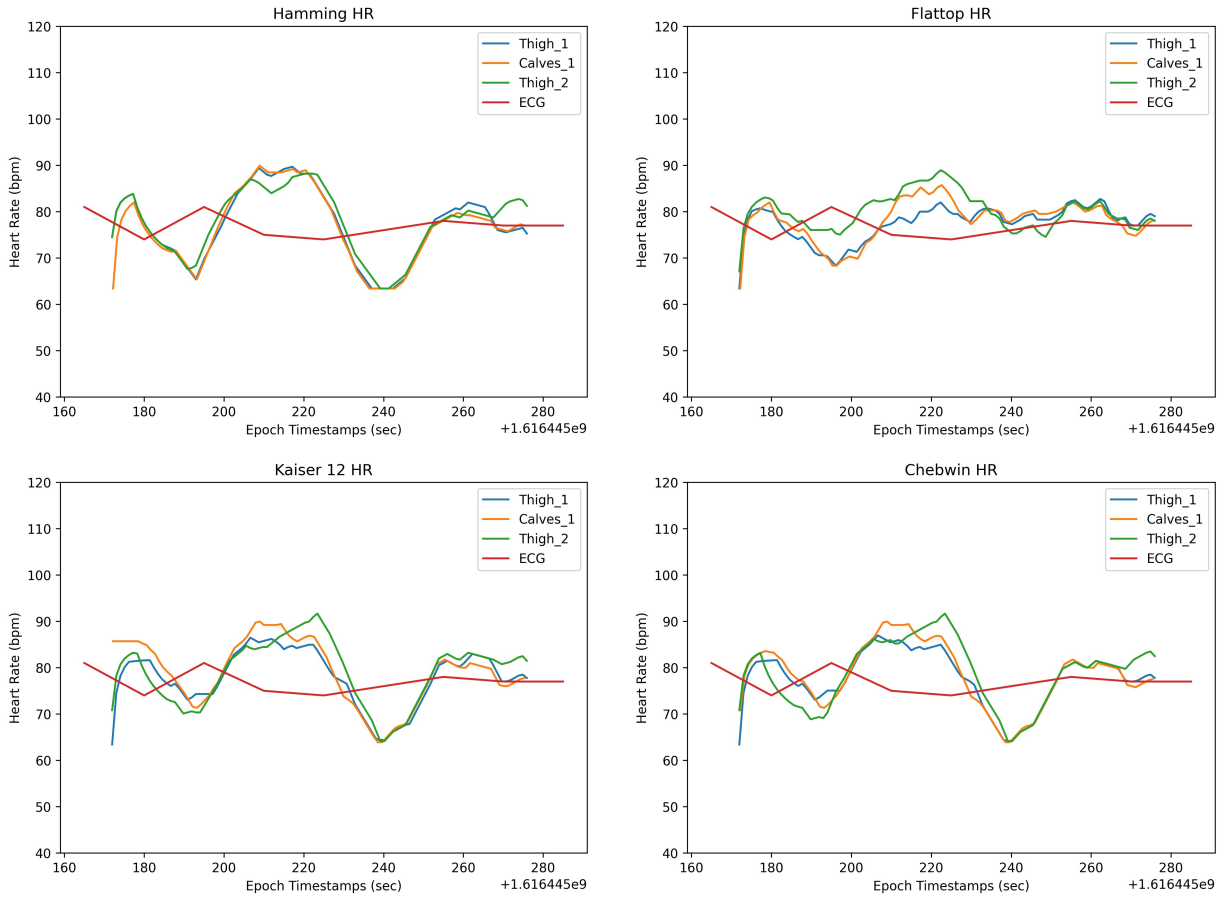

Figure B.23: Results of monitoring heart rate from different ROIs on the leg using different windowing methods with window size of 15 sec and no zero-padding

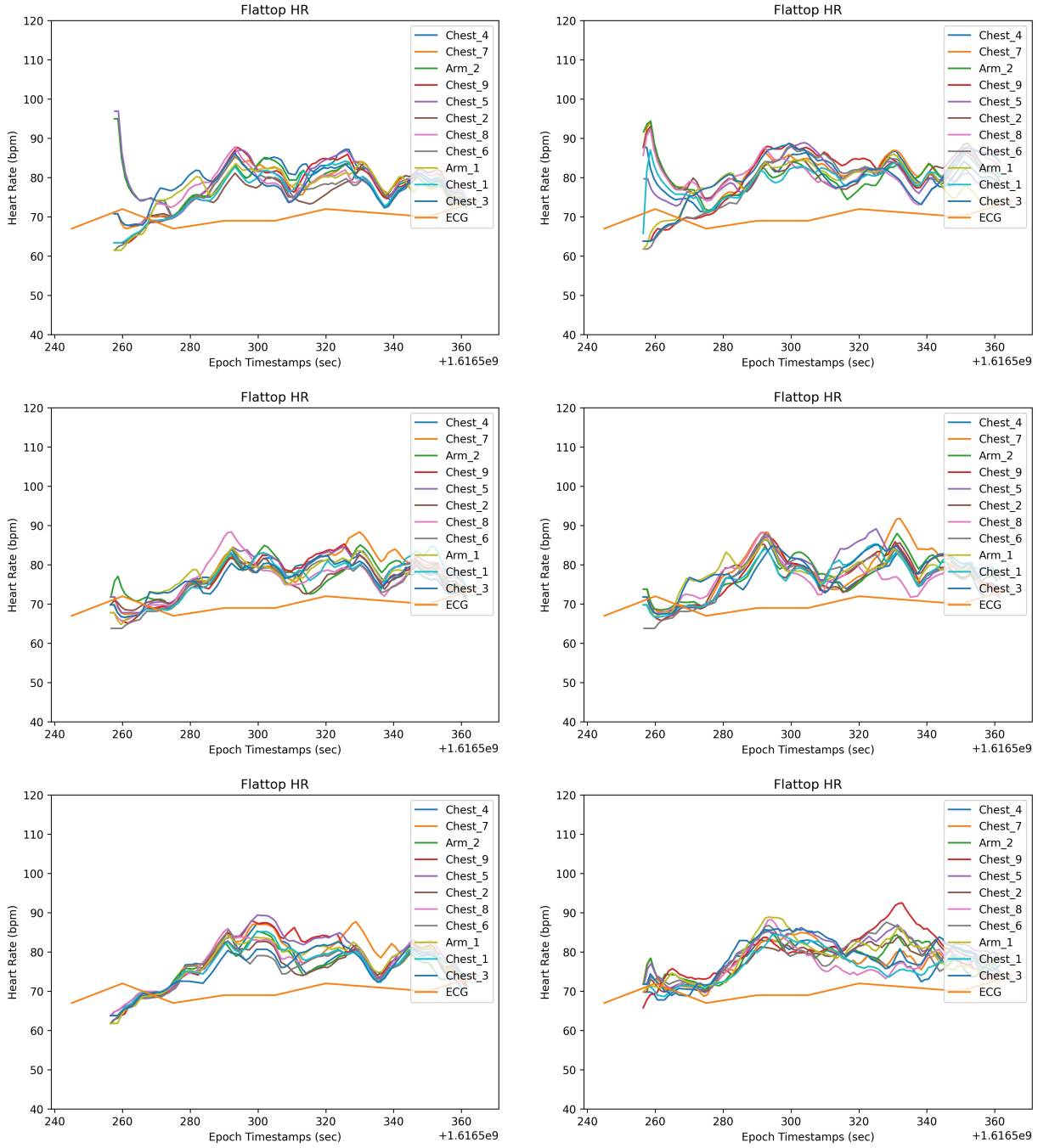

Figure B.24: Results of monitoring heart rate from different ROIs on the chest using different windowing methods with window size of 15 sec and zero-padding once the length of the signal with a channelizer of (1) 0 bands,(2) 2 bands,(3) 4 bands,(4) 8 bands,(5) 16 bands,(6) 32 bands.

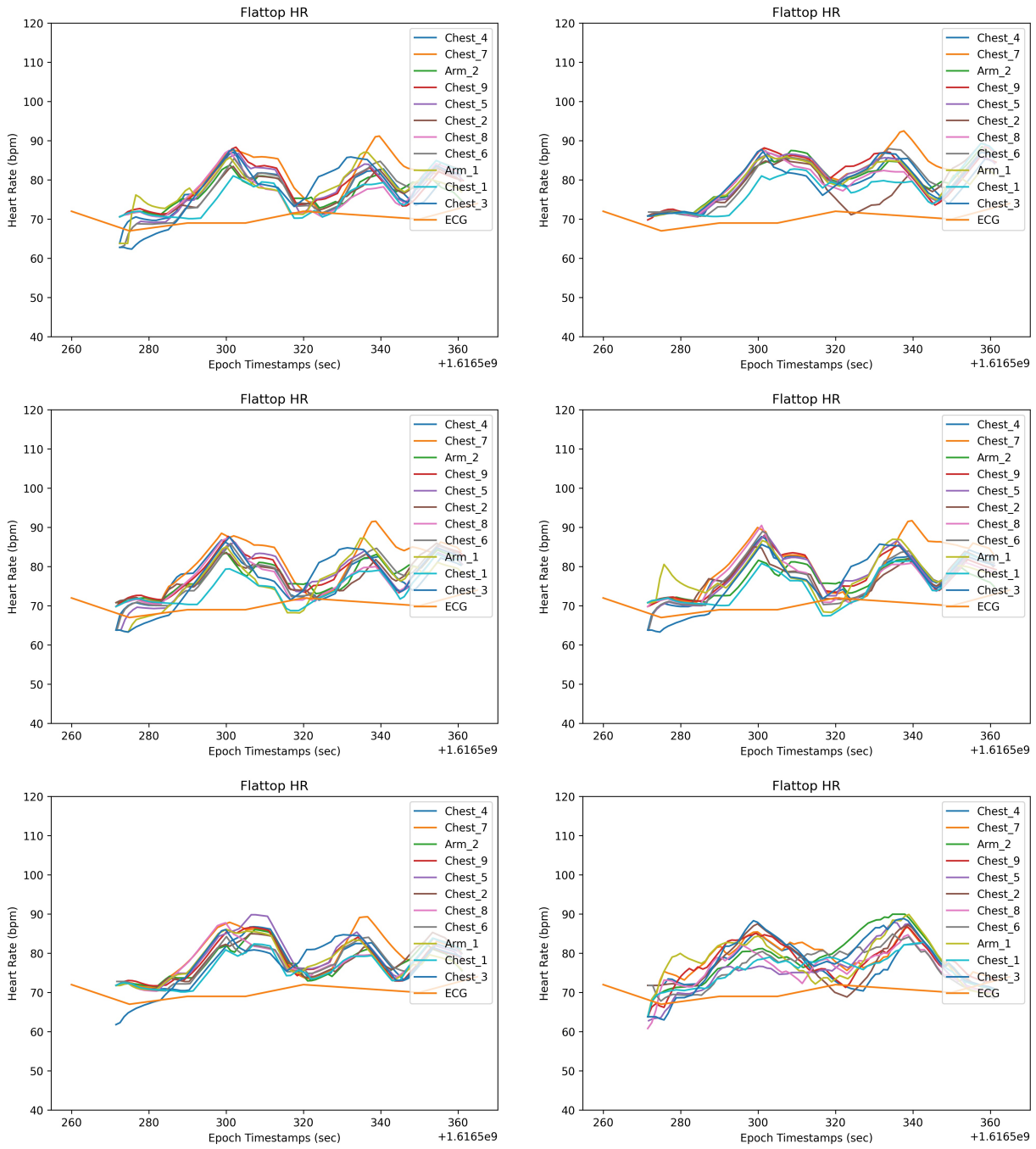

Figure B.25: Results of monitoring heart rate from different ROIs on the chest for the same recording as fig.B.24 using different windowing methods with window size of 30 sec and zero-padding once the length of the signal with a channelizer of (1) 0 bands,(2) 2 bands,(3) 4 bands,(4) 8 bands,(5) 16 bands,(6) 32 bands.

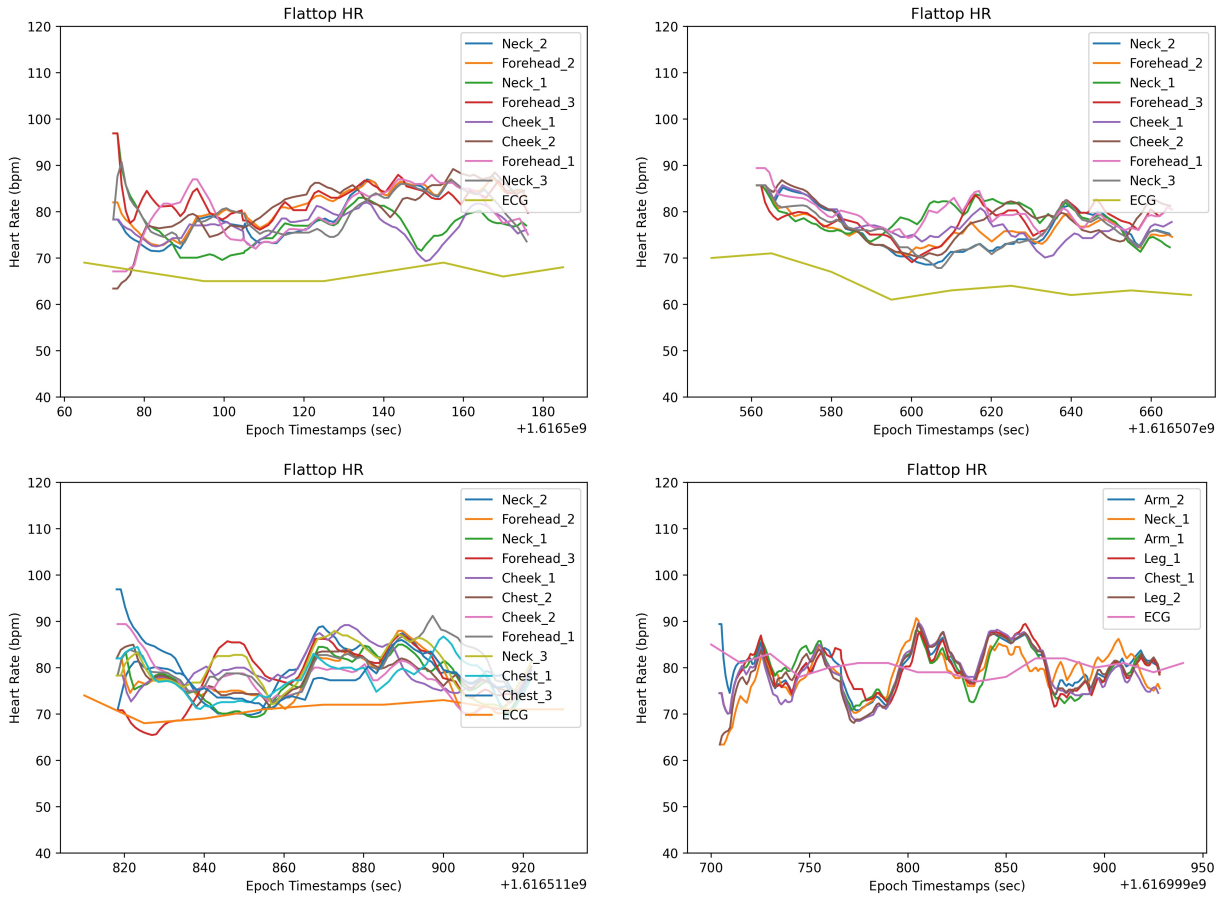

Figure B.26: Results of monitoring heart rate of different subjects from different ROIs on the face and body using the Flattop window of size of 15 sec and no zero-padding